Beam data acquisition with the IC Profiler: a feasibility study

Vincent Leduc

Master of Science

Medical Physics Unit

McGill University Montréal, Québec August 1, 2012

A thesis submitted to McGill University in partial fulfillment of the requirements for the degree of Master of Science in Medical Radiation Physics

© 2012 Vincent Leduc

ACKNOWLEDGEMENTS

First, I would like to thank my advisors, Christophe Furstoss and Piotr Pater. They helped me from start to finish and were very supportive throughout the project. Wieslaw Wierzbicki also deserves some thanks for helpful discussions and support.

I'd like to thank Patrice Munger for his ideas and for the many times he helped me out, especially on the technical side of things regarding programming and the DICOM format. I also thank Matthieu Lemire for his insights regarding beam modeling. My thanks go to Jean-René Tremblay as well for his help with materials. Thanks also to Laurent Tantôt for help in translating the thesis abstract.

I would like to acknowledge the following people with whom I had helpful discussions: Monica Serban, Jan Seuntjens, Steve Davis and Frédéric Tessier. Bill Simon, Tom Simon, Mark Rose and Jeff Hildreth from Sun Nuclear corporation were also very helpful, my thanks go to them as well.

I acknowledge and thank the following sources of funding: NSERC, Sun Nuclear corporation and CSP Medical.

ABSTRACT

This thesis reports on the feasibility of performing beam data acquisition on a medical linear accelerator (linac) using an ionization chamber array, the IC PROFILERTM (ICP; Sun Nuclear Corp., Melbourne, FL, USA). This quality assurance tool has been suggested as a possible alternative to scanning water tank (SWT) systems for the task of beam data acquisition leading to data importation into a treatment planning system (TPS) and the subsequent beam modeling. With a detector array, the potential is present to greatly reduce the important measurement time required when performing acquisition with a SWT system. A beam acquisition method allowing all data necessary for importation into Pinnacle³ (Philips Medical System, Fitchburg, WI, USA) TPS to be acquired in a short time span was developed. This method was used with a specific experimental setup to acquire all necessary beam data for the 6 MV and 18 MV beams of an Elekta Synergy® (Elekta AB, Stockholm, Sweden) linac. The resulting beam data set was compared to the data set acquired with a SWT system at the time of the original commissioning of this machine. The comparisons were performed with the use of the gamma index and by straight percentage difference, over percent depth dose (PDD) curves and beam profile (off-axis ratios, OAR) curves. The ICP-acquired data were then imported into the Pinnacle³ TPS. The resulting beam models (one for each energy and open or wedged beam), termed ICP beam models, were compared directly to clinically-used beam models for the machine (called here SWT models). Again, the comparisons were made using the gamma index and percentage difference for PDDs and OARs. Each beam model was compared to a corresponding model validation data set of measurements. The validation results from the ICP beam models were compared to the validation results of their corresponding clinical beam model. It was ensured that the ICP beam models agreed better with the ICP measurements by comparing the results of ICP model-to-ICP data and SWT model-to-ICP-data comparisons. TPS-calculated 3D dose distributions for some validation fields and clinically-used treatment plans were compared using per-voxel dose difference and the gamma index. The results of the comparisons of ICP data to SWT data show that, on average over all field sizes, for a 2 %, 2 mm tolerance for the gamma index, the 6 MV acquisition data set has a passing rate of 97.7 % for OARs and 96.3 % for PDDs, while passing rates are respectively 99.0 % and 95.7 % for the 18 MV data set. The ICP-measured relative dose factors (RDF) show an underestimation for the smallest field sizes and an overestimation for the largest field sizes, the effect being more prominent for the 6 MV beam than the 18 MV beam. 3D dose distribution comparisons show that there are significant differences present between the two beam models mainly in the buildup region of the PDDs and the beam penumbrae. These differences in the beam models sometimes lead to differences that could affect clinical decisions as to whether or not a treatment plan is suitable for use. Overall, with the developed method, it may be said that the IC PROFILERTM is not suitable for performing beam acquisition for the purpose of TPS data importation. However, the method presented in this work allows a great speed in making measurements to be achieved (\approx 3 measurements per minute). In combination with the ICP, this method could be a way of performing beam matching, where one seeks to confirm if a machine's beam matches that of another, or simply as a fast way to obtain quality assurance baseline measurements. Other than the development of a rapid beam data acquisition method, this work allowed the determination of some limitations of the ICP in the context of beam commissioning.

RÉSUMÉ

Cette thèse traite de la faisabilité d'effectuer l'acquisition des données de faisceau d'un accélérateur linéaire médical (linac) à l'aide d'une matrice de chambres d'ionisation, l'IC Profiler IM (ICP; Sun Nuclear Corp., Melbourne, FL, É.-U.). Cet outil de contrôle de la qualité a été proposé comme alternative possible aux systèmes à balayage dans l'eau (SWT) pour l'acquisition des données qui seront importées dans le système de planification de traitement (TPS) pour créer les modèles de faisceau. Le temps d'acquisition des données avec une matrice de détecteurs est potentiellement très réduit en comparaison du temps nécessaire avec un SWT. Une méthode a été développée pour acquérir en un minimum de temps toutes les données de faisceau requises pour l'importation dans Pinnacle³ (Philips Medical System, Fitchburg, WI, É.-U.). Cette méthode a été utilisée avec un protocole expérimental spécifique afin d'acquérir les données nécessaires des faisceaux de 6 MV et 18 MV d'un linac Synergy® d'Elekta (Elekta AB, Stockholm, Suède). Les données de faisceau obtenues ont été comparées aux données acquises avec un SWT au moment de la mise en service initiale de l'accélérateur. Les comparaisons ont été effectuées à l'aide de l'index gamma et par différence relative des courbes de rendement en profondeur (PDD) et des courbes de rapports hors axe (OAR). Les données acquises avec l'ICP ont ensuite été importées dans le TPS Pinnacle³. Les modèles de faisceau obtenus, dits modèles ICP, ont ensuite été comparés directement aux modèles SWT utilisés en clinique. Encore une fois, les comparaisons ont été effectuées avec l'index gamma et la différence relative des courbes de PDD et d'OAR. Chaque modèle ICP a aussi été validé à l'aide de données de validation mesurées indépendamment. Les résultats de validation de chaque modèle ICP ont étés comparés aux résultats de validation du modèle clinique correspondant. Les données ICP ont été comparées aux modèles SWT et aux modèles ICP et il a été vérifié que les modèles ICP s'accordent mieux avec les données ICP. Des distributions de dose en 3D, calculées avec le TPS pour quelques champs de validation et pour des plans de traitement cliniques, ont été comparées par soustraction voxel par voxel et avec l'index gamma. Les résultats des comparaisons des données ICP et des données SWT montrent qu'en moyenne, sur tous les champs, avec une tolérance de 2 %, 2 mm sur l'index gamma, les données d'acquisition du faisceau de 6 MV ont un taux de passage de 97,7 % pour les OAR et de 96,3 % pour les PDD, tandis que les taux de passage sont respectivement de 99,0 % et 95,7 % pour les données du 18 MV. Les facteurs de dose relative (RDF) mesurés avec l'ICP sont sous-estimés pour les petits champs et surestimés pour les grands champs, le phénomène étant plus prononcé pour le 6 MV que pour le 18 MV. Les comparaisons des distributions de dose en 3D montrent qu'il y a des différences significatives entre les deux modèles ICP et SWT, notamment dans la zone de recouvrement électronique (build-up) des PDD et dans la pénombre des champs. Ces différences entre modèles mènent quelques fois à des différences entre plans de traitement qui pourraient affecter la décision prise concernant la validité du plan. Avec la méthode développée ici, on peut conclure que l'IC ProfilerTM n'est pas un outil approprié pour l'acquisition des données de faisceau qui seront importées dans un TPS. Cependant, la méthode présentée dans cette thèse permet de prendre des données très rapidement (environ 3 mesures/minute). Utilisée avec l'ICP, cette méthode pourrait permettre de vérifier que les faisceaux de deux machines concordent, ou bien d'acquérir rapidement les données de référence pour l'assurance de la qualité. Outre le développement d'une méthode rapide d'acquisition de données, ce travail a aussi permis de caractériser certaines limites de l'ICP si on l'utilise pour la mise en service d'un linac.

TABLE OF CONTENTS

ACF	KNOV	VLEDGEMENTS	ii
ABS	TRA	CT	iii
RÉS	UMÉ		v
LIST	ГОБ	ABBREVIATIONS	ix
LIST	ГОБ	TABLES	x
LIST	ГОБ	FIGURES	xi
1	Intro	oduction	1
	1.1 1.2	Cancer	1 2
	1.3 1.4	Preparations for the Use of Linear Accelerators in Radiotherapy	7
	1.5 1.6	Rationale and Objectives	7 10
2	Back	ground	11
	2.1 2.2 2.3	Short Literature Review	11 15 25
		2.3.2 Analytical Modeling of Percent Depth Dose	30 31
3	Mate	erials and Method	33
	3.1	3.1.1 Plastic Used	33 33 34
	3.2	Method	37 37 45 55

		3.2.4 M	Iodel Vali	dation																	57
		3.2.5 B	eam Data	a and M	fodel	Con	npar	ison	s.												57
		3.2.6 C	omparison	n of Do	se Di	istrib	outic	ns .													59
4	Result	s and Dis	scussion .								•										62
	4.1	IC PRO	$FILER^{TM}$	^I Total (Corre	ected	Co	unts	Re	proc	duc	ibil	ity				 				62
	4.2		ng of Bea																		63
		4.2.1 IC	C PROFII	LER^{TM}	Cal	ibrat	ion										 				63
		4.2.2 C	ombination	on of M	easu	reme	$_{ m nts}$														70
			moothing																		72
			ercent De																		73
	4.3		Dose Fac																		74
	4.4		isons with																		78
	4.5		isons with																		81
	4.6		on of Bear																		81
			MV Mod																		81
			8 MV Mo																		84
	4.7		ed Dose I																		86
			alculated																		86
			alculated																		97
	4.8		ion Speed																		
J	G 1																				105
5	Conch	usion				• •					•			• •	•	•	 •	•	 •	•	107
	5.1	Method															 				107
	5.2		ent of ICF																		
	5.3	_	ces Betwe																		
	5.4		ty of Bear																		
	5.5				-																
Ann																					
App	endix F	1				• •		• •			•	• •			•	•	 •	•	 ٠	•	119
App	endix I	3															 •				116
App	endix (C																			119
App	endix I)																			125
App	endix I	E									•										131
Dofo	nonaaa																				199

LIST OF ABBREVIATIONS

3DCRT 3-Dimensional Conformal Radiation Therapy

AAPM American Association of Physicists in Medicine

CAX Beam Central Axis

DD Dose Difference

DICOM Digital Imaging and Communications in Medicine

DTA Distance To Agreement

DVH Dose Volume Histogram

EPOM Effective Point of Measurement

FDD Fractional Depth Dose

HMR Hôpital Maisonneuve-Rosemont

IC Ionization Chamber

 $ICP \quad IC \; PROFILER^{TM}$

IMRT Intensity Modulated Radiation Therapy

linac Medical Linear Accelerator

MLC Multi-Leaf Collimator

MU Monitor Unit

OAR Off-Axis Ratio (profile)

OF Output Factor

PDD Percent Depth Dose

PRF Pulse Repetition Frequency

PTV Planned Treatment Volume

QA Quality Assurance

RDF Relative Dose Factor

RT Radiation Therapy

SF Scatter Factor

SSD Source-Surface Distance

SWT Scanning Water Tank

TG Task Group

TPR Tissue-Phantom Ratio

TPS Treatment Planning System

LIST OF TABLES

<u> Fable</u>	Inst of Industry	oage
3-1	Initial parameters provided to the optimizer for the different beams for the analytical fit to PDD data	54
3-2	Metric definitions for PDD and OAR comparisons	61
4–1	Central detector total corrected counts variation over ten identical irradiations as given by the ICP software. σ refers to an estimation of the sample standard deviation.	. 62
4–2	Summary of acquisition data comparison between SWT and ICP for the 6 MV beam. For more detailed results, consult Appendix A	79
4–3	Summary of acquisition data comparison between SWT and ICP for the 18 MV beam. For more detailed results, consult Appendix B	79
4–4	Model-data comparisons for the 6 MV beam. For more detailed results, consult Appendix C	82
4–5	Model-data comparisons for the 18 MV beam. For more detailed results, consult Appendix D	82
4–6	Validation results for point measurements made in 6 MV beam using the clinical SWT model and the ICP model. The average absolute difference in percentage over all fields of a certain type between the TPS-calculated dose and the dose measured for the model validation field is shown	83
4–7	Validation results for scans made in the 6 MV beam using the clinical SWT model and the ICP model	83
4-8	Validation results for point measurements made in 18 MV beam using the clinical SWT model and the ICP model. The average absolute difference in percentage over all fields of a certain type between the TPS-calculated dose and the dose measured for the model validation field is shown.	85
4–9	Validation results for scans made in the 18 MV beam using the clinical SWT model and the ICP model	85

LIST OF FIGURES

$\underline{\mathrm{Figure}}$		page
1–1	Picture of an Elekta Synergy® (Elekta AB, Stockholm, Sweden) linear accelerator assembly [6]. Shown on the picture is the gantry, rotated slightly and the patient couch where the patient rests for the duration of the treatment	. 3
1–2	Picture of a PTW Freiburg MP3 scanning water tank system [9]. Shown on the picture are the water tank itself on a vertically-adjustable platform and the water reservoir and pump systems on the right.	. 6
1–3	Picture of the IC PROFILER TM [12]. The box-like structure in the lower left corner of the picture contains the control and measurement electronics of the device and may not be irradiated directly, under the primary beam. The active detection surface, or the panel, containing the four detector axes, is displayed on the upper right of the picture.	. 8
2-1	Close-up of the IC PROFILER TM 's surface	. 13
2-2	ICP calibration factors response relative to $4.9~\mathrm{cm}$ buildup calibration [15]	. 16
2–3	ICP profile agreement for (a) 6 MV beam (b) 18 MV beam. In the top right part of the graphs, the total amount of buildup is shown in terms of water-equivalent depth [15]	. 16
2–4	FDD agreement. (a) FDDs for a 6 MV $10 \times 10 \text{ cm}^2$ field. (b) Ratio of ICP FDD to CC13 FDD for three field sizes at 6 MV and 18 MV [15]. Note that in this figure, buildup must be interpreted as depth in the solid phantom, that is, it includes the ICP's inherent buildup and any additional material placed over the ICP	. 17
2–5	Output factors agreement. (a) OF measurements for square field sizes. (b) ICP OF measurements normalized to the OF obtained by different detectors for the reference $10 \times 10 \text{ cm}^2$ field [15]	. 18
2-6	(a) Sinusoidal perturbation applied to calibration procedure measurements. (b) Effect on resulting calibration factors after the wide field calibration procedure is done [13]	. 21
2–7	(a) Three calibration curves measured under an Elekta Synergy® linac. (b) Three calibration curves measured under an Varian Trilogy TM linac [13]	. 21
2-8	Effect on resulting calibration factors of using sidescatter during the calibration procedure [13]	. 23

2–9	example of a measured PDD for a 6 MV photon beam with a 10 × 10 cm ² field size at 90 cm source-to-surface distance. The measurement was conducted in water with a CC13 ionization chamber using a SWT system. The diagram on the right shows the measurement geometry. The curve is normalized to a value of 100 at the depth of maximum dose	27
2–10	Example of an inline measured profile for a 6 MV photon beam with a $20 \times 20 \text{ cm}^2$ field size at 90 cm source-to-surface distance. The measurement was conducted in water with a CC13 ionization chamber using a SWT system. The measurement geometry is shown on the right. The curve is normalized to a value of 1.0 at the position of the beam central axis	28
3-1	Screenshot of the IC PROFILER $^{\mathrm{TM}}$'s software	36
3-2	(Top) Photograph showing a typical centering of the ICP on the +8 cm detector. (Bottom) Photograph showing a possible measurement setup	38
3-3	Schematic diagram of the measurement setup. The numbers indicates the order of the measurements	39
3-4	Schematic diagram of the workflow for performing beam data acquisition for a single beam energy with the ICP. The plain arrows indicate the flow of information during the beam acquisition process. The dashed double arrow indicates the correspondence between the planned list of measurements and the DICOM step-and-shoot sequence	44
3-5	Example of the automatically detected transitions, indicated by vertical bars, for the beam central axis detector only in a 6 MV beam at 20 cm depth. The cumulative corrected counts are plotted on the top graph, while for reference the first and second derivatives are shown in the graphs below. All fields placed shortly after frame number 320 are wedged fields, which is why the height of the peaks in corrected counts rate is lower than in the first portion of the file since the delivered dose rate is lower.	48
3-6	Example of the top portion of a PDF report of a comparison between two acquisition data sets	60
4-1	6 MV calibration factors for the ICP Y-axis	63
4–2	Effect of applying calibration with the combination of half-profiles. Drawings on the graph show the two ICP positions used to measure the half-profiles (not to scale). The +Y and -Y labels indicate the orientation of the ICP's Y-axis linear array of detectors	64
4–3	(Top) Used calibration factors and mean calibration factors. (Middle) Ratio of used calibration factors to mean calibration factors for the 6 MV beam. (Bottom) The ten separate sets of calibration factors normalized to the mean calibration factors.	66

4–4	(Top) Used calibration factors and mean calibration factors for the 18 MV beam. (Middle) Ratio of used calibration factors to mean calibration factors. (Bottom) The ten separate sets of calibration factors normalized to the mean calibration factors.	67
4–5	(Top 6 MV Y-axis calibration factors measured with no additional buildup on the ICP with and without 3 cm tall sidescatter at the array ends. (Bottom) Ratio of calibration factors with sidescatter to those without it	68
4–6	(Top) 18 MV Y-axis calibration factors measured with no additional buildup on the ICP with and without 3 cm tall sidescatter at the array ends. (Bottom) Ratio of calibration factors with sidescatter to those without it	69
4-7	Shown here are two examples of pairs of half-profiles which will be combined together. The graph title shows the beam energy, field size, whether the field is wedged or open, the depth, the profile direction, the percentage difference between the total counts of the two measured half-profiles accumulated in the +8 cm detector of the ICP and the ICP acquisition mode. The difference should ideally and theoretically be zero. The legend lists measurement number followed by the file name where the ICP measurement was taken from in parentheses	71
4-8	Example of the effect of applying a pressure and temperature correction factor to half-profile measurements. The percentage difference of the beam central axis detector is given by the symbol δ on the graph titles	72
4–9	6 MV, $25\times25~\mathrm{cm^2}$ wedged profiles at 10 cm depth before and after smoothing	74
4-10	Results of the PDD fitting procedure on SWT data for open fields	75
4-11	Results of the PDD fitting procedure on SWT data for wedged fields	76
4-12	ICP-measured 6 MV output factors vs SWT-measured output factors	77
4-13	ICP-measured 18 MV output factors vs SWT-measured output factors	77
4–14	6 MV $40 \times 40 \text{ cm}^2$ open water phantom calculation. (Top) Reference distribution (SWT model). (Bottom) Dose difference	87
4–15	6 MV $10 \times 10 \text{ cm}^2$ open water phantom calculation. (Top) Reference distribution (SWT model). (Bottom) Dose difference	88
4–16	6 MV $10 \times 10 \text{ cm}^2$ wedged water phantom calculation. (Top) Reference distribution (SWT model). (Bottom) Dose difference	89
4–17	6 MV 8×8 cm ² MLC water phantom calculation. Collimation is provided up to 20×20 cm ² by the collimator jaws, with the MLC leaves further collimating the beam to a 8×8 cm ² square field. (Top) Reference distribution (SWT model). (Bottom) Dose difference	90
4–18	18 MV 40 × 40 cm ² open water phantom calculation. (Top) Reference distribution (SWT model). (Bottom) Dose difference	92

4–19 18 MV 10 × 10 cm ² open water phantom calculation. (Top) Reference distribution (SWT model). (Bottom) Dose difference
4–20 18 MV 10 × 10 cm ² wedged water phantom calculation. (Top) Reference distribution (SWT model). (Bottom) Dose difference
4–21 18 MV 8 × 8 cm ² MLC water phantom calculation. Collimation is provided up to 20 × 20 cm ² by the collimator jaws, with the MLC leaves further collimating the beam to a 8 × 8 cm ² square field. (Top) Reference distribution (SWT model). (Bottom) Dose difference
4–22 6 MV and 18 MV forward IMRT breast treatment plan dose comparison. (Top) Reference distribution (SWT model). (Bottom) 2 %, 0 mm γ comparison 98
4–23 DVH comparison for the 6 MV and 18 MV breast treatment plan 99
4–24 18 MV, 4 fields then 6 fields prostate treatment plan dose comparison. (Top) Reference distribution (SWT model). (Bottom) 2 %, 0 mm γ comparison 100
4–25 DVH comparison for the 18 MV prostate treatment plan
4–26 6 MV head & neck IMRT treatment plan dose comparison. (Top) Reference distribution (SWT model). (Bottom) 2 %, 3 mm γ comparison
4–27 DVH comparison for the 6 MV head & neck treatment plan

Chapter 1 Introduction

This chapter introduces, in simple terms a non-specialist should be able to understand, the subject of this thesis. As such, more details and in-depth definitions are found rather in the next chapters of this thesis than in this present chapter. The text starts by a brief discussion of cancer and then of radiation therapy and of its use in the treatment of this disease. Special attention is paid to linear accelerators, how their radiation beams need to be modeled to predict delivered dose and what this modeling usually entails. The chapter then provides some basic information on the IC PROFILERTM, a commercial product of Sun Nuclear corporation (Melbourne, FL, USA) used extensively in the project of this thesis. Additionally, it discusses objectives and rationale for this project. Finally, an overview of the structure of the thesis is presented.

1.1 Cancer

The word cancer is used to denominate many different specific diseases; other designations for it are malignant tumors and neoplasms. These all have in common an abnormal and malicious division of cells. This can occur in any part of the body, and different cancers usually involve different types of cells. The cause is damaged DNA strands leading to the abnormal cell reproduction. The DNA damage itself may be inherited, or caused by environmental factors or lifestyle choices. For example, one of the most common cancers in the world is lung cancer, often linked to the smoking of tobacco. The two other most common cancer treated in North America are breast cancer and prostate cancer. Work exposure to carcinogenic substances, lack of physical exercise, infections and alcohol abuse are other common causes [1, 2].

Cancer already represents the most significant cause of death in the world, accounting for 13 % of all deaths (although in some developed countries, heart disease is the leading cause of death). The global number of cancer-related deaths is expected to increase to approximately a rate of 11.5

million deaths per year by 2030. This increase is largely due to the global increase in population, and its aging [3]. An estimated 75,000 people died from cancer this year in Canada only [4]. While there is a large on-going effort to focus on cancer prevention [5], rather than strictly treatment, cancer treatment modalities are not forecasted to go out of favor. Rather, it is expected that their use will grow, as the total number of cancer cases grows.

1.2 Radiation Therapy

Radiation therapy (RT), or radiotherapy, is one of several available therapies used in the treatment of cancer. It accounts, together with surgery and chemotherapy, for the most used modalities in the treatment of cancer. Note that while RT is mostly used in the treatment of this disease, it also can be applied to treat other ailments.

Radiotherapy techniques can be classified into two branches: brachytherapy, in which radioactive sources are used in close proximity to tumors (often placed inside the body near the tumor) and external beam therapy, where a radiation source is used from outside the patient. In the latter case, the source often consists of a cobalt-60 radioactive source emitting gamma rays or of a high energy electron beam impinging on a small metallic target. Radiation is then produced in the form of X rays as a result of electron-nuclei interactions (by way of a process called bremsstrahlung). This form of therapy is sometimes called photon therapy. The electron beam can also be used directly as a source of radiation after it is transmitted through a scattering foil, in which case we term it electron therapy. The production of high energy electron beams necessary for photon therapy or electron therapy is achieved by the use of linear accelerators (linacs). Figure 1–1 shows a picture of a linac. Less commonly, heavier particles such as protons or carbon ions are also used in the treatment of cancer.

In external beam radiotherapy, collimated fields of radiation of varying duration and/or intensity are aimed at the cancerous mass in the patient, usually from several angles. In simple terms, the goal is to obtain a distribution of radiation dose high enough to kill cancer cells in the target area, while minimizing damage to healthy tissues.



Figure 1–1: Picture of an Elekta Synergy® (Elekta AB, Stockholm, Sweden) linear accelerator assembly [6]. Shown on the picture is the gantry, rotated slightly and the patient couch where the patient rests for the duration of the treatment.

3-dimensional conformal radiotherapy (3DCRT) represents a treatment technique where collimated beams of radiation are designed by the treatment planner to conform the dose distribution to particular contours, or volumes, within the patient geometry (e.g. obtained from computed tomography scans). A common and simple form of 3DCRT is to define static (non-varying) beams of radiation that, in combination, yield the desired dose distribution: so-called "forward planning".

There exist more complex forms of 3DCRT, such as "inverse planning", where the beam geometries are decided from an optimization algorithm that strives to deliver a dose distribution corresponding to pre-defined constraints imposed on patient contours. Moreover, static beams are not used in inverse planning. Rather, their intensity is dynamically modulated during treatment by moving collimating equipment, varying beam geometry and/or delivered dose rate. This last technique is called intensity-modulated radiation therapy (IMRT). IMRT is often delivered in a

so-called "step-and-shoot" fashion, where the linac alternates between varying the beam geometry automatically and delivering radiation. Another form of IMRT is arc therapy, where beam geometry is varied simultaneously as radiation is delivered, contrary to the step-and-shoot approach.

1.3 Preparations for the Use of Linear Accelerators in Radiotherapy

Linear accelerators are extremely complex machines, designed to deliver dose distributions that can be predicted accurately to about 5% uncertainty [7]. To attain this level of confidence in predicted delivered dose is not an easy task and requires several steps.

After the initial installation of the linac, it must undergo acceptation, where the machine itself and its bunker (the radiation-attenuating walls surrounding the linac) undergo tests to ensure that they conform to certain specifications of quality and radiation safety.

A computer model able to predict dose reliably, given a treatment plan and a patient geometry, must also be made. This task, called beam modeling, usually requires a set of typical radiation measurements to be collected, ensuring that the model built on the computer is able to reproduce experimental observations reasonably well. Other more complex measurements are then used to confirm that the beam model characterizes well the radiation emitted by the linac. This is called model validation.

Finally, the linac is put to clinical use. A proven and well-established radiotherapy protocol must be followed. Patient positioning and contention must be ideal. Machine calibration must be performed with high precision, establishing a known dose rate under reference conditions. The delivered radiation dose distribution must be tailored to eradicate cancer cells inside the tumor volume without damaging healthy tissue as best as possible.

As is standard practice in radiotherapy departments, liquid water is used as a phantom material to simulate the human body receiving radiation. Depending on the tissue type in the human body, water content by mass varies from about 20 % to 80 %. On average in the whole body, water content by mass is about 55 %. This proportion raises to 70 % when considering only fat-free tissues [8]. The availability, reproducibility and high body content of water explains its choice as a the standard phantom material for dose measurements for radiotherapy.

The choice of water as a phantom material explains why scanning water tanks represent one of the most common equipment used in characterizing a medical radiation beam. In a scanning water tank (SWT) system (an example is shown in figure 1–2), a water-proofed radiation detector is moved (scanned) in water through a radiation beam by a calibrated robotic arm, so that the detector location relative to an arbitrary origin is known. Radiation beam intensity relative to a reference position can then be plotted along any axis accessible to the SWT mechanism. These radiation or beam "profiles" consist most of the desired data when using a SWT system. Point measurements, in which the SWT arm is not scanned but rather remains stationary in the water tank can also be made.

Data measured in such SWT systems is used extensively as building blocks for beam models used in treatment planning systems (TPS), and for linac calibration. It is important to understand that the beam model is created from a set of measurements with given beam geometries, but should allow dose predictions for different beam geometries, ideally any beam geometry the linac assembly is capable of delivering. This is why beam models must be validated with geometries falling outside the set used in creation of the model in the first place.

The TPS beam model then allows one to predict, within uncertainties, dose received by a patient for a given treatment plan. The time-consuming process of gathering all data necessary for creating beam models is referred to as beam acquisition or beam data commissioning [10]. It usually is a necessary task when an accelerator is first put into service in a radiotherapy clinic. Sometimes, a beam model may already be provided by the linac manufacturer or a clinic may decide to use the same beam model for different accelerators of the same type and manufacturer. In these cases, the model still has to be validated by measuring all or a selected subset of the beam data and by comparing the measurements to the model predictions [10].

Similarly for machines which do not come with a model, once the necessary data are gathered, a beam model in the TPS may then be created and validated with further measurements. This model validation is done to ensure that the TPS and the beam model are able to predict dose distributions resulting from radiation fields that were not used to create the model in the first



Figure 1–2: Picture of a PTW Freiburg MP3 scanning water tank system [9]. Shown on the picture are the water tank itself on a vertically-adjustable platform and the water reservoir and pump systems on the right.

place. To accomplish this, measurements are made with the SWT once again and the results are compared to the TPS model predictions.

Finally, to keep linacs from deviating too far from the expected performance levels, they must be monitored at regular intervals of time for such deviations. We refer to this process as quality assurance (QA). Because many QA tasks are repetitive, that is to say they must be repeated often, at short time intervals, tools specific to radiotherapy QA have been developed. These are often devices that have a specific purpose and allow time savings when compared to the use of more general purpose equipment for QA tasks.

1.4 Introduction to the IC PROFILERTM

The IC PROFILERTM is a radiotherapy quality assurance tool used for linear accelerator beam profile measurements during the phases of the initial linac installation and periodic QA tests thereafter. It is intended to replace a scanning water tank for these purposes. The IC PROFILERTM is however *not* intended for acquiring data used as input to radiotherapy treatment planning systems (TPS) beam models [11].

In contrast to the SWT which, usually, uses only one radiation detector, the IC PROFILERTM is a matrix with many embedded radiation detectors, in this case ionization chambers (IC). ICs are cavities filled with an ionizable material, usually a gas or liquid. Most often, air is used. Electrodes are placed in a cavity which apply an electric field across it. The ions (i.e. charged particles) created by the interactions of the radiation with the cavity material are collected by one of the electrodes. Connecting the ionization chamber to an electrometer allows us to measure the ionization charge resulting from an irradiation.

In the IC PROFILERTM, ICs are placed at regular intervals along four linear axes inside its panel. Therefore, by placing the IC PROFILERTM under a radiation beam, the beam intensity profile may be measured by using the signal coming from each IC for every axis. A disadvantage is that the axes are fixed and that their positions cannot be changed remotely from outside the radiotherapy bunker. Furthermore, the spatial sampling (i.e. detector spacing) on the IC array may be coarser than what is achievable using the SWT. However, profile measurement is faster with the IC PROFILERTM than with the SWT, especially when considering the time required to set up the SWT under the radiation source. This makes the IC PROFILERTM attractive for use in regular QA tests, where one can rapidly evaluate how uniform (flat) and symmetric beam profiles are.

1.5 Rationale and Objectives

It is estimated that photon beam acquisition takes 15 hours per beam energy available on a linac [10]. All in all, for an accelerator providing multiple beam energies, there are thousands of lateral (left to right, back to front in the SWT) beam profiles to acquire: one for each beam energy, field size and depth in water, both for open (unfiltered) and wedged (where the beam is



Figure 1–3: Picture of the IC PROFILERTM [12]. The box-like structure in the lower left corner of the picture contains the control and measurement electronics of the device and may not be irradiated directly, under the primary beam. The active detection surface, or the panel, containing the four detector axes, is displayed on the upper right of the picture.

attenuated, or filtered, with a triangular prism) fields. Percent depth dose (PDD), which describes the variation of the radiation dose with depth in the phantom along the beam central axis, must also be measured for each combination of field size and beam energy. More measurements have to be made to calculate relative dose factors. These describe the dose delivered at a reference point by a particular radiation field configuration relative to the dose delivered by a field of reference at the same point (and under certain specific reference conditions for the measurement of this dose). It is the large quantity and the required high quality of all these measurements that make beam commissioning a daunting task.

If data acquired with the IC PROFILERTM can be shown to be equivalent to data acquired with a SWT and, moreover, models respectively built from IC PROFILERTM measurements and SWT measurements shown to be equivalent, then considerable time savings can be gained at the time of commissioning by using a detector array, such as the IC PROFILERTM (also referred to

as ICP in this text). Alternatively, if it is shown to be possible, the ICP could be used for spotchecking and validating ready-to-use beam models provided by manufacturers. It could also be used for machine matching, where the ICP would be used to verify a linac matches within certain limits another well-characterized linac.

It can thus be said that the first goals of this project were to investigate if performing beam commissioning with the IC PROFILERTM is possible at all and in the process see if any gains can be made in terms of measurement time. Pending this initial investigation, a further goal of this project was to validate a method of beam data acquisition with an array of ionization chambers in replacement of the traditional scanning water tank measurements. The project was carried out for photon beams only of energies 6 MV and 18 MV; a later project may be needed to investigate electron beam commissioning with an IC array. Specific objectives were as follows:

- 1. Find a suitable measurement setup to acquire beam data with the ICP that reproduces beam data acquired with a SWT. In particular, large fields (e.g. ≥ 40 × 40 cm²) and small fields (≤ 5 × 5 cm²) profiles must be measured with the ICP. These tasks represent a challenge since the active area of the ICP is only 32 cm wide and the detector volume and detector spacing are both relatively large in respect to what is normally used to measure small fields.
- 2. Show that beam data acquired with the ICP is equivalent to beam data acquired with a SWT or, alternatively, evaluate to what degree it is able to reproduce SWT measurements.
- 3. Build a beam model solely from beam data acquired with the ICP.
- 4. Validate the ICP beam model with validation field measurements in SWT.
- 5. Investigate if the ICP beam model is equivalent to the clinical model, built from SWT measurements and highlight any differences found between the two.
- Assess if model differences could have a clinical impact by comparing dose distributions from water phantoms or treatment plans in the treatment planning system.
- Evaluate the reductions in beam acquisition time allowed by the use of the ICP instead of a SWT.

1.6 Structure of Thesis

This chapter introduced the subject of this thesis and rationale behind this work.

In the next chapter, some important technical details regarding the ICP are introduced and a short literature review is made. Linac commissioning, analytical expressions for percent depth dose and dose distribution comparison tools are also discussed.

The third chapter discusses the materials and the method used in performing beam acquisition with the ICP, in beam modeling and in making comparisons with SWT measurements and the SWT-based model used in the clinic.

In chapter 4, results are presented and discussed.

The final chapter summarizes the work, draws conclusions from the results and provides an outlook for future work.

Chapter 2 Background

This chapter first presents a short literature review on the IC PROFILERTM. Some background information is then presented on quantities, techniques and methods of interest in this project. The intent is to provide information that is useful in understanding the method described in chapter 3 and the results presented in chapter 4. Some of the theory presented should already be familiar to a trained medical physicist. However, for completeness, all concepts or quantities used extensively throughout this project are still defined explicitly.

Before the literature review, a section of the text is devoted to a more detailed description of the IC PROFILERTM than what was presented earlier. The details discussed there are very useful in understanding the published literature on the ICP, as well as understanding the method presented in chapter 3 and the results presented in chapter 4.

2.1 Complementary Information Regarding the IC PROFILERTM

As mentioned in chapter 1, the IC PROFILERTM is an ionization chamber array intended to replace the scanning water tank (SWT) for linac beam measurements during bunker testing, field service and periodic quality assurance (QA) of installed machines. The major advantages of using the ICP for these tasks are that setup time and measurement time are short, and that the beam profile can be viewed in real-time. This allows easier monitoring of beam constancy and beam steering than scan data would allow. Beam flatness, beam symmetry, field size, beam center, penumbra width and light-radiation coincidence can all be evaluated with the ICP.

The ICP comprises 4 linear arrays of detectors labeled Y axis, X axis, positive diagonal (PD) axis and negative diagonal (ND) axis (these are simply names given to the different axes in the ICP's panel; they should not be interpreted as being oriented along any specific direction relative to a linac room space reference frame). The axes all share a common detector in the center of the

matrix. The detectors along the X and Y axes span a length of 32 cm, while the PD and ND axes span 45 cm. The area covered by the detectors is 32×32 cm². The detector pitch is 0.5 cm on the X and Y axes while it is 0.707 cm on the PD and ND axes. Each cavity is air-filled and 0.075 cm³ in volume.

Inherent polycarbonate buildup plates of 0.9 cm and 2.3 cm (water-equivalent thickness, manufacturer specifications) are respectively placed above and under the detectors. Thus, to approximate a depth z in water, one should place a water-equivalent buildup of thickness z - 0.9 cm over the ICP's surface. A more precise determination of this depth correction would require a measurement of the ICP chamber's effective point of measurement (EPOM). The correction presented here was verified to be valid based on measured field size with the array, versus the expected field size. A thin plate with drawings of the chamber locations and with alignment marks covers the array's surface. Figure 2–1 shows a close-up picture of the IC PROFILERTM.

The ICP (sometimes referred to in this text as "the panel") must be calibrated to compensate for the relative differences in sensitivity of its detectors – mainly caused by differences in scattering conditions, variations in geometric parameters and electrical wiring from detector to detector. Here, the term calibration is understood to mean the set of correction factors applied to the detectors on an ICP axis relative to a reference detector on that axis. For all detector axes of the ICP, the central detector of the panel is used as reference and its calibration factor is thus 1.000 (this detector is common to all axes). Other detectors may have calibration factors that differ from 1.000 by a few percent. The calibration factors may be applied before initiating measurement with the ICP software or, alternately, after all beam data collection is done by applying the factors to the recorded data.

The calibration procedure used is the wide field array calibration method, described in detail in [13] and implemented in the IC PROFILERTM software. This procedure involves measuring a field covering the array entirely but not irradiating the electronics section of the ICP, say a 35×35 cm² field in different ICP orientations and positions.

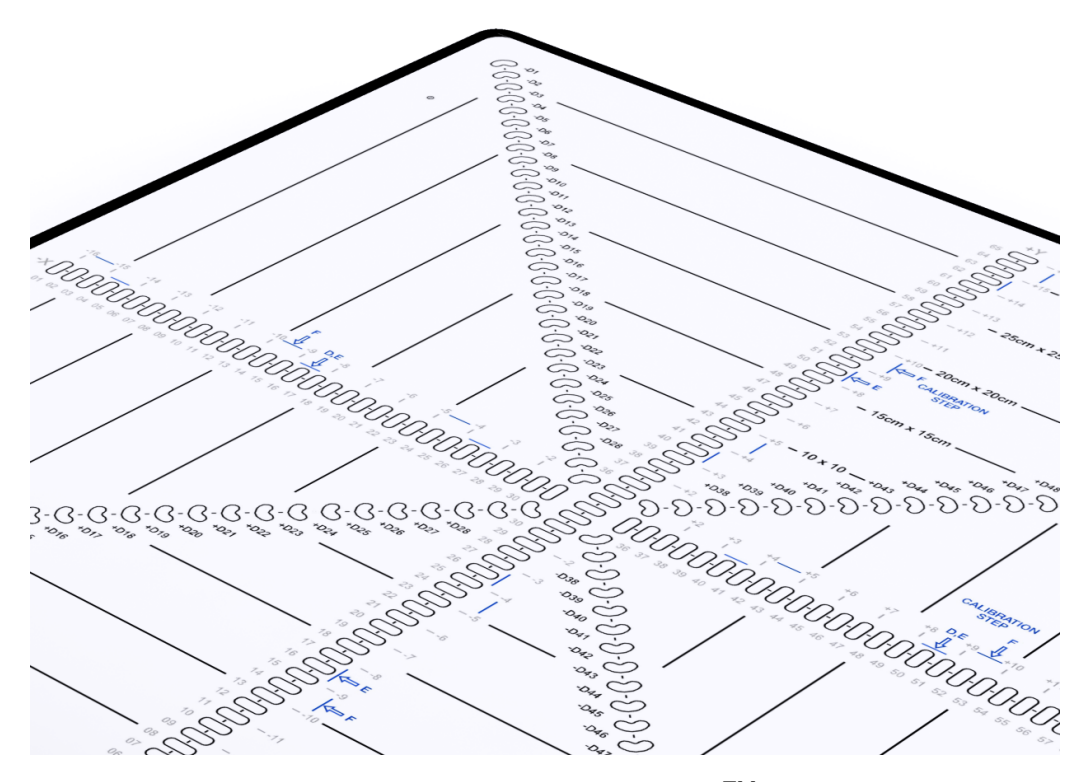


Figure 2–1: Close-up of the IC PROFILER $^{\mathrm{TM}}$'s surface.

The panel can acquire measurements in two modes: pulsed and continuous. In pulsed mode, trigger diodes embedded in the ICP's inherent buildup detect a linac's pulses. This allows measurement updates to be synchronized to fall in-between linac pulses. This is important, because measurement updates made during a linac pulse may cause ionization created by that pulse to go partially undetected. Indeed, as capacitors are discharged to measure ionization in the cavities, they are not able to accumulate charge. Any ionization created during the capacitor discharge time will not be measured.

The continuous mode is on the other hand simply clock-synchronized, with measurement updates occurring at a time interval adjustable from 125 ms to 800 ms. This mode should be used with continuous radiation sources, rather than pulsed, such as a cobalt-60 source. The continuous mode can be used with a pulsed source, but the possibility that measurement updates will occur during linac pulses means that the total effect of the pulsed radiation delivered will not be detectable.

Every time a measurement update occurs, the capacitors storing the charge released in each cavity are discharged. The charge is split into counts. The counts are determined by an analog-to-digital converter. Each count represents a fixed amount of electric charge, which is determined by the specific chip used by Sun Nuclear corporation in the ICP readout circuitry. The number of counts counted during the measurement update is sent to the ICP software by a cable. The ICP software then corrects the raw counts sent from the device for background, leakage and by applying calibration factors for each cavity. The final result is what is termed "corrected counts" in the ICP software and represents the quantity of interest used in this project to perform beam data acquisition. The corrected counts are calculated as follows [14]:

$$cc_i(t) = \left(\frac{rc_i(t) - t \times l_i}{g}\right) \times CF_i,$$
 (2.1)

where $cc_i(t)$ are the total cumulative corrected counts for detector i at time t and similarly with $rc_i(t)$ but for raw counts. l_i is the leakage rate for detector i in raw counts per "time tick", the unit of time used internally in the ICP software. t is therefore measured in time ticks. l_i is measured for each detector before the start of acquisition, when the ICP is instructed to measure background and is assumed constant throughout the measurements that follow until another background measurement is initiated. g is the gain multiplication factor (the ICP can apply a gain multiplication factor of 1, 2, 4 or 8 on the ionization signal obtained from its cavities). CF_i represents the calibration factor for detector i.

Note that in one article [15], it is indicated that a pressure-temperature correction factor ($P_{T,P}$) is used in the calculation of corrected counts (the ICP is equipped with a transistor for monitoring temperature and a transducer for monitoring pressure). However, the ICP software's online help contradicts this fact and states that the corrected counts are calculated as shown in equation 2.1 [14]. Tests later made (with results presented in chapter 4) indicated that the software's online help was correct in stating that no correction was actually being applied.

The resulting total corrected counts for each detector can be plotted against detector position to obtain beam profiles. The total corrected counts recorded at time t can be subtracted from the

total corrected counts recorded for a later time ($t+1\times$ "time tick") to obtain a nearly instantaneous view of the profile shape.

2.2 Short Literature Review

Few published articles could be found that directly discuss the IC PROFILERTM. The two main ones will be discussed here.

Simon et al.: Characterization of a multi-axis chamber array

In this article [15], the authors describe the goal of their work as being to evaluate a detector array having the potential to simplify beam acquisition. The authors acknowledge the potential of the ICP for this purpose, although without testing it out fully in a beam acquisition process (like it was done for this thesis). The tests performed by Simon et al., however, are interesting in that they provide a sense of how the ICP behaves as a radiation detector.

The authors start by evaluating measurement reproducibility. They choose a Co-60 source for this test because of its highly reproducible nature, rather than a linac. Because of the choice of this source, they also choose to operate the ICP under its continuous acquisition mode. As a result, they evaluate the ICP reproducibility under this acquisition mode and omit to test the reproducibility of pulsed acquisition. This can be criticized because it is expected that the ICP will be used much more to measure linac beams rather than Co-60 beams in modern clinics.

They measure short-term reproducibility by exposing the ICP with 10 consecutive 1 minute irradiations, with only the center 45 seconds being used, disregarding any variation due to source travel. The reproducibility was then quantified by determining the standard deviation of total corrected counts for each detector and then taking the maximum deviation from the mean. They obtain a maximum deviation from the mean of 0.15 %.

The measurement of calibration factors for the different detectors of the array is used by the authors to evaluate energy dependence. The fact that the measured calibration factors differed by nearly 1.5~% for some detectors showed that it is necessary to perform a calibration for each beam energy.

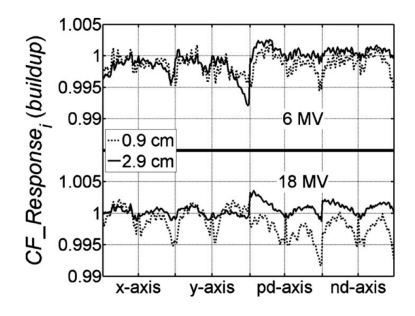


Figure 2–2: ICP calibration factors response relative to 4.9 cm buildup calibration [15].

The effect of using 2 cm or 4 cm additional buildup on top of the inherent 0.9 cm during calibration was also studied. The obtained calibration factors differ from the 0 cm additional buildup calibration factors. The calibration factor response relative to a 4.9 cm buildup calibration is displayed in figure 2–2. The authors state that since over 97 % of the detectors fall within calibration factor reproducibility, a single calibration file can be used for a range of buildup values.

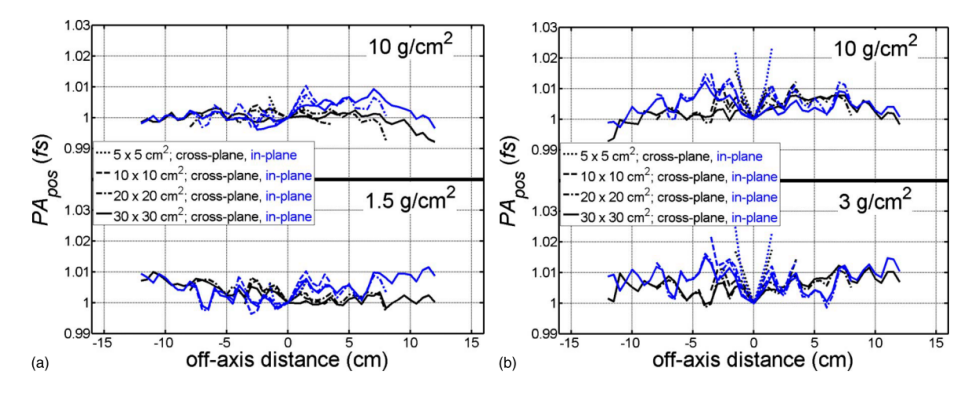


Figure 2–3: ICP profile agreement for (a) 6 MV beam (b) 18 MV beam. In the top right part of the graphs, the total amount of buildup is shown in terms of water-equivalent depth [15].

Figure 2–3 shows profile agreement between the ICP and a SWT. The plotted lines correspond to ICP measurement ratio to CC13 measurement in a water phantom. The difference between the two systems is typically on the order of 1.5 % and biased towards positive errors. The authors mention that the bias is a result of the combined error in measurement and error on the central detector's calibration, to which all calibration factors for the other detectors are normalized.

One observation that can be made is that the agreement for small fields is worse than for large fields. Only two different depths are evaluated at each energy. Furthermore, since only 80 % of the field width is used for the comparison, we are unable to see the agreement in penumbra and umbra for these graphs. These regions of beam profiles are *essential* to measure when doing beam acquisition, because many beam model parameters are derived from them. No wedged fields comparisons are made either. It is therefore interesting to investigate these comparisons that were omitted from the article if one wants to use the ICP for beam commissioning.

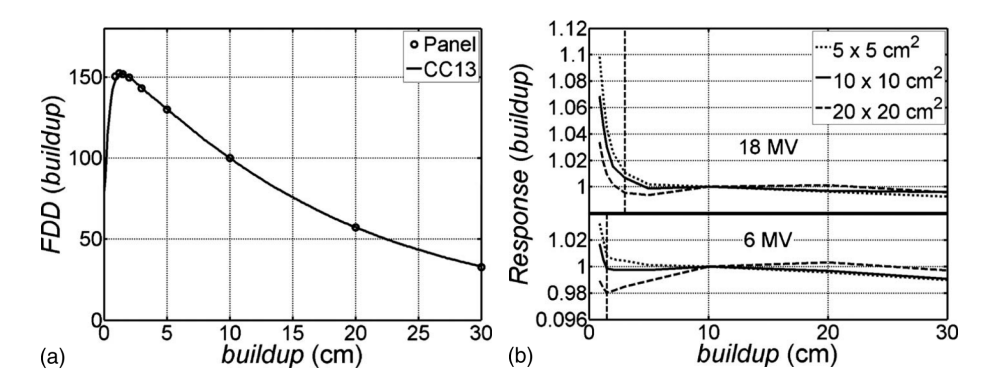


Figure 2–4: FDD agreement. (a) FDDs for a 6 MV 10×10 cm² field. (b) Ratio of ICP FDD to CC13 FDD for three field sizes at 6 MV and 18 MV [15]. Note that in this figure, buildup must be interpreted as depth in the solid phantom, that is, it includes the ICP's inherent buildup and any additional material placed over the ICP.

Simon et al. also compared fractional depth dose (FDD) curves between ICP and CC13 in a SWT. FDDs are similar to PDD curves, but normalized at some depth possibly different than the depth of dose maximum. The SSD to the buildup surface was set at 90 cm. The comparison is presented in figure 2–4. The authors state that, outside the buildup region, agreement is generally within \pm 1 %, with greater differences occurring for the shallow regions of the 20 × 20 cm² 6 MV beam, the largest field size used. Under these conditions, an under-response of about 2 % occurs near z_{max} .

The authors continue by mentioning that by 5 cm of buildup, the ICP agrees with the CC13 within \pm 1 %, yet they do not mention to which depth their FDD is normalized. Consulting figure 2–4 (b), it seems reasonable to conclude that 10 cm was chosen as normalization depth. It is

therefore natural that differences between the two systems should diminish as we approach this depth.

A mention is made that larger field sizes ($30 \times 30 \text{ cm}^2$ or more) were not included in their study because of "increased measurement noise due to electronic cross-talk" [15]. They attribute this to "increased scatter entering the panel's electronics due to the larger field size [...] and increased secondary scatter from the buildup" [15]. They warn that "one should be aware of this possibility when measuring larger field sizes in conjuction with a substantial amount of buildup" [15].

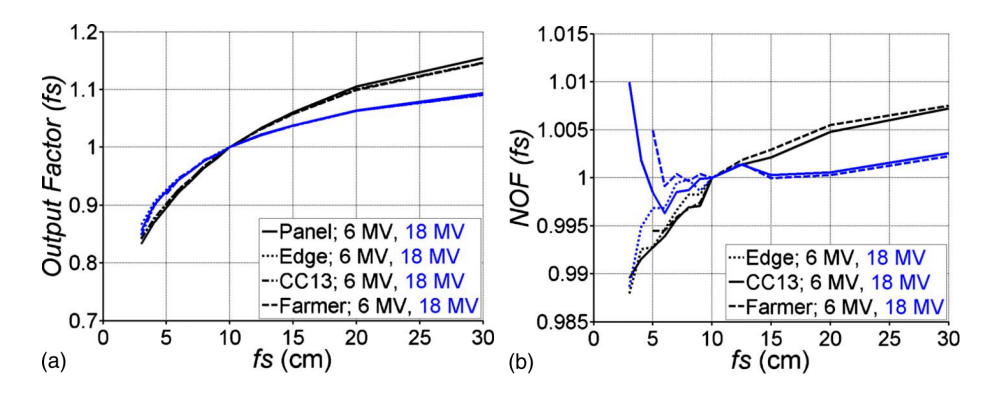


Figure 2–5: Output factors agreement. (a) OF measurements for square field sizes. (b) ICP OF measurements normalized to the OF obtained by different detectors for the reference $10 \times 10 \text{ cm}^2$ field [15].

As for output factors, Simon et al. measure them for 6 MV and 18 MV at several field sizes, starting with 1×1 cm² up to 30×30 cm², for 10 cm depth at 90 cm SSD. They choose to exclude from their graphs the results obtained for fields smaller than 3×3 cm², citing that the difference was superior to ± 1.25 %, while it remained within that margin for the other field sizes.

For small field sizes $(5 \times 5 \text{ cm}^2 \text{ or less})$, we observe on figure 2–5 that the ICP underestimates OFs compared to the EDGETM (Sun Nuclear corporation, Melbourne, FL, USA) detector, which is a small-volume shielded diode, and this, at both 6 and 18 MV. For large field sizes $(15 \times 15 \text{ cm}^2 \text{ or larger})$, the ICP overestimates OFs when compared to all other detectors and by a larger amount at 6 MV than at 18 MV. The authors offer no specific explanation as for the reason behind the differences, except perhaps for the warning about increased scatter resulting from the use of large amounts of buildup mentioned earlier.

In summary, the article provides a sense of how closely the ICP is able to reproduce SWT measurements. The authors' opinion is that the results are indicative of the array's abilities in beam data collection, with a strong potential benefit in acquisition time reduction. The subject of this thesis was to further test these abilities to assess the IC PROFILERTM in a beam acquisition context.

Simon et al.: Wide field array calibration dependence on the stability of measured dose distributions

Simon et al. discuss in this article [13] the method by which the IC PROFILERTM is calibrated using the software provided by Sun Nuclear corporation. The method is derived in detail in a patent [16] and is generalizable to other detector arrays. The idea is to determine the relative sensitivities of the detector by substituting them at different locations in the radiation field.

For a linear array, the wide field array calibration method requires measurements to be made in three separate array configurations. These are termed α , θ and λ by the authors. α represents a measurement taken with the array centered with the linac's crosshairs. θ is a measurement taken with a 180° rotation from the α configuration. Finally, λ is a measurement taken with the array translated one detector spacing from the θ configuration. The field size used must cover all detectors. Furthermore, it is highly desirable that no detector reside in a high dose gradient region, such as a beam penumbra, so that small errors in array positioning have only a minor impact on the resulting measured calibration factors.

The wide field array calibration method is based on three postulates, or assumptions [13]. Firstly, it is assumed that the dose delivered during each irradiation of the calibration process does not vary. Secondly, we assume that the relative sensitivities of the array's detectors does not change throughout the calibration procedure. The last assumption is that the different positions and orientations of the ICP offer the same scattering conditions in the linac space reference frame.

In practice, all three assumptions are likely to be false, but to varying degrees. The third assumption represents the most obvious case of failure. In fact, we know it to be false because of several factors. To start with, the ICP is inherently asymmetrical; one side of the Y axis is adjacent

to the ICP electronics box, which no doubt contains many plastic and metallic parts. The opposite side of the axis marks the end of the array.

Another important factor is that scattering conditions are certainly changed as the ICP is translated and rotated during the calibration procedure. For instance, a cavity placed near the end of an ICP axis may be substituted for another cavity that has more sidescattering material from one calibration step to the next. In their article [13], Simon et al. acknowledge this problem, and mention that including a specially cut piece of PMMA around all edges of the array reduces error associated with changes in scattering conditions.

Much of the work the authors undertake for this article is devoted to examining the effects of postulate failures. To do so, they use only the IC PROFILERTM's Y-axis, a linear array of detectors, but they mention that their investigations would also apply to the other axes of the device, or other linear arrays.

They tested the effect of small symmetry variations in the beam profile, from one irradiation to another, which represents a violation of the first postulate. In a numerical simulation of array calibration, they deliberately introduce a small sinusoidal perturbation of either measurement α , θ or λ . The pertubation takes the form of:

$$p(y) = 0.001 \sin\left(\pi \times \frac{y}{32 \text{ cm}}\right) + 1,$$
 (2.2)

where $y \in \{-16.5, -16, -15.5, ..., 16\}$ cm. The perturbation is maximal at the array ends and is valued at ± 0.1 %.

The perturbation itself and its effect on either the α , the θ or the λ measurement are shown in figure 2–6. In this figure, p_error_n(cf_X, cf) refers to the percent error of calibration factors of a perturbed calibration measurement to an unperturbed one, that is, for example:

$$p_error_n(cf_{\alpha}, cf) = \left(\frac{cf_{\alpha}}{cf} - 1\right) \times 100.$$
 (2.3)

 cf_{α} refers to the resulting calibration factors when the α measurement is perturbed but the θ and λ measurements are left undisturbed. cf refers to the set of the final obtained calibration factors after the wide field calibration procedure is done. n is an index identifying the detector within the array.

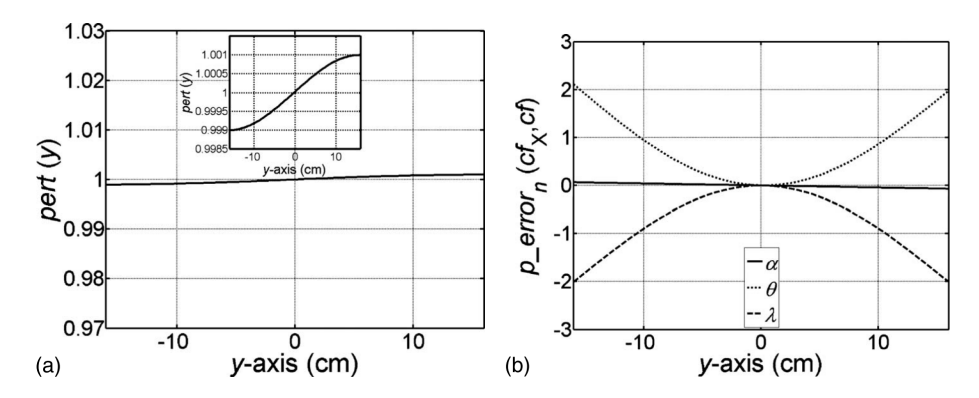


Figure 2–6: (a) Sinusoidal perturbation applied to calibration procedure measurements. (b) Effect on resulting calibration factors after the wide field calibration procedure is done [13].

The horizontal axis used in figure 2–6 is in centimeters and the curves are plotted such that the nth point of p_error_n is aligned with the corresponding position for detector n in the linear array.

This test shows how a minor variation in beam symmetry for one of the measurements during the calibration procedure can have a significant impact on the curvature of the resulting calibration curve. The effect is dominant at array ends. At these positions, errors in calibration factors go up to 2 %, even if only a 0.1 % perturbation on the signal was applied. Such a small symmetry variation is rather insignificant in clinical practice, yet it affects calibration factors in such a way that measured beam profiles measured with the ICP can be visibly distorted from beam profiles measured with a scanning water tank system.

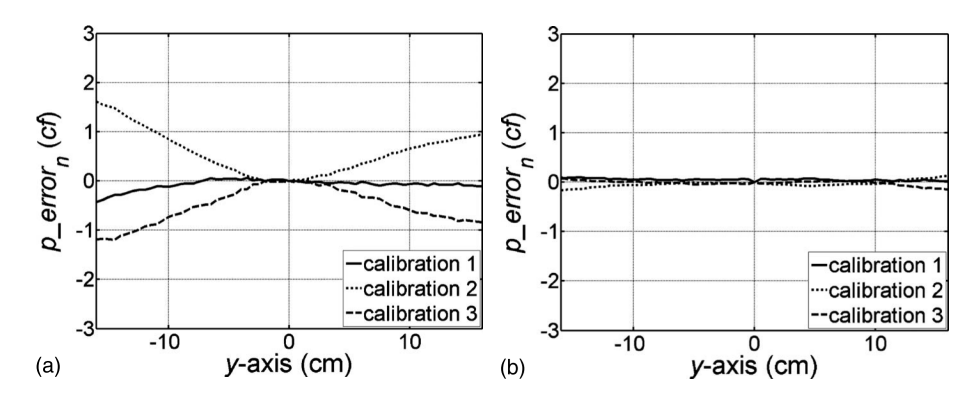


Figure 2–7: (a) Three calibration curves measured under an Elekta Synergy® linac. (b) Three calibration curves measured under an Varian TrilogyTM linac [13].

The overall shape of the resulting calibration curves is quite similar to that which is presented in the left graph of figure 2–7. In this figure, Simon *et al.* show both calibration factors measured under an Elekta Synergy® linac and a Varian TrilogyTM linac (Varian Medical Systems, Inc., Palo Alto, CA, USA). The calibrations measured under the Elekta machine clearly exhibit a much wider spread than the ones measured under the Varian machine, going from ≈ -1 % to $\approx +1.5$ % at one array end.

To limit the effects of violations of the first postulate, Simon et al. keep the radiation beam continuously on and use a remotely operable linear stage to move the panel for the θ and λ measurements, while standard beam cycling (on and off) is used for the α measurement. As seen in figure 2–6, a symmetry perturbation of the α measurement does not affect importantly the resulting calibration curve, meaning the wide field calibration algorithm is fairly immune such perturbations of the α measurement [13].

There are also a few steps that can be taken to limit the effects of violations of the second postulate, which states that the relative sensitivities of the detectors should remain constant throughout the calibration process. The two main things that can be done are to store the ICP in its calibration environment and keep it connected to the power cable, so that it is under constant power supply [13]. The idea is to limit temperature variations during the calibration process due to temperature gradient between the ICP's parts and the external environment.

The third postulate assumes that the array's movement within the radiation field does not change the scattering conditions encountered by the detectors. The ICP is radially symmetric about its central detector [13]. However the array is *not* radially symmetric about any other of its detectors. It is therefore straightforward to assume that scattering conditions do indeed change upon a translation of the array, for most detectors on the array.

This is even more so for detectors at distal ends of the array. Detectors near the negative end of the ICP's Y-axis are placed next to the box that contains the control electronics of the ICP. The detector at the positive end of the Y-axis is placed a short distance away from the physical end on the ICP's panel (1.5 cm) and thus experiences less sidescattering than the detectors placed near the electronics box, which is over 14 cm wide.

In order to reduce this discrepancy, they conduct the calibration procedure using extra sidescattering material placed all around the ICP panel, except on the side where the electronics box is. A machined $4 \times 4.2 \text{ cm}^2$ (width \times height) acrylic border was used. The authors state that the width was chosen to match the scattering conditions near the negative end of the ICP's Y-axis [13]. As was just mentioned in the previous paragraph, however, the electronics box is much wider than 4 cm, which might imply that ≈ 4 cm scattering material is located inside the box. The height of the border was chosen to match the height of the panel with the additional 1 cm buildup the authors used during their tests. While using this additional sidescattering material might reduce the violations of the third postulate, they will in no case be entirely eliminated.

The authors evaluate the effect of using sidescatter or not during calibration by averaging five separate calibrations with and without it and then taking their ratio:

$$\operatorname{agreement}_{n}\left[\left\langle \operatorname{cf}_{\operatorname{ss}}\right\rangle ,\left\langle \operatorname{cf}\right\rangle \right] = \frac{\left\langle \operatorname{cf}_{\operatorname{ss}}\right\rangle}{\left\langle \operatorname{cf}\right\rangle},\tag{2.4}$$

where $\langle cf_{ss} \rangle$ indicates the average of five calibrations done with the sidescatter border and $\langle cf \rangle$ the same but with no sidescatter (just the ICP).

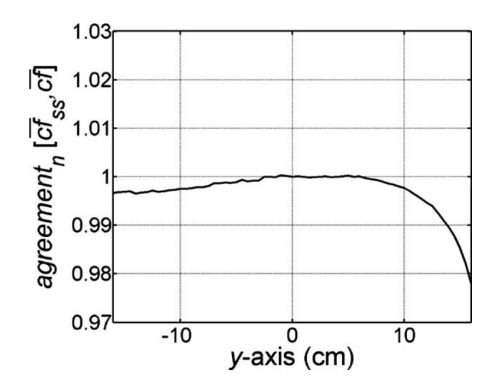


Figure 2–8: Effect on resulting calibration factors of using sidescatter during the calibration procedure [13].

Taking the average of several calibrations can help to mitigate the undesired effects that occur because of variations in the dose distribution used and variations in array positioning. The results are shown in figure 2–8. As seen on the figure, the response is asymmetric: the detectors at the

negative end of the Y-axis responded down to -0.35 %, while to at the positive end went down to -2.21 %. This indicates that even with the addition of the sidescatter border around the ICP, the third postulate was not respected [13].

The authors state that the benefit of using sidescatter is not entirely clear, but that it provided the most reproducible calibrations and that it improved the agreement of shallow profiles with a SWT system. However, use of sidescatter worsened agreement for a 10 cm water-equivalent depth measurement [13].

Finally, Simon et al. conclude that:

- The array has a minimal calibration response to additional buildup being used during calibration (< 0.8 % for the 0.9 cm to 4.9 cm range of buildup values, including the inherent buildup). They cite their previous article [15] regarding this. Even while stating this, they recommend calibrating the array with a buildup that meets of exceed the energy-specific depth of dose maximum [13]. They do not elaborate on this recommendation and it is unclear exactly what advantages there are to performing calibration with additional buildup.
- The array has a slight response to change in energy (< 1.5 % for x-rays, 18 MV to 6 MV). Thus, they recommend using energy-specific calibrations [13].
- By taking all the steps to minimize postulate violations (continuous beam on, additional sidescatter, leaving the ICP connected to its power supply beforehand), they state that the overall error in calibration factors was reduced from ±1.6 % to ±0.48 % [13]. Leaving the ICP connected and storing it in its measurement environment is easy enough, but the linear translation stage required for changing the ICP position remotely while the radiation beam is kept on is surely not available to every commercial user of the device. Furthermore, the sidescatter border, although not impossible to obtain, requires custom machining to be made. Therefore it may not be easy to implement all these measures for ordinary users of the IC PROFILERTM.

2.3 Background Information

This section introduces extra background information that is useful to know to fully understand this project's method and results.

2.3.1 Beam Commissioning and Modeling for Collapsed-Cone Superposition-Convolution Dose Calculation

The AAPM's Task Group 106 report [10] is the main reference document used at this time in North America regarding beam commissioning. It provides several guidelines on the choice of phantom, methods, equipment setup and detectors as well as specifying photon-specific and electron-specific measurements and data processing. The beam data acquired in this process often serves as direct input into the chosen treatment planning system and should therefore be measured with the utmost care. TG-106 specifies that inter-observer variations in measured data should be of less than 1 %.

Beam commissioning data is obviously necessary for collapsed-cone superposition-convolution dose calculation algorithms, where radiation beams are modeled from a few parameters only (e.g. on the order of 30 parameters). These parameters must be carefully adjusted such that the predictions of the TPS agree with measurements as best as possible. This type of dose calculation algorithm for treatment planning is not the only one possible (one can think of numerical Monte Carlo [17, 18, 19] or analytical anisotropic algorithm [18] or analytical radiation transport approaches [20]). However, since in this project use was made of a collapsed-cone superposition-convolution algorithm exclusively, a discussion of their working principles is beyond the scope of this text.

In collapsed-cone superposition-convolution algorithms, for example as in the Pinnacle³ TPS [21] (Philips Medical Systems, Fitchburg, WI, USA) used in this work, dose is determined by way of modeling the incident energy fluence exiting the linac head, projecting this fluence through the patient and determining total energy released in matter (TERMA) in each voxel (i.e. volume element of the patient geometry, obtained from computed tomography data) using the attenuated energy fluence that results from the ray path traveled and the known mass attenuation coefficients and densities along this path. The resulting TERMA distribution is then convolved with a Monte

Carlo-calculated energy deposition kernel, which takes into account the energy deposited as resulting from photon interactions and the subsequent charged particles released in the vicinity of the interaction point. Dose for each voxel is determined for a whole plan by superposing the dose distributions obtained for each beam in the plan. While only a few parameters describe the model, the relative dose to a water phantom predicted by the TPS should agree within 1 % or less of the measured data on the beam central axis. The agreement can worsen to 2 % for off-axis profiles [22].

However, even in Monte Carlo-based treatment planning systems, where the parameters used relate rather to the linac construction, beam commissioning data are essential for validation of the obtained dose distributions.

Beam Data Collected During Commissioning

One can divide the necessary measurements in two categories: scanned data and point data. In general, scanned data includes percent depth dose (PDD) and profiles (i.e. off-axis ratios, OAR). A set of square or rectangular field sizes is chosen for these measurements. Profiles are, additionally, measured for a set of chosen depths in water. Furthermore, they are taken in at least two orientations: in the gun-target axis of the linac (inline) and in the direction perpendicular to that (crossline). If the accelerator supports wedges, either physical or dynamic, then profiles and PDDs must be measured in both configurations: open-field and wedged-field. For linacs equipped with a multi-leaf collimator (MLC), profiles and PDDs for MLC-defined fields should also be measured. Figures 2–9 and 2–10 show examples of a PDD measurement and a profile measurement and their corresponding geometries.

Point data can include, depending on the situation and the particle type (photon or electron beams): relative dose factor (RDF, also called output factor, OF or total scatter factor), tray factor, wedge factor, cone factor, cutout factor, surface dose. For electron beams, the virtual source position must also be determined.

The most relevant point measurement for this project is the relative dose factor. Its definition is the following:

$$RDF(A, h\nu) = \frac{M(A, h\nu)}{M(10 \times 10 \text{ cm}^2, h\nu)},$$
(2.5)

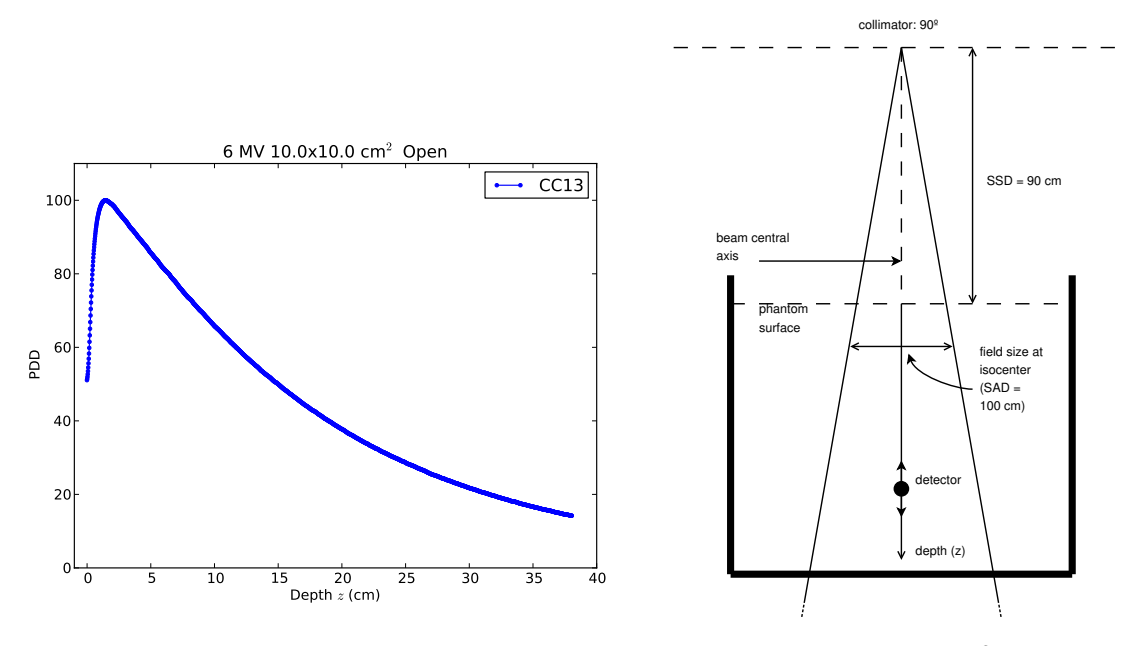


Figure 2–9: Example of a measured PDD for a 6 MV photon beam with a $10 \times 10 \text{ cm}^2$ field size at 90 cm source-to-surface distance. The measurement was conducted in water with a CC13 ionization chamber using a SWT system. The diagram on the right shows the measurement geometry. The curve is normalized to a value of 100 at the depth of maximum dose.

where A is a monicker for field size, $h\nu$ is nominal beam energy and M represents the result of a point measurement made at 10 cm depth in water on the beam central axis, with sufficient scattering material in all directions.

As can be expected from the above list of measurements, acquiring all beam data can take a significant amount of time. Furthermore, if an accelerator is capable of operating at different energies, the list of measurements must be repeated for each energy. TG-106 estimates the overall scanning speed at 2 seconds per point and at 60 points per scan [10]. For a machine with two energies and with 25 fields to be measured, their estimate yields a total scanning time of 20 hours, assuming 6 scans per field. This excludes time alloted for equipment setup and point measurements. In fact, TG-106 states that typically a full 1.5 weeks of measurement time will be required for two photon energies. Depending on the number of electron energies available, electron scan time will add 1 to 2 weeks to that. Verification of the data, analysis and report writing should then follow, adding another 2 to 3 weeks. Thus, in total, commissioning is expected to last from 4 to 6 weeks.

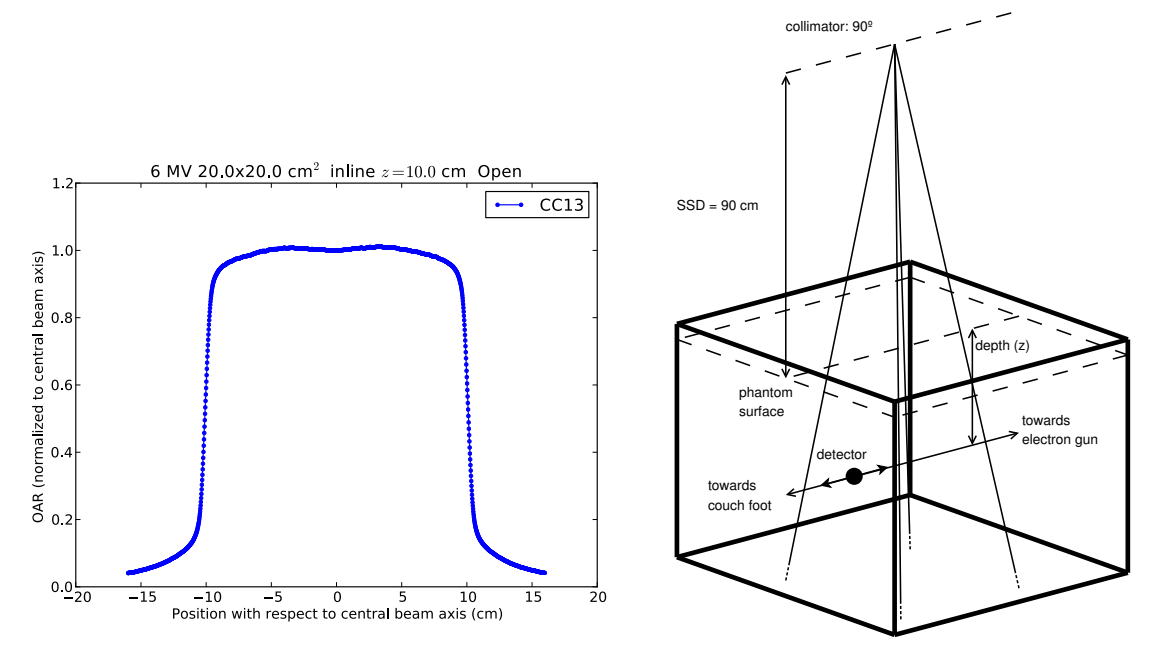


Figure 2–10: Example of an inline measured profile for a 6 MV photon beam with a $20 \times 20 \text{ cm}^2$ field size at 90 cm source-to-surface distance. The measurement was conducted in water with a CC13 ionization chamber using a SWT system. The measurement geometry is shown on the right. The curve is normalized to a value of 1.0 at the position of the beam central axis.

Materials Used in Beam Commissioning

According to TG-106, scan data should be acquired in water and point data can be acquired either in water or in a solid phantom. The scanning water tank should be large enough to allow scans of large fields (e.g. $40 \times 40 \text{ cm}^2$ at a source-to-surface distance of 100 cm) with sufficient scattering material on the sides (an extra 5 cm). In depth, some TPSs require scans to go up to 40 cm, others, up to 30 cm. Once again, sufficient material (5 cm) should be left for full scattering effects to be recorded.

Concerns have been raised by TG-106 [10] and others [23, 24] over the fact that solid phantoms are not truly dosimetrically equivalent to water and that corrections may be needed in order to use measurements made with them. Such solid phantoms include commercially available products such as Plastic Water® (CIRS, Norfolk, VA, USA), Virtual Water® (CIVCO Medical Solutions,

Kalona, IA, USA) and Solid Water® (Gammex, Middleton, WI, USA). With appropriate corrections and usage, some of these could be used for relative dosimetry and even for reference absolute dosimetry [25, 26]. In the very least, it has been shown that, without applying any corrections and according to Monte Carlo simulations, scan data such as profiles and PDDs are reproducible in a solid phantom within 0.5 % of a water phantom [27]. Furthermore, point data (RDF and WF) were within 1 % of that measured in water for a variety of field sizes and photon energies. The authors do mention, however, that absolute dose measurements sometimes deviated up to 1.5 % from that which was measured in water and that corrections need to be applied for absolute dosimetry [27].

The choice of detector used in commissioning depends on the situation. Ionization chambers have been used for this purpose for a long time, but their commonly large volume of detection (e.g. 0.5 cm³), relative to other detectors, put them at a disadvantage for measuring profiles of small fields or point data. Smaller volume ionization chambers (e.g. of 0.1 cm³ to 0.2 cm³) are preferred for these measurements. However, these chambers display lower signal-to-noise ratio than large chambers [7]. Note that the majority of ionization chambers available on the market and used in radio-oncology clinics are vented, i.e. the ionization signal is collected in the medium of air. They exhibit the characteristics discussed previously. There are, however, liquid-filled chambers that produce a higher ionization signal for a given chamber volume than vented chambers. These can represent a good choice when a small detector volume is desired while keeping high signal-to-noise ratio.

Silicon diodes are more sensitive and of smaller volume and make a good choice when performing measurements on small fields. Furthermore, the fact that silicon's stopping power ratio to water is constant over a wide range of energies relevant in radiotherapy makes these diodes attractive for electron beam dosimetry [7, 10]. Diodes, however, do have some disadvantages over ionization chambers in that they can display angular dependence on beam incidence, dose rate dependence and energy dependence [7, 28]. This latter dependence is problematic in large fields where a significant proportion of the dose originates from scattered low energy photons. As silicon's photoelectric effect cross-section is higher than water's for these energies, we say diodes over-respond (when we compare with dose measured with an ionization chamber in water under the same conditions).

For this reason, diodes are usually fitted with a high atomic number material acting as a shield against scattered low-energy photons to bring the response down to what can be expected from an ionization chamber [29]. One must keep in mind this solution is not ideal and will work mostly for a specific field size at a certain depth while introducing potentially unwanted perturbations to the spectrum [29]. Thus, diodes are not necessarily the best choice for every measurement needed in beam commissioning. Comparisons between diodes and ionization chambers should always be made before committing to the use of one or the other [10]. A note is simply made here that, in a lesser extent, other detectors can be used in commissioning, such as diamond detectors, films, radiochromic gels and thermoluminescent detectors.

Detector arrays represent the best method available for profile measurements of dynamically wedged fields during commissioning [10]. These types of wedge filters do not employ a static triangular filter placed in the beam path. Rather, the jaws of the secondary collimator move while the beam is active to produce an effect similar to that of a static wedge filter. Detector arrays make a good choice because of the dynamic nature of such fields which prohibits scanning. It is also possible to use Gafchromic film (Ashland Specialty Ingredients, Wilmington, DE, USA) for this purpose [30].

No particular difference has been noted between arrays of ionization chambers and arrays of diodes in the measurement of these fields; either one may be used [10]. Because the detectors in the array may not have the same relative sensitivity, these arrays must be calibrated so that the gain applied to each detectors (or corrections applied to measurements) makes their response uniform [10].

2.3.2 Analytical Modeling of Percent Depth Dose

While traditionally the percent depth dose values used in treatment planning originate from experimental measurements only (be it directly or through a beam modeling process), there has been work devoted to finding analytic representations of PDD curves in the form of empirical or semi-empirical models. Such models were designed with many purposes in mind: as a faster way to determine PDD [31], as an alternative to depth dose data look-up tables [32] and as a way to characterize beam quality [33, 34, 35].

All of these models require some measured data to be used to fit model parameters. Only one tissue-phantom ratio (TPR) value is required to be measured for the model presented by Gerbi *et al.* [31]. But this model is unable to represent PDD in the buildup region, as is the case for the model proposed by Bjarngard *et al.* [34].

The function presented by Wang et al. [35] assumes either PDD and scatter factor (SF) or TPR and SF have been measured, but is able to fit in all regions of the depth-dose curve (the reader is referred to reference [7] for the definitions of SF and TPR). The authors mention that they expect that this model can be used to reconstruct depth-dose data in situations where measurements at all desired depths or field sizes are not available.

The analytical representation of depth-dose data proposed by Wierzbicki *et al.* [32] assumes simply that all depth-dose data have been measured. The representation, a fitting function in the form of

$$PDD(z,r) = A(r)e^{-\alpha(r)z} - B(r)e^{-\beta(r)z}, \qquad (2.6)$$

where z is the depth in water and r the circular field radius, is focused on modeling depth-dose curves of radiosurgical fields. A, α , B and β are the fit parameters, which vary according to field size and accelerator. The proposed goal of this analytical representation was to facilitate lookup of PDD values by using a function rather than a large lookup-table, which was very memory-consuming for treatment planning systems at the time. The authors state that they believe a minimum of three exponentials are required for a valid approximation of standard radiotherapy fields, because of the increase in the scatter component when compared to the smaller radiosurgical fields.

2.3.3 Dose Distribution Comparison Tools

There has long been a desire for a dose-comparison tool to evaluate to which degree two measured dose distributions agree together (call them the evaluated distribution and the reference distribution). The initially used tools were dose-difference (DD) and distance-to-agreement (DTA).

The first is defined as taking simply the difference between the two dose distributions. This yields a metric that almost inevitably fails in high dose-gradient regions: only a slight spatial mismatch between the two distributions can cause an elevated dose-difference. Often this dose-difference is expressed as a percentage relative to some dose of reference.

Conversely, DTA is not sensitive to low dose-gradient regions, since it is defined as the distance to the closest point in agreement in the reference distribution from the position of the point tested in the evaluated distribution. With a low dose-gradient, the point in close agreement may be quite far spatially.

These two metrics are best suited for mutually-exclusive dose gradient regions and therefore there was effort devoted to finding a tool that could be used under any dose-gradient conditions. One of these tools is the now widely-adopted Gamma dose comparison tool [36, 37]. It is defined as

$$\gamma = \min_{\mathbf{r}_e} \sqrt{\frac{|\mathbf{r}_e - \mathbf{r}_r|^2}{\Delta d^2} + \frac{[D_e(\mathbf{r}_e) - D_r(\mathbf{r}_r)]^2}{\Delta D^2}},$$
(2.7)

where \mathbf{r}_e are evaluated dose distribution points, \mathbf{r}_r are reference dose distribution points, $D_e(\mathbf{r}_e)$ and $D_r(\mathbf{r}_r)$ the dose at evaluated and reference distribution points respectively. Δd represent a distance tolerance criterion while ΔD is a dose tolerance criterion. In practice, ΔD is often chosen to be a percentage of the global maximum of a dose distribution. Δd is usually taken to be on the order of a millimeter.

Since the dose-distance space is normalized by the dose and spatial tolerances and the Euclidian distance calculated, regions of acceptable agreement are indicated by the regions consisting of reference dose distribution points where $\gamma < 1$. As indicated by the min operator in the above formula, the Gamma tool requires an exhaustive search over the evaluated dose distribution points (although some implementations of the Gamma metric calculation can be much more efficient compared to simple exhaustive search [37, 38, 39]).

This concludes the background chapter of this thesis. The next chapter will discuss the materials and the method used.

Chapter 3 Materials and Method

This chapter introduces the materials used in this project, as well as describes the methods applied.

3.1 Materials

This section describes, aside from the IC PROFILERTM, what were the materials used for this project.

3.1.1 Plastic Used

The solid phantom used on top of the ICP is constituted of Virtual Water® M1648 (CIVCO Medical Solutions, Kalona, IA, USA) plates of area 35.3×35.3 cm², fitting entirely over the surface of the ICP. Various thicknesses were available: 0.2 cm, 0.3 cm, 0.5 cm, 1.0 cm, 2.0 cm and 5.0 cm. Additionally, 30×30 cm² slabs of Plastic Water® were used to provide sidescattering material for the cavities near the end of the ICP's Y-axis.

Under the ICP were placed two plates of PMMA, totaling 3.8 cm thickness. With the 2.3 cm-thick backscatter layer included in the ICP below the cavities, they provide for a total thickness of 6.1 cm backscattering material.

3.1.2 Linear Accelerator

An Elekta Synergy® linear accelerator at Hôpital Maisonneuve-Rosemont's radio-oncology department in Montreal, Canada was used throughout this project. This machine is able to deliver three photon energies: 6 MV, 10 MV and 18 MV. In addition, several electron energies are available (however these were not used during this project). Wedged fields are produced with a physical 60°

wedge. The maximum field size is $40 \times 40 \text{ cm}^2$ with a 40 leaf-pairs multi-leaf collimator (MLC). Each leaf projects thus to a 1 cm width at the isocenter.

Even if this accelerator is able to produce a 10 MV beam, it was decided that only the 6 MV and 18 MV beams would be acquired for this project. These beam energies are the most frequently used in practice. Furthermore, investigating beam data acquisition with the IC PROFILERTM at these energies should be sufficient to show if the method has potential to work for a 10 MV beam as well.

3.1.3 Software

IC PROFILER TM Software

The IC PROFILERTM software (version 3.0.1.3) was used to drive the ICP. It was and remains today the only option available to configure ICP parameters and start/stop data acquisition. As such, this project had to work within the limitations of the IC PROFILERTM software. There was discussion with Sun Nuclear corporation staff about the limitations and inconveniences associated with the use of this software in the context of beam acquisition. They provided help and guidance regarding the software's functions and behavior, but could not provide source code or make custom modifications that would allow a more practical implementation of a lengthy beam data acquisition process. For this reason, a great effort was put into finding and developing workarounds that would make beam data acquisition time-efficient even when constrained to work with the IC PROFILERTM software.

This software, when the ICP is used in pulsed acquisition mode, detects beam on and automatically starts acquiring a profile. When the beam goes off, it automatically stops data acquisition, but the user still has to interact with the software to save the file and fill in the file header (with information such as field size, buildup, energy, collimator angle and so on). A screenshot of the IC PROFILERTM software is shown on figure 3–1. Some of the necessary mouse-clicks needed to save each measurement are highlighted. Note that these mouse-clicks are, strictly-speaking, not necessary to save a file. However, in the context of beam data acquisition leading to beam modeling, one must be sure to know under which conditions each measurement is made (field size, depth, energy,

and so on). Thus, this information must be entered manually for each file saved using the ICP software.

Due to the amount of profiles required to be measured during linac beam commissioning, the act of manually saving each file separately represents an unacceptable overhead in time spent not taking measurements. The necessary workarounds developed to overcome this IC PROFILERTM software limitation will be discussed in the next section of this text.

Python

The Python programming language (version 2.7) [40] was used extensively to prepare programs that would enable data acquisition with the ICP, reading the ICP software file format (.prm) and process the data contained in the files created by the ICP software. Some 6400 lines of code were written for the final versions of the programs used, excluding earlier versions and early tests.

This language was also used, mainly by Patrice Munger, Ph.D. at Hôpital Maisonneuve-Rosemont (HMR), to develop in-house software. As such, Python represented a good choice for interoperability between software developed for this project and existing in-house software. Such in-house software was used for three purposes. A DICOM read/write library was used to create and send through the hospital network step-and-shoot sequences of the fields to be measured to the record-and-verify system (MOSAIQ®, Elekta AB, Stockholm, Sweden) which could interface with the linac to deliver the fields. Another program was used to read .rfb (Omni-Pro Accept format, IBA Dosimetry GmbH, Schwarzenbruck, Germany) files for the purpose of reading reference SWT data.

Lastly, a profile and PDD analysis program allowing gamma metric comparisons between reference data and test data was used to compare different data sets (comparing either ICP to SWT measurements or beam model to measurements or beam model). This last program was written by P. Munger but was modified by the author to provide analysis with a percent difference metric as well. The comparison metrics will be defined in more details in a later section of this chapter. The program was also modified so more global statistics about the agreement between the two datasets could be extracted.

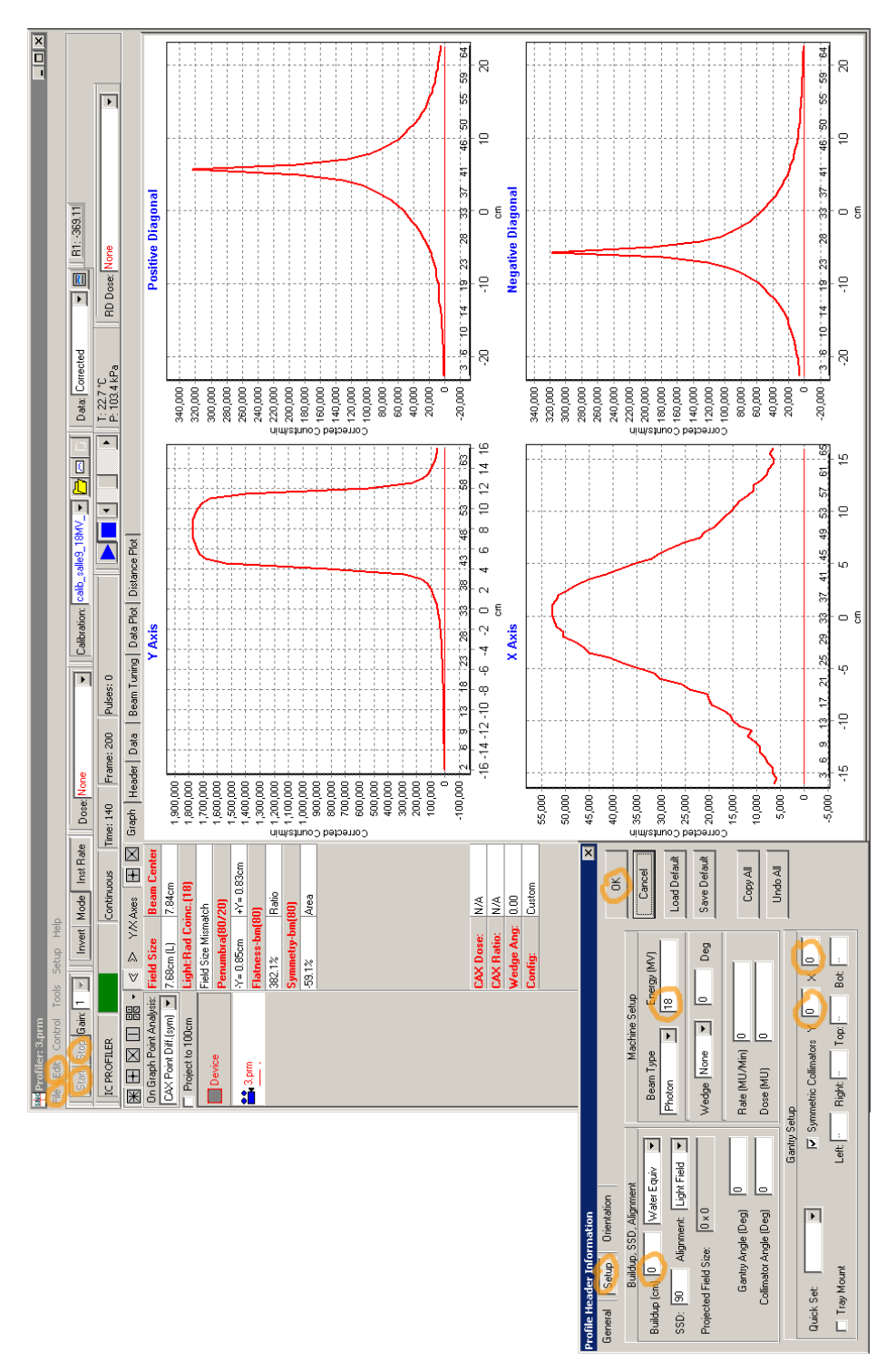


Figure 3–1: Screenshot of the IC PROFILERTM's software.

3.2 Method

3.2.1 Beam Acquisition

Measurement Setup

The measurement setup was chosen to best reproduce measurement conditions used for beam data acquisition with the SWT. At HMR, a source-surface distance (SSD) of 90 cm is used with a $61 \times 63.5 \times 54$ cm³ SWT (Blue Phantom, IBA Dosimetry GmbH, Schwarzenbruck, Germany). (Our treatment planning systems requires either 90 cm or 100 cm SSD measurements.) These dimensions are too large to replicate using a solid water-equivalent phantom. Instead, the 35.3×35.3 cm² area Virtual Water® slabs are used on top of the ICP, while the 30×30 cm² area Plastic Water® slabs are placed besides the ICP to provide sidescatter.

Only the ICP's "Y" axis is used to acquire beam data, meaning that, in this setup, every detector is surrounded by at least 10 cm sidescatter (except a few detectors near the ICP's electronics panel, which are always placed far into the umbra of region of profiles). The Y-axis was chosen as it includes the most detectors (65) of any axis on the ICP. As mentioned previously, PMMA plates are placed under the ICP to provide at least 5 cm backscatter as well, which is a TG-106 recommendation [10]. Figure 3–2 shows photographs of the ICP in its measurement setup. The setup is placed on the SWT platform, which allows easy adjustment of SSD and leveling. Furthermore, it eliminates any sag that could occur were the setup placed on the patient couch.

Two of the main problems we face when using the IC PROFILERTM for beam data acquisition are its relatively low spatial sampling (one detector every 0.5 cm) and its limited active detection length (32 cm). Better spatial sampling is desired when measuring high dose gradient regions (penumbrae of all fields generally, and small fields, $5 \times 5 \text{ cm}^2$ and below, specifically). A larger detection area is required to measure profiles of very large fields, e.g. $30 \times 30 \text{ cm}^2$ or $40 \times 40 \text{ cm}^2$, particularly at great depths because of beam divergence. These problems lead us to consider a very specific experimental setup as a solution, described here.

Figure 3–3 schematizes the measurement setup and demonstrates the order of the measurements. At each step, the total thickness of water-equivalent slabs on top of the ICP is reduced to provide the desired depth (starting with the thickest buildup initially). The ICP is raised to

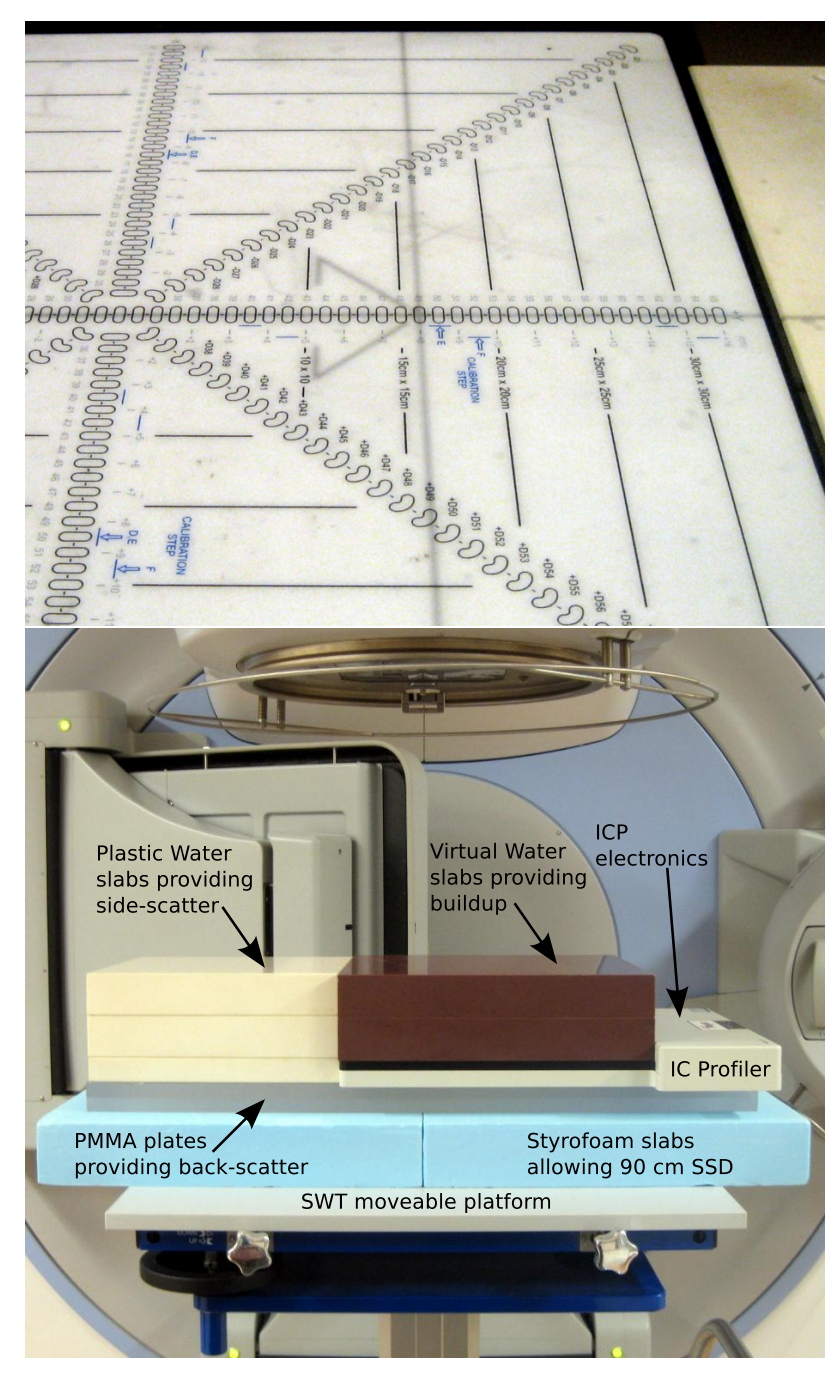


Figure 3–2: **(Top)** Photograph showing a typical centering of the ICP on the +8 cm detector. **(Bottom)** Photograph showing a possible measurement setup.

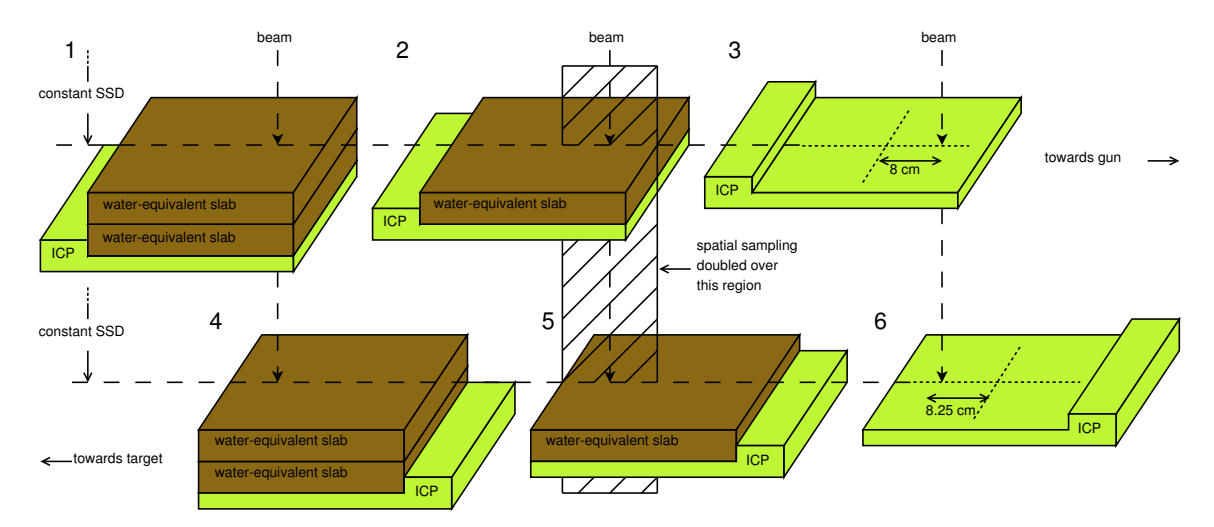


Figure 3–3: Schematic diagram of the measurement setup. The numbers indicates the order of the measurements.

maintain a constant SSD at 90 cm. In one phase of the measurements (top row of the diagram), the ICP is centered on the Y axis' +8 cm detector. When all depths have been measured for this orientation, the ICP is rotated 180° and centered between two detectors using the linac reticule, at +8.25 cm from the array center. Once all measurements are taken, two measurements are combined to yield a full profile.

For instance, in this example, measurements 1 and 4, 2 and 5, 3 and 6 are combined together, respectively. This method produces a spatial sampling double that of the ICP (used in its standard setup) over the region where both orientations share a common portion of the beam profile. Furthermore, it allows the measurement of profiles, with a good portion of the umbra, that would normally be too large to fit over the ICP active detection length. 8 cm was chosen as the central detector as it provides a good compromise between the area of overlap between the two combined measurements and the total available active length for measuring large fields. The 180° rotation is necessary to keep the ICP's electronics panel out of the primary radiation beam. Not shown on the diagram is the column of water-equivalent slabs placed at the end of the ICP's Y axis to provide sidescatter and the PMMA plates placed under the ICP to provide backscatter.

Note that larger spatial sampling for profiles could be achieved by increasing SSD beyond 90 cm, and then scaling back numerically to 90 cm SSD. However, we would no longer be able to measure large field profiles without irradiating the ICP electronics. Similarly, a reduced SSD, inferior to 90 cm, would make measuring large field profiles easier, but would reduce spatial sampling.

Profiles measured at different depths provide data necessary to assemble PDD curves by using the signal of the detector placed in the beam central axis. Other approaches were considered to acquire PDDs. One approach was to place a water-equivalent wedge on the surface of the ICP to vary depth along the detector axis, correcting for the known variation in profile shape. However, since so many different field sizes must be measured, and many of them quite small, this solution would work for a very limited number of fields at best. Moreover, corrections would need to be applied because of variations in SSD along the wedge, and depth dose would not be strictly measured under the central beam axis.

Another approach was to measure PDDs by irradiating the ICP on its side, with its X axis placed vertically along the beam central axis. However, since the ICP was not designed for this, doing so without irradiating the ICP electronics for large fields $(30 \times 30 \text{ cm}^2 \text{ or larger})$ would be difficult to achieve. Furthermore, after a trial, it was revealed that there are too many measurement artifacts due to the components in the ICP's construction to even consider this technique for small fields.

A Short Note on Acquiring TPR instead of PDD

Acquiring tissue-phantom ratios instead of percent depth dose would dispense with the need for repositioning vertically the ICP to maintain a constant source-to-surface distance of 90 cm. To change the depth of the measurement, the user would simply have modify the buildup thickness over the ICP panel. This would be very convenient, and TPR could be converted to PDD at a later time [28].

However, measuring TPR presents a serious disadvantage in the context of beam acquisition for input into the Pinnacle³ TPS: it requires as input profiles measured at several depths but at a constant SSD (either 90 cm or 100 cm [41]). If the TPR approach were used, either some beam divergence correction would have to be applied to measured profiles or a different series of

measurements would have to be made at 90 cm SSD to measure profiles exclusively. A correction for beam divergence would imply a lower spatial sampling of profiles at depths larger than 10 cm (since the correction would increase the effective detector spacing of the ICP for these depths). A different series of measurements would make the complete beam acquisition process longer in time, which is undesirable.

As it stands, the experimental setup presented earlier allows the simultaneous acquisition of PDD and OAR data, with *a priori* no need for further numerical manipulation before importation into Pinnacle, except for the combination of two measurements. For this reason, PDD was preferred to TPR.

Data Acquisition

The method of data acquisition employed with the ICP is radically different from what is usually done with a SWT system. When using a SWT, one would normally choose one beam geometry and vary the detector position while the radiation beam is active, making instantaneous measurements to obtain OARs and PDDs. The detector position is varied with the SWT hardware and a software program which allows the definitions of the desired detector positions prior to the measurements. The beam geometry is manually set by the user and the beam started before the detector position is varied automatically by the SWT system.

With the ICP and its software, this approach is not feasible. Rather, we choose to keep the detector position fixed as often as possible and vary beam geometry automatically during the measurements. User interaction is only required for changing the ICP panel's position, which is necessary to acquire PDDs in the least. The complete process is optimized to minimize the number of times the user has to manually reposition the ICP. No instantaneous measurements are made; each beam geometry is acquired by measuring the cumulative effect of a pre-defined amount of monitor units.

Before the start of acquisition, the list of the data needed to be acquired is carefully prepared. The sets of beam geometries, depths and energies to be measured are defined. The set of depths is split into two subsets. One defines "model depths"; that is, depths at which profiles are measured and used in the model construction. The second subset contains "PDD depths", depths at which

profiles are measured with the ICP with the sole purpose of obtaining the central detector signal to measure PDD.

The list of measurements in the order in which they should be taken is then created by running a Python script. The list specifies the position of the ICP for each measurement and what combination of beam geometry, energy and depth should be used for that measurement. The possible positions are: towards target centered at +8 cm, towards gun centered at +8.25 cm, 90° counter-clockwise from the gun centered at +8 cm and finally 90° clockwise from the gun centered at +8.25 cm. Only the position towards the gun and centered at +8 cm is considered for PDD depths, since only a point measurement is necessary at these depths (only the signal from the +8 cm detector on the ICP is taken from for these measurements).

The script prepares a step-and-shoot sequence corresponding to the exact planned order of the measurements. To each field is delivered 40 monitor units (MUs): more than long enough for the beam to stabilize and short enough to give an overall acquisition time that remains short. All fields delivered for a given combination of depth and ICP position are clustered together in the sequence. This minimizes the amount of time spent by the user to enter the linac room and change depth or ICP position.

Normally, each profile measured with the ICP must be saved separately in a single .prm file (this file extension designates the IC PROFILERTM software's native file format). This file's header data is entered manually by the user to identify beam geometry, energy and so on. The file is named and saved manually by mouse-clicking a "save" button. As mentioned before, this task, quite insignificant when done only once, becomes very burdensome when repeated over 1000 times over a few hours as is necessary in this case.

Since an ordered list of measurements has been clearly defined from the start, there is no need to manually edit the .prm file header data: beam geometries, depths, ICP positions, etc. are all exactly known for each measurement (as long as the measurements are made and saved in the pre-determined order). For this to work, the measurement files need to indicate by themselves where they stand in the list of measurements. The solution adopted was to have a program rename

each new file created in the working directory as 1.prm, 2.prm, 3.prm and so on, with the number indicating the position in the list. The measurement workflow is summarized in figure 3-4.

Furthermore, in order to avoid interrupting the step-and-shoot sequence and having to save over 1000 files manually, the ICP is left to acquire profile data continuously for all beam geometries measured for a single given combination of depth and ICP position. In other words, for a particular depth and ICP position, a single ICP .prm file contains measurements for all beam geometries. This reduces the number of files to be saved to less than 50, each containing a profile time series. All that is left then is to interpret each .prm file correctly to separate and extract the multiple beam profiles contained within. How this is accomplished is discussed in the coming text in section 3.2.2.

Pulsed Acquisition vs Continuous Acquisition and Measurement Reproducibility

Pulsed acquisition mode is recommended for use in pulsed beams because measurement updates, during which capacitors are discharged and charge measured, occur only in-between linac pulses. This means no measurement update will cause the ionization produced by a pulse to go unmeasured.

Trigger diodes embedded in the ICP and placed near each detector cavity are used to detect the linac pulses and start data acquisition upon beam on. However, it was quickly found that these diodes would not react for small fields and large depths at 6 MV, the signal being too low. Pulsed acquisition is simply not possible under these conditions with our ICP unit's hardware and firmware presets. Furthermore, there were some concerns about the reproducibility: the ICP's ability to always capture the same total ionization for a given field. Results regarding this will be discussed further in the next chapter. Reproducibility was tested by performing ten times the same irradiation and studying the recorded total corrected counts. The setup used was: 6 MV beam, 1.9 cm depth (including the inherent 0.9 cm buildup), 100 cm SSD, 90° collimator angle, 0° gantry angle and 15×15 cm² field size, with the ICP centered on the beam central axis. 100 MUs were delivered on each occasion for both measurement modes. 500 ms update time was used for continuous mode and 125 ms was used for pulsed mode.

The reader is reminded that always two measurements, taken with the ICP in two different orientations, are combined to give the final measured profiles. It is therefore important that the

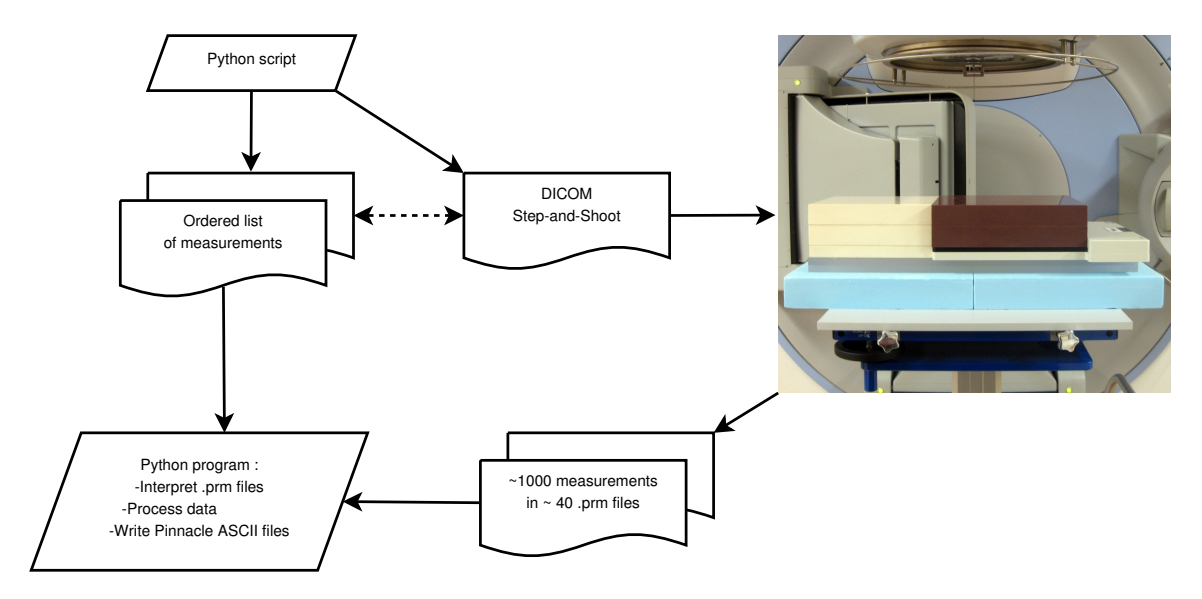


Figure 3–4: Schematic diagram of the workflow for performing beam data acquisition for a single beam energy with the ICP. The plain arrows indicate the flow of information during the beam acquisition process. The dashed double arrow indicates the correspondence between the planned list of measurements and the DICOM step-and-shoot sequence.

total corrected counts recorded be the same for the detectors that overlap in the two combined measurements. Furthermore, no reference detector is used with the ICP, only total counts recorded. This means that in PDD curves, where each point actually comes from a different ICP measurement, it is imperative that total ionization be recorded with as minimal a variability as possible.

For these reasons, continuous acquisition was used instead. In continuous acquisition, the interval between each measurement update is rather a fixed time interval and is adjustable with a minimum of 125 ms. A measurement update of 500 ms was chosen instead to help minimize the number of missed linac pulses, while still providing frequent-enough updates to allow the interpretation of the ICP data files and the extraction of the multiple beam profiles found inside. Note that this update time cannot be increased indefinitely because the ICP detector circuits would saturate, especially for shallow depths near the dose maximum where the signal is strong.

We may evaluate the impact of using continuous acquisition as follows. Say, for a given stable dose rate, that the total beam on time is t seconds. Now let T be the measurement update period. The ratio t/T gives the number of measurement updates that will occur during the beam on time.

This number also corresponds to the maximum number possible of missed linac pulses during the beam on time.

In typical linacs, the pulse repetition frequency (PRF) is on the order of 100 to 200 pulses per second [42], meaning there is a 5 ms to 10 ms time in-between pulses. The total number of pulses during beam on time is $PRF \times t$. It appears then that the maximum (worst-case scenario) fraction of missed linac pulses is

$$\frac{t/T}{\text{PRF} \times t} = \frac{1}{\text{PRF} \times T}.$$
(3.1)

This ratio is inversely proportional to both PRF and measurement update interval T. Selecting a higher T=500 ms than the minimum 125 ms allows us to decrease the probability of missing a linac pulse, as well as the maximum possible number of linac pulses missed. Since the PRF is equal to 200 Hz for the accelerator used in this project, the maximum worst-case fraction of missed pulses is $1/(200 \text{ Hz} \times 500 \text{ ms}) = 1 \text{ \%}$. Under the assumption of equal dose-per-pulse, which should hold once the linac beam has stabilized, this means at worst there will be an underestimation of ionization by 1 %. Again, this represents a worst-case scenario and an error of this magnitude does not occur for every measurement. After some trials, it was found that this error was more acceptable than the error introduced by using pulsed acquisition.

Because the 18 MV beam was acquired prior to reproducibility tests comparing the two acquisition modes, some measurements, at depths shallower than 20 cm, were acquired in pulsed mode. At 20 cm depths or more, the measurements were made in continuous mode. The signal-to-noise ratio of the ICP being sufficiently good, the gain on its readout amplifier was kept at 1 regardless of beam energy, field size or depth.

3.2.2 Processing of Acquired Beam Data

Interpretation of IC PROFILERTM Files

The .prm file format contains, for each detector on the ICP, the cumulative raw counts at each "timetic" value. Timetics indicate elapsed time since start of data acquisition in microseconds. At each timetic, a frame number is incremented, starting from zero at the start of acquisition. The

time-series capability is already included in the .prm file format to allow a replay (i.e. a movie) of the profile shape with time in the IC PROFILERTM software. Counts can be reduced to dimensions of charge and are directly related to the ionization measured in the ICP's detector cavities. Raw counts are corrected for background drift and multiplied by a correction factor which is determined by the ICP's calibration procedure. This yields the corrected counts, as introduced in chapter 2.

In our case, since the time-series of a .prm file contains the profile information of several beam geometries, it must be carefully analyzed. The 500 ms update time for continuous acquisition was chosen to be long enough not to miss too many pulses, yet short enough such that the sharp drops in ionization rate in-between the different irradiations are sampled enough to be detectable. It will typically take between 1 and 5 seconds for the MLC and collimator jaws to move into place from one beam geometry to the next, so an update time of 500 ms allows at least 2 to 3 updates in-between beams (a minimum of one update is needed while the beam is off, but 2 or 3 updates facilitate detection of this in the corrected counts time series).

The variation of total corrected counts with frame number for each detector in the ICP's Y axis is considered. More to the point, the numerical derivative of total corrected counts, i.e. corrected counts rate, is used. The goal is to identify where in time lie the transitions between the different beams in the corrected counts time-series. These transitions between different beam geometries are characterized by sharp drops in corrected counts rate when the radiation beam is turned off and the collimation is in the process of being modified, as is the case in any step-and-shoot sequence.

The low plateaus in corrected counts created in this way can be used to identify the different profiles contained in the cumulative corrected counts time series. The algorithm for detecting these separate beams is as follows. First, the square of the corrected counts (cc) rate from each detector is summed up:

$$\alpha(n) = \sum_{i=1}^{65} \left(\frac{\mathrm{dcc}_i}{\mathrm{d}n}\right)^2,\tag{3.2}$$

where i is an index running over the detector number in the ICP Y axis and n is frame number. Detectors in the umbra contribute very little to this sum, while any detector in a penumbra or in the field will contribute much more. At 6 MV, a fixed threshold of 15000 corrected counts squared per frame is then used to determine all contiguous regions of frame numbers below this values in $\alpha(n)$ (a threshold of 2 × 10⁷ is used for 18 MV). The center of those contiguous regions is taken to be the frame number corresponding to the transition between two fields (i.e. two separate irradiations).

The thresholds were chosen so they can be applied to measurements made at any depth or field size (open or wedged fields) for the given energy and dose rate. In practice, the lowest-signal field measured determines the threshold to use (i.e. the 3×3 cm² wedged field). An example of the results of this thresholding analysis for a .prm file is shown in figure 3–5.

The difference in corrected counts in-between two transitions corresponds to the total measured corrected counts for a field, and this, for all detectors along the Y axis. It is implicit that a transition exists at n = 0 and n = N, where N is the total number of frames in the .prm file.

Any error made in detecting the transition between two beam geometries will introduce errors in profiles and PDDs, as one geometry will have an overestimation of total corrected counts and the other neighboring geometry will see its total corrected counts underestimated. Note that by always using total corrected counts and a fixed amount of MUs per irradiation, one eliminates the need for a reference chamber as ionization rate is not used, only total ionization.

Combination of Profiles

As explained previously with figure 3–3, measurements from two opposing ICP orientations are combined to yield a full profile. Let those measurements be called half-profiles (even though they overlap over a region of the beam and actually measure more than half a profile each). In theory, these two half-profiles are shifted apart along the detector array axis by exactly 0.25 cm, half the detector spacing on the array. One then needs to flip one of the two half-profiles (vertical reflection along an axis passing by the 0 cm position), translate it 0.25 cm and then interlace the result with the other half-profile to produce the full profile.

However, because the ICP is positioned manually, and scanning (i.e. changing repeatedly its position remotely by some increment) it is not possible with our equipment, it is difficult to ensure the position of the beam center is exactly as wanted. If one could scan the ICP, one would be able to go "maximum hunting" and ensure that it is really centered on the beam central axis (or

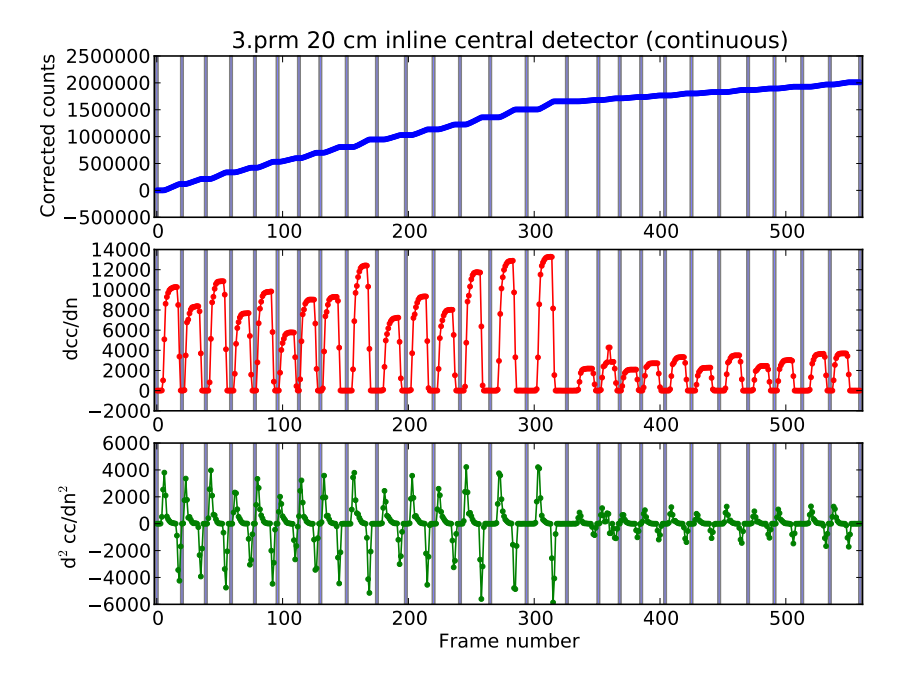


Figure 3–5: Example of the automatically detected transitions, indicated by vertical bars, for the beam central axis detector only in a 6 MV beam at 20 cm depth. The cumulative corrected counts are plotted on the top graph, while for reference the first and second derivatives are shown in the graphs below. All fields placed shortly after frame number 320 are wedged fields, which is why the height of the peaks in corrected counts rate is lower than in the first portion of the file since the delivered dose rate is lower.

command a shift of 0.25 cm from the beam central axis). Therefore, rather than assume a fixed 0.25 cm shift between the two half-profiles, the position of the beam center along the ICP's Y axis is determined using every field size available that fits over the ICP active length. Because the ICP is centered using the +8 cm detector under the beam central axis, and not the central chamber, this occurs only for fields smaller than 12×12 cm². Once it is calculated from corrected counts, their dosimetric center is determined and saved in memory. (The 1×1 cm² field center is not used, as it is doubtful that its calculated center is meaningful considering the ICP's detector spacing and detector size.) The centers determined for each field size below 12×12 cm² are then averaged to estimate the beam center position along the ICP's Y axis.

The center is determined by considering the position of 50 % profile height on each side of the profile (using linear interpolation), with 100 % being defined for the +8 cm detector of the array, which should be quite close to the beam center. For the ICP position where a shift of 0.25 cm is applied, 100 % is defined as the average of two detector signals, on each side of the beam central axis. From the two respective beam center positions for the two orientations, the appropriate shift is determined and applied.

As a precaution, it was preferred to normalize profiles only after the two ICP measurements were combined, instead of normalizing each measurement separately and then combining them. Normalizing each half-profile prior to combination presents a risk of introducing wrong data into a beam model. Because of the different ICP orientations and positions in space used to acquire the two measurements, normalizing prior to combination could lead to a profile asymmetry problem going undetected, which is highly undesirable. It is preferable to verify, prior to combination and importation into the TPS, that two corresponding ICP measurements do indeed agree together in terms of absolute ionization collected. This made it necessary to have reproducible ICP measurements in terms of total corrected counts.

Profile Interpolation

The Pinnacle³ TPS (version 9.0) requires profiles to be interpolated every 0.2 cm. To avoid having to do this processing step manually in the TPS after importation of the beam data, the profiles are interpolated linearly before importation into Pinnacle.

Smoothing of Profiles

Smoothing of the profiles has proved necessary in over the profile central region. No smoothing is performed at the profile shoulders, penumbrae and in the umbra. The main reason for having to smooth the profiles is the fact that always two half-profiles are combined to yield a full profile and that there can be discrepancies in recorded total corrected counts for each half-profiles, as will be demonstrated in the next chapter. These differences produce visible high-frequency noise over the region shared by the two half-profiles.

To attenuate this noise, profiles are convoluted with a 5-point Hamming window equal to [0.08, 0.54, 1., 0.54, 0.08]. The choice of this window and window length were made empirically by

trying out different combinations of window length and type available in the NumPy Python library (part of the SciPy project) [43]. This was found to greatly reduce noise introduced by the half-profile combination procedure while not significantly changing the profile shape over regions where noise is not apparent.

Furthermore, since no smoothing is performed in the penumbrae or umbrae (only the relatively flat central region of a profile is smoothed), the consequences of the convolution are limited to attenuating the noise introduced by the combination procedure over a profile region shared by the two half-profiles. Because the situation is different for very small field sizes, with no flat region in the profile, no smoothing is performed for 1×1 cm², 2×2 cm² and 3×3 cm² fields. Smoothing profiles (and PDDs) is a common procedure even when using SWT systems.

Percent Depth Dose Curve Fitting

The IC PROFILERTM has an inherent buildup equivalent to 0.9 cm of water [11]. This buildup, for obvious reasons, cannot be removed. Thus, any measurements at depths below 0.9 cm cannot be made with the ICP. This is problematic for measuring PDD data with the ICP. Furthermore, due to the fact that a solid phantom is used, PDD data cannot be obtained from scan data (one cannot scan the ICP in water). Rather, a series of point measurements along the beam axis must be made with the ICP and the solid phantom remaining stationary between each change in depth. To change the depth, the user has to enter the linac room and manually change the thickness of the solid phantom placed on top of the ICP.

If one were to try and perform these point measurements at every depth in a conventional scanned measurement, the time expended would be too great to justify the use of the ICP and its solid phantom versus the SWT. Therefore, the number of depths chosen for point measurements with the ICP must be limited within reason. Again, a problem arises in that the TPS, Pinnacle³, requires many more points in the PDD curve than can be taken in a reasonable amount of time. A fitting function able to tie all point measurements made with the ICP into a PDD curve that can be input into the TPS is proposed as a solution.

In reference [32], PDD curves were fitted for radiosurgical fields. The authors believed a three-exponential function should be able to fit PDD for conventional radiotherapy fields. Given this

insight, and that part of the PDD shape may be accounted for with the inverse square law, a fitting function of the type

$$PDD_{fit}(z) = \left(\frac{f}{f+z}\right)^2 \left(Ae^{az} + Be^{bz} + Ce^{cz}\right)$$
(3.3)

was chosen, with z being depth in water. f may be interpreted as the source-to-surface distance, and the rest of the variables are simply fit parameters.

The set of depths measured with the ICP was chosen, for a 6 MV beam, as such: 0.9 cm to 2.5 cm in 0.1 cm increments along with 3.0, 3.5, 4.0, 5.0, 10.0, 15.0, 20.0, 25.0 and 30.0 cm depths. This set of depths is modified for use with an 18 MV beam because of its deeper depth of maximum dose. The new set includes depths taken at 0.1 cm increments up to 3.0 cm, with the same depths thereafter.

A PDD value at the surface is then added to the ICP measurements to help fit within the buildup region. This surface PDD value was measured by using a Sun Nuclear Corp. EDGETM shielded diode detector embedded at the surface of a water-equivalent slab. The ratio between the signal at 5 cm depth in water-equivalent material and the signal from the diode with no buildup was measured (a depth of 5 cm was chosen because it represents a depth that could be easily obtained with a single water-equivalent slab and is beyond the depth of dose maximum). Since an ICP measurement is made at 5 cm, the same ratio is applied then to infer on the surface PDD value:

$$PDD_{ICP}(0 \text{ cm}) = \frac{M_{EDGE}(0 \text{ cm})}{M_{EDGE}(5 \text{ cm})} \times PDD_{ICP}(5 \text{ cm}). \tag{3.4}$$

A diode was chosen for its small detection volume, enabling it to measure the ratio for small fields such as those 3×3 cm² or lower. A large parallel-plate ionization chamber would have been inappropriate for these fields. The diode's location is 0.3 mm below the surface of the detector housing, which is smaller than the ≈ 1 mm effective point of measurement (EPOM) of typical parallel-plate chambers in a high-energy photon beam [44]. For PDD fitting purposes only, the 0.3 mm value was ignored and the detector's position was assumed to be at the surface of the phantom.

The end result is a surface PDD value able to guide the fitting function at the surface with the use of a constraint. It is apparent from the form of the fitting function that A + B + C actually gives surface PDD value, and the sum of these three parameters can be used as a constraint for the optimizer by forcing it to the desired value.

With the added point at the surface, a total of 25 different depths are used. Many more points are chosen in the buildup region and near the dose maximum than at great depth. This should be sufficient since after the depth of dose maximum, PDD is a slowly-varying function.

Before fitting point measurements made with the IC PROFILERTM, however, the fitting procedure was tested on SWT data. The reasoning behind this is that if the fitting function is able to reproduce the full PDD dataset using SWT data within a certain reasonable tolerance, then it should be able to do the same with the ICP-measured data. If it is not able to do this with the SWT data, then of course the fitting procedure cannot be trusted to work with the ICP data. Therefore, PDD points corresponding to the same set of available depths with the ICP were taken from SWT data and fitted using the procedure described above. 6 MV photon beam data were chosen to validate the fitting procedure because of its shallower z_{max} , when compared to an 18 MV beam. This represents the most difficult case to fit out of the two energies.

The fitting algorithm used is the following. An objective function is defined as the sum of squares of differences between the fitted function values and the measured values:

$$O(f, A, B, C, a, b, c, PDD_{\text{meas}}(\mathbf{z})) = \sum_{i} \left[PDD_{\text{fit}}(z_i) - PDD_{\text{meas}}(z_i)\right]^2,$$
(3.5)

where i is an index running over all depth values. While all measurements were taken at f = 90 cm and one could choose to force f to take on this value, it was found empirically that better fitting results could be obtained if f was left to vary as a fit parameter. $PDD_{meas}(\mathbf{z})$ represents the set of measured PDD values used as input for the fitting procedure. This objective function is minimized

under the following conditions:

$$\begin{aligned} & \underset{f,A,B,C,a,b,c}{\text{minimize:}} & O(f,A,B,C,a,b,c, \text{PDD}_{\text{meas}}(\mathbf{z})) \\ & \text{subject to:} & \text{PDD}_{\text{fit}}(0\text{ cm}) = A + B + C = \text{PDD}_{\text{meas}}(0\text{ cm}) \\ & \text{PDD}_{\text{fit}}(0.9\text{ cm}) = \text{PDD}_{\text{meas}}(0.9\text{ cm}) \\ & \text{PDD}_{\text{fit}}(5.0\text{ cm}) = \text{PDD}_{\text{meas}}(5.0\text{ cm}) \\ & \text{PDD}_{\text{fit}}(10.0\text{ cm}) = \text{PDD}_{\text{meas}}(10.0\text{ cm}) \\ & \text{PDD}_{\text{fit}}(30.0\text{ cm}) = \text{PDD}_{\text{meas}}(30.0\text{ cm}) \\ & \text{PDD}_{\text{fit}}(100.0\text{ cm}) > 0 \\ & \frac{\mathrm{d}}{\mathrm{d}z} \left. \text{PDD}_{\text{fit}}(z) \right|_{z=100.0\text{ cm}} < 0 \\ & \frac{\mathrm{d}^2}{\mathrm{d}z^2} \left. \text{PDD}_{\text{fit}}(z) \right|_{z=100.0\text{ cm}} > 0 \end{aligned}$$

The optimization routine used was the sequential least-squares algorithm implemented in the scientific computing toolset SciPy [43]. It is a gradient-based general-purpose minimization routine allowing equality and inequality constraints. It was found to give better results than the much-used unconstrained Levenburg-Marquardt algorithm for least-squares regression. A reason for this is that many more points are used at depths in the buildup region and near the dose maximum than elsewhere to fit the PDD curve. An unconstrained least-square algorithm with equal weights simply tries to minimize the sum of squares of differences, regardless of the spatial location of the point or the spatial sampling in the vicinity of that point.

A constrained minimization algorithm allows one to give infinite weights to certain points, making them "anchor-points" in the fit while providing a better chance for successful extrapolation past 30 cm depth with the use of inequality constraints. Indeed, the constraints used, shown above, were chosen with these purposes in mind.

The three inequality constraints ensure that the fitting function is able to extrapolate past 30 cm depth to approximately 40 cm depth. The first constraint forces the fitting function to have a strictly positive value at 100 cm. This is to ensure that, even at great depths, the fitting curve

does not go below zero. The two other inequalities reflect the behavior of a PDD curve past z_{max} . The curve should never reach below zero, but is always decreasing. Therefore, the rate at which the PDD decreases must become less and less with increasing depth. Indeed, it is well known that PDD decreases more rapidly near to the source rather than far away from the source (this is an inverse square law effect) [28]. These facts means the first derivative of the fitting function should remain negative, while its second derivative should remain positive.

Different initial values were used as an initial guess for the optimizer, depending on the situation. These values are summarized in table 3–1 and were taken from the optimizer results obtained for 10×10 cm² fields. The goal of using these custom initial guesses was to provide a reasonable set of parameters for the optimizer to work with from the start, making the optimization faster and possibly finding a better solution.

As explained above, the overall fitting procedure was tested with SWT data to verify that it could work as expected. During this validation study, the optimal parameters resulting from the fit were saved in a database for each beam. The final objective value using those parameters as an initial guess was compared to the final objective value obtained when using one of the initial guesses in table 3–1. The solution obtained with the lowest objective value was always retained. In other words, for every beam, two sets of parameters were used as initial guesses and the solution providing the better fit, in the sense that it most minimized the objective value, was kept.

These initial values assume the depth axis was expressed in centimeters while the PDD data is normalized to 100 at the depth of dose maximum and represent a reasonable starting guess. The routine was allowed to run up to 20000 iterations upon which, if convergence was not yet achieved,

Table 3–1: Initial parameters provided to the optimizer for the different beams for the analytical fit to PDD data.

Beam	f	A	a	В	b	С	С
6 MV Open	86.78	121.6	-0.03702	-15.95	-0.2287	-65.77	-3.062
6 MV Wedged	88.16	124.2	-0.03526	-17.87	-0.1760	-74.16	-2.923
18 MV Open	105.71	381.41	-0.03618	-264.76	-0.04191	-78.87	-1.061
18 MV Wedged	98.22	125.5	-0.02762	-7.028	-0.08674	-87.14,	-1.022

it was stopped and the fit results used as they were. The partial derivatives of the objective function in respect to each fit parameter were provided to the optimization routine. This is optional, as the algorithm can estimate these numerically, but providing them can improve convergence. On the other hand, the normals to the equality and inequality constraints were not provided and left for the algorithm to estimate.

3.2.3 Beam Modeling in Pinnacle TPS Version 9.0

Input Data Measured with the ICP

The input data acquired with the ICP and used as input for the beam model in Pinnacle³ TPS are the following: OARs taken at 2 cm, 5 cm, 10 cm, 20 cm and 30 cm depth for the following open field sizes: 1×1 cm², 2×2 cm², 3×3 cm², 4×4 cm², 5×5 cm², 7×7 cm², 5×20 cm², 20×5 cm², 10×10 cm², 12×12 cm², 15×15 cm², 20×20 cm², 25×25 cm², 30×30 cm² and 40×40 cm² and the following wedged fields: 3×3 cm², 4×4 cm², 5×5 cm², 7×7 cm², 10×10 cm², 12×12 cm², 15×15 cm², 20×20 cm², 25×25 cm², 30×30 cm² and 40×30 cm². The wedge is a 60-degrees physical filter.

In addition, OARs for the following MLC-defined fields were taken: $3 \times 3 \text{ cm}^2$, $6 \times 6 \text{ cm}^2$, $10 \times 10 \text{ cm}^2$, $14 \times 14 \text{ cm}^2$. The MLC-defined fields have the collimator jaws closed so that they project a $20 \times 20 \text{ cm}^2$ field size at the isocenter. The MLC leafs are further closed to define the desired field size. A 0.5 cm crossline shift is applied to the ICP in order not to perform measurements under an inter-leaf region. All measurements were made at SSD = 90 cm. The PDD was measured with the IC PROFILERTM for all the field configurations listed above.

All the profiles imported into Pinnacle were already sampled at 0.2 cm intervals. However, the profiles for field sizes $10 \times 10 \text{ cm}^2$ and below were re-sampled in Pinnacle to 0.1 cm using linear interpolation, as the procedure adopted at HMR specifies.

Input Data not Measured with the ICP

RDFs were also measured with the ICP. However, as will be presented and discussed in the next chapter, the results were not satisfactory. Therefore, the output factors measured at the time

of beam acquisition with the SWT were used as input for the ICP beam model in order to make dose distribution comparisons.

Other data taken at the time of acquisition and not measured with the ICP include all the linac's geometrical parameters (such as MLC leaf specifications and wedge physical profile and material) and the MLC inter-leaf leakage transmission (the "additional interleaf leakage transmission parameter" in Pinnacle³). These values were simply copied over from the clinical beam model.

Method Used for Model Construction

The method used for beam model construction was inspired from Starkschall et al. [22]. The reader is referred to this article and the Pinnacle³ Physics Reference Guide [41] for an explanation of the beam model and its various parameters. The different recommendations made in this article were respected in general. What differed in our modeling process is that a single beam model was made for all open field sizes, and another model was made for all wedged field sizes, whereas Starkschall et al. constructed several beam models for different field sizes (with Pinnacle³ interpolating beam models for intermediate field sizes).

A model covering all field sizes was chosen instead for the following reason. Interpolating beam models made for different square field sizes for computing irregular fields is questionable at best. Indeed, given a collimation for an irregular field which does not fall in-between two square field sizes, the choice of which pair of beam models to use for interpolation is unclear. A single beam model appropriately describing the incident fluence, source size, beam spectrum and so on for the machine in question can in principle be used to calculate beams of any geometry falling within the machine's capabilities without ambiguity. The disadvantage is that some compromises have to be made with regards to agreement of the model with measurements. When compromises had to be made, the model was tuned so that the best agreement was for the $10 \times 10 \text{ cm}^2$ field size and to a lesser extent smaller field sizes. Moreover, shallow depths (2 cm and 5 cm), being closer to the depth of maximum dose, were favored over larger depths.

3.2.4 Model Validation

A beam model must be validated by testing its dosimetric predictions against measurements for field configurations not used as input during its construction. At HMR, there is a given set of fields used for beam model validation. OAR, PDD and point measurements (absolute dose at 10 cm depth) are made to compare with model predictions.

Because many of these measurements must be made off the beam central axis and because the absolute dose measurement capability of the ICP has never been tested at our center, making these validation measurements with the ICP would be difficult and very time-consuming. Furthermore, it would mean validating a beam model using a detector in which we do not have complete confidence yet. The difficulties and limitations associated with the ICP lead us to choose to validate the ICP model with the measurements made with a SWT at the time of initial beam model validation for the linac in question.

The list of fields used for model validation is too long to be presented exhaustively here. It includes regular symmetrical square and rectangular fields with varying collimator or gantry angles. Also included are asymmetrical fields, i.e. fields where profiles and PDDs are acquired off the normally-used beam central axis. There are also many MLC-defined fields of arbitrary shape and center; these are termed here as irregular fields. Finally, there are blocked fields as well, where a cerrobend block is placed on a tray in the path of an open beam. All fields, when possible, are measured in open and wedged configurations. Some measurements are made at reduced or extended SSD, different than the 90 cm used at the time of beam acquisition.

The validation measurements made at the time of the original commissioning of the linac are used in the next chapter to evaluate how well the ICP beam model validates compared to the clinical SWT beam model validation results.

3.2.5 Beam Data and Model Comparisons

Firstly, ICP measurements are compared to SWT measurements for the same field configurations to see if they agree. Where they do not agree, this comparison serves to highlight any

differences with SWT measurements. Secondly, the ICP beam model is compared to ICP measurements to ensure they are in good agreement.

Thirdly, the clinical beam model is compared to ICP measurements. It is checked that the ICP beam model agrees better with the ICP measurements than the clinical model agrees with the ICP measurements. This is to ensure the ICP model is significantly more representative of the ICP data than the clinical model is.

Lastly, the ICP beam model is compared directly to the clinical beam model. By this, it is meant the calculated profiles and PDDs from each model are compared. Other comparisons made thereafter assess differences in calculated dose distributions or DVHs. These are ways to compare the two models to see how they fare with more complicated beam and phantom geometries, rather than simply comparing the computed profiles and PDDs from the beam models. How dose distributions are compared is discussed in the next subsection of this text.

Comparison Metrics and Statistics for Model and Acquisition Data Sets

Any comparisons made between measurements (either from the ICP or a SWT) and other measurements or beam model were made using in-house software developed by Patrice Munger at HMR. This software normalizes PDD curves at a value of 100 at 10 cm depth (strictly speaking, one should call these fractional depth dose (FDD) curves, since by definition PDD curves are normalized at the depth of dose maximum). Each profile is then normalized at its center at the value of the PDD at the corresponding profile depth, i.e., the profile at 10 cm depth will be normalized to 100 at the beam central axis.

Gamma comparisons are made with 2 %, 2 mm criteria. The 2 % dose criterion is 2 % of the PDD at 10 cm depth, i.e. 2 % of 100 = 2. This has the effect of giving relatively a larger tolerance for the deepest profiles, where the PDD is lower, than for the shallow profiles, where PDD is higher.

The software was modified to allow a direct percentage difference comparison point-by-point. This percentage difference is expected to be quite high in the penumbrae of profiles, where the dose gradient is large, if the measurements are not perfectly aligned or if the measured field size differs from the reference measurement. Therefore, percentage difference may be most useful for PDD comparisons outside the buildup region and for profile regions outside the penumbra.

The sheer number of profiles and PDDs compared makes it difficult to weigh in favor of a data set versus another when both are compared to a reference data set or simply to assess if a data set corresponds reasonably well to another. To make these tasks easier, some statistics are calculated for each pair of curves. Furthermore, each curve is separated into two regions. For PDDs, the two regions are the surface up to z_{max} and z_{max} to the deepest depth. For profiles, there is the central in-field region and the second region comprises the penumbrae and the umbrae.

For a given field size, statistics are calculated as follows. In each region, the maximum, mean and the percentage of passing points are calculated. This is done for the gamma metric and the percentage difference. The same is done for the overall curve, disregarding the defined regions. For the purpose of calculating percentage difference statistics, the tolerance is set to 2 % (of CAX value for OARs, and of value at 10 cm depth for PDD).

These statistics are reported in a PDF file report, displayed above a graph where the comparison can be seen visually. The various statistics for each pair of curves (i.e. all profiles and the PDD) are averaged together to give a general idea of how well the data set fits the reference. Furthermore, the distance over which the two data sets fail either the gamma comparison or the percentage difference comparison is summed over all pairs of curves and displayed at the top of the report along with the averaged statistics. An example of the PDF report is shown in figure 3–6, while the specific definitions of the metrics used for PDD and OAR comparisons in the next chapter are defined in table 3–2.

3.2.6 Comparison of Dose Distributions

Comparisons of dose distributions (that calculated by the ICP beam model vs the clinical beam model) are made in three possible fashions. Firstly, dose-volume histograms (DVHs) may be visually compared. 3D dose distributions may then be compared either by gamma analysis or simply by computing dose difference on a voxel-per-voxel basis.

All three comparison methods can be achieved conveniently by using the 3DVH® software (Sun Nuclear corporation, Melbourne, FL, USA) [45, 46]. The software allows easy adjustment

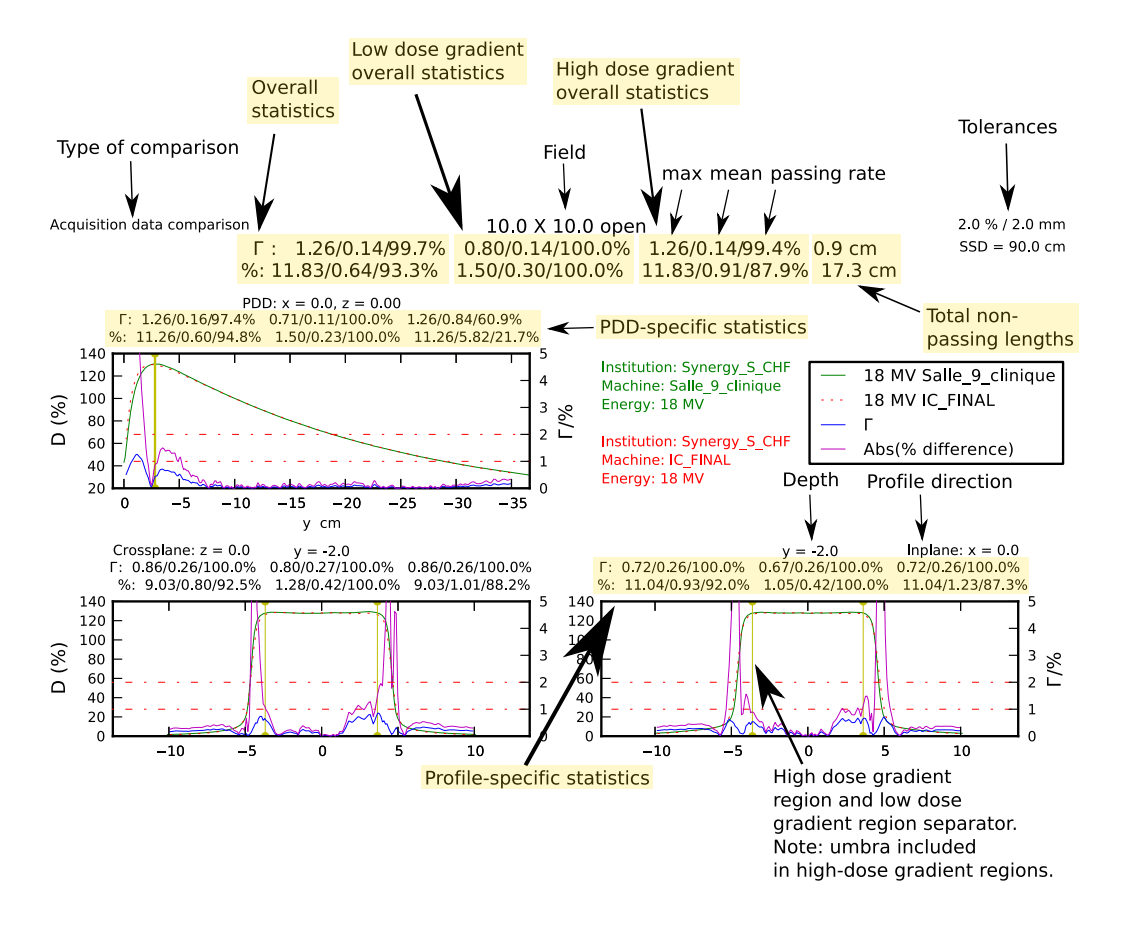


Figure 3–6: Example of the top portion of a PDF report of a comparison between two acquisition data sets.

of dose and distance-to-agreement criteria. Simple per voxel dose differences can be obtained by setting the dose and distance-to-agreement criteria to zero.

The criteria used for the gamma index comparisons of calculated dose distributions is 2 %, 3 mm. The dose criterion of 2 % refers to 2 % of the global maximum of the dose distribution. A spatial tolerance of 3 mm was chosen since the voxel size used for the dose grid in the Pinnacle TPS was set to $3 \times 3 \times 3$ mm³ for all evaluated plans. In some cases, the spatial tolerance was lowered to zero in order to observe differences between the two beam models more clearly.

This concludes the overview of the methods employed in this project. The next chapter reports on the results of the application of these methods.

Table 3–2: Metric definitions for PDD and OAR comparisons.

	•
Metric	Definition
Field size-specific $\overline{\gamma}$	Gamma values averaged over all points (all depths considered; lower is better)
Field size-specific $\gamma_{\rm rate}$	Percentage of points passing Gamma test (all points at all depths considered; higher is better)
Field size-specific $\overline{\%}$	Point-by-point percent differences averaged over all points (all depths considered; lower is better)
Field size-specific $\%_{\rm rate}$	Percentage of points passing the percentage difference test (all points at all depths considered; higher is better)
Overall $\overline{\gamma}$	Field size-specific $\overline{\gamma}$ values averaged over all field sizes (lower is better)
Overall $\gamma_{\rm rate}$	Field size-specific γ_{rate} values averaged over all field sizes (higher is better)
Overall $\overline{\%}$	Field size-specific $\overline{\%}$ values averaged over all field sizes (lower is better)
Overall $\%_{\text{rate}}$	Field size-specific $\%_{\rm rate}$ values averaged over all field sizes (higher is better)

Chapter 4 Results and Discussion

This chapter will present and discuss the results of this project.

4.1 IC PROFILERTM Total Corrected Counts Reproducibility

As hinted at previously in section 3.2.1, the ICP presented worse reproducibility in terms of total ionization (total corrected counts accumulated during beam on) in pulsed mode than in continuous mode. The results of 10 identical irradiations using the 6 MV beam are presented in table 4–1.

Of course, the results are influenced by the linac's variability as well. The measured reproducibility at the time of acceptation for the linac used in this project was of 0.1 % for the 6 MV beam (measured as standard deviation from the mean value, with a sample of 5, 100 MU irradiations). From table 4–1, we can conclude that the measurements made in continuous were much closer to what was measured at the time of acceptation than measurement made in pulsed acquisition mode. Since having a reproducible total counts reading was essential to PDD data (no reference detector was used), continuous mode was chosen.

Off-axis ratio acquisition in pulsed mode or continuous mode is equally reproducible when the data are normalized to the central detector. Between two measurements, the maximum observed variation of an in-field detector signal is about 0.3 % of the central detector value. Since total

Table 4–1: Central detector total corrected counts variation over ten identical irradiations as given by the ICP software. σ refers to an estimation of the sample standard deviation.

Mode	max	min	average	σ (counts)	σ (% of average)
Pulsed	259864.60	254528.69	258344.89	1606.44	0.62
Continuous	260732.03	259503.96	260301.80	460.31	0.18

corrected counts of a single detector (not normalized) are used in calculating RDFs and PDDs, it was preferred to use continuous mode for acquisition.

4.2 Processing of Beam Data

This section discusses the resulting effects of any processing done on the acquired ICP data.

4.2.1 IC PROFILERTM Calibration

6 MV Y-axis calibration factors of the ICP were measured with no additional buildup except that which is inherent to the ICP. The results are shown in figure 4–1. As can be seen from the graph, the calibration factors generally rise with distance from the array center, i.e. calibration factors are higher for detectors near the array ends. This is consistent with the fact that calibration factors compensate for differences in relative sensitivity among its detectors and detectors near the array ends are in a different situation when compared to the central detector in terms of scattering conditions.

Calibration conditions, with the array centered under the beam central axis, are very different from the measurement conditions as used in the method described earlier, where the beam central axis coincides with the detector placed 8 cm from the array center. Evidently the application of calibration factors measured under the standard conditions to measurement using our unconventional measurement setup creates problems in the overlap of the two measured profiles, as can be seen in figure 4–2.

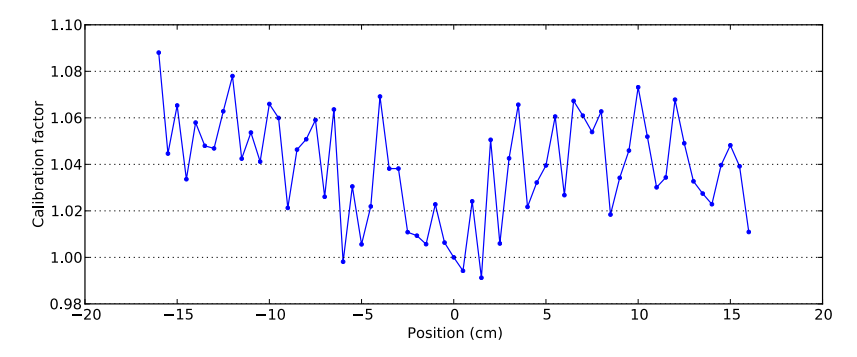


Figure 4-1: 6 MV calibration factors for the ICP Y-axis.

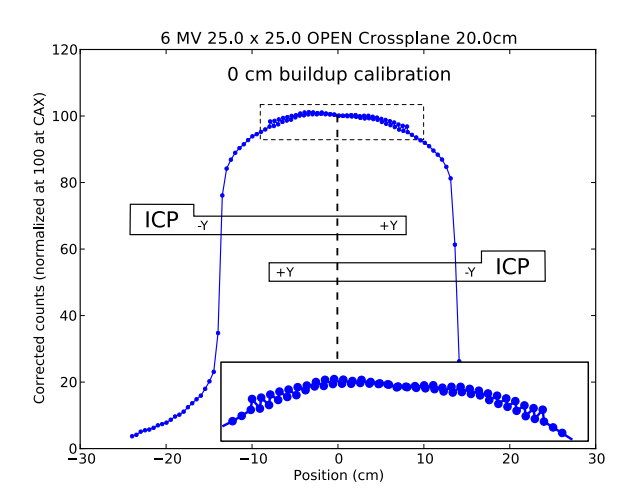


Figure 4–2: Effect of applying calibration with the combination of half-profiles. Drawings on the graph show the two ICP positions used to measure the half-profiles (not to scale). The +Y and -Y labels indicate the orientation of the ICP's Y-axis linear array of detectors.

Because calibration factors near array ends are higher than at the array center and an important sidescatter stack of water-equivalent slabs is used near the array's distal end, discrepancies appear near the positions along the array axis where the half-profiles start overlapping. Sidescatter is not normally used during the wide field array calibration, and thus it may be said that the calibration obtained by that procedure is not ideal for the experimental setup used in this project. Simon et al. [13] discussed the possibility of using sidescatter during calibration. This was attempted and the results are presented further in this chapter.

Unfortunately, it is not possible to measure calibration factors using the measurement setup defined in the previous chapter. The wide field calibration procedure itself assumes a detector array that is symmetric about a central detector. The fact that we use an off-center detector (the detector at +8 cm) as beam central axis detector prohibits the use of this procedure. Either a different calibration procedure is needed, or correction factors need to be applied to the half-profile combination procedure to compensate for this phenomenon. The solution adopted was to apply smoothing to combined profiles (results regarding this are presented later on in this chapter). Smoothing was also necessary for the 18 MV beam profiles.

Calibration Factors Measurement Reproducibility

The reader is reminded that Simon et al. [13] mention that calibration reproducibility is especially an issue on Elekta linacs due to small variations in beam symmetry from one irradiation to the next. Figure 4–3 shows the results obtained from ten separate array calibration procedures for the 6 MV beam. The figure compares the used calibration factors to the mean calibration factors obtained from those ten calibration procedures.

The spread of the different calibrations shown on the bottom is akin to what is demonstrated by Simon et al. in their article [13]. The spread is most pronounced for detectors at distal ends of the array, with calibration ranging from $\approx +5$ % to ≈ -4 % relative to the mean value. Therefore, it seems that a single calibration measurement should not be taken as being necessarily correct (at least when calibrating using an Elekta Synergy linac; the case may be different with other radiation sources). Rather, many calibrations should be performed, and their average taken. Alternatively, as done in this project, a calibration measurement close to the mean calibration is chosen for use, as shown in the center graph of figure 4–3. The highest deviation from the mean calibration factors are of less than 0.5 % for the detectors near +10 cm. Thus, this calibration measurement was accepted as being valid for the 6 MV beam.

For the 18 MV beam, the same measurements were performed. The results are presented in figure 4–4. Similarly to the 6 MV case, the different calibration exhibit a spread around their mean, though this time the spread is confined to a variation ranging from $\approx +1.5 \%$ to $\approx -2.5 \%$ at distal ends. The used calibration factors for the 18 MV beam differ by less than 0.5 % from the mean calibration factors obtained by the repeated measurements for all detectors of the array.

Of the Use of Sidescatter During Calibration

The calibration procedure was initially tried with and without 3 cm sidescatter water-equivalent slabs placed on every side of the ICP, except where its electronics box resides.

Figure 4–5 shows the results obtained for the 6 MV beam. The bottom graph shows the ratio of calibration factors obtained with sidescatter to those obtained without it. Because of the poor calibration factors reproducibility (from $\approx +5$ % to ≈ -4 % at distal ends of the array), we cannot conclude exactly on the influence of using sidescatter during calibration. However, we can guess

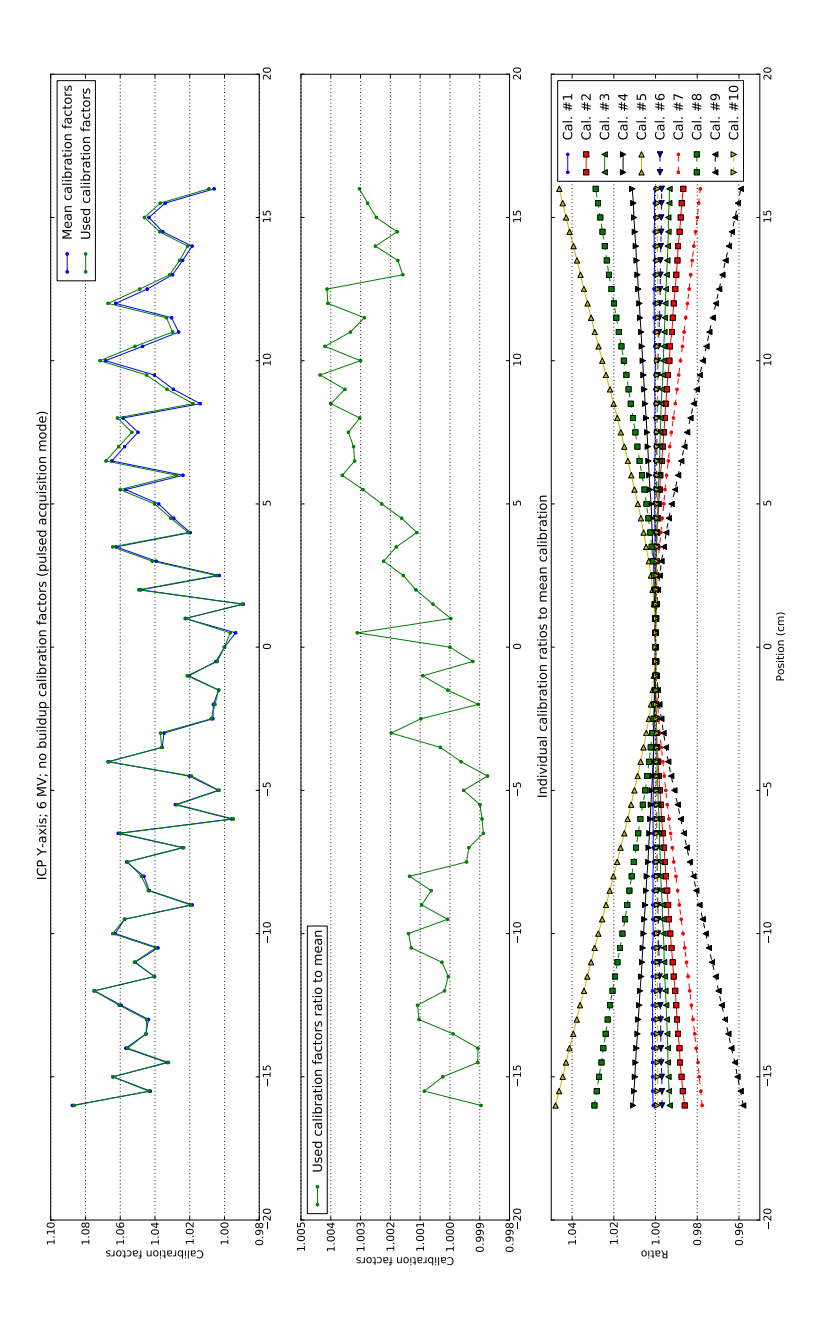


Figure 4-3: (Top) Used calibration factors and mean calibration factors. (Middle) Ratio of used calibration factors to mean calibration factors for the 6 MV beam. (Bottom) The ten separate sets of calibration factors normalized to the mean calibration factors.

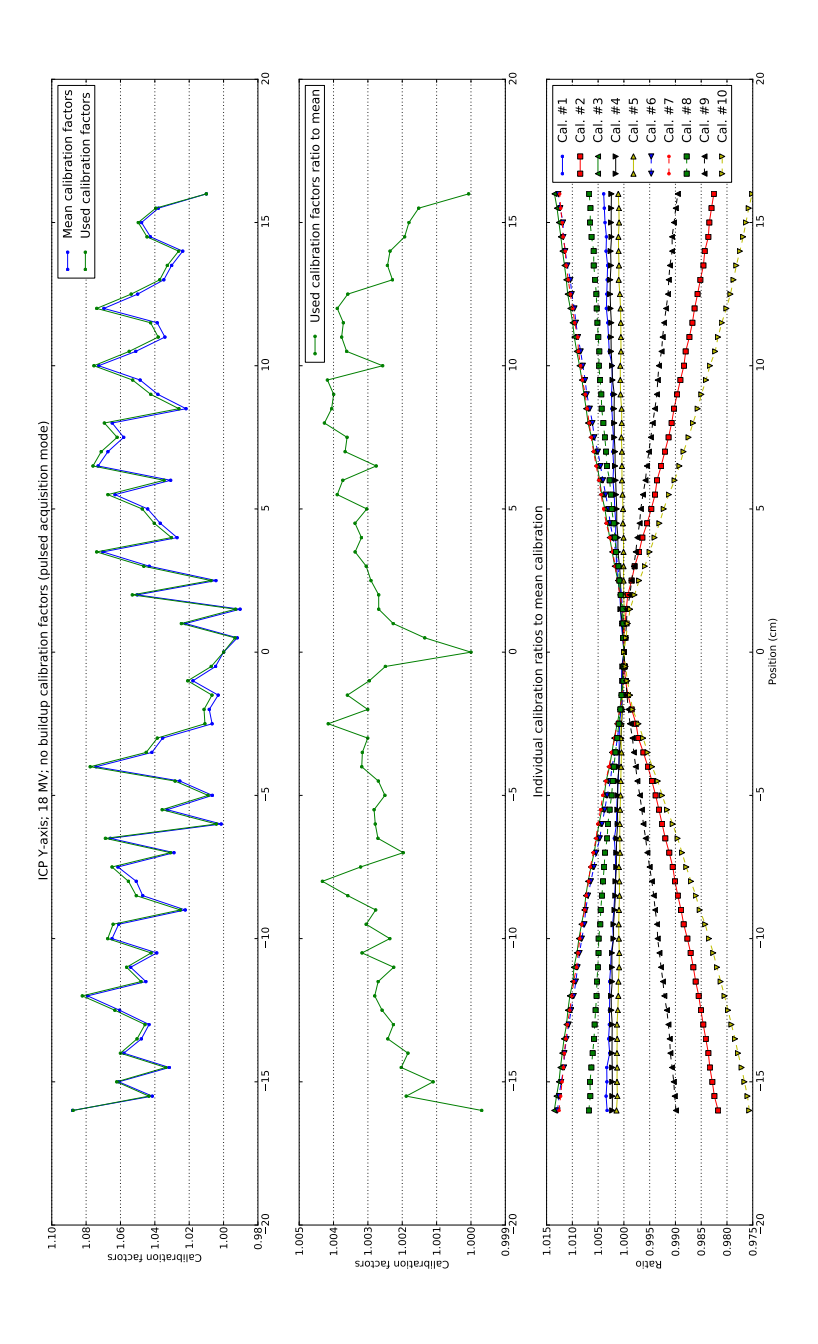


Figure 4–4: (**Top**) Used calibration factors and mean calibration factors for the 18 MV beam. (**Middle**) Ratio of used calibration factors to mean calibration factors. (**Bottom**) The ten separate sets of calibration factors normalized to the mean calibration factors.

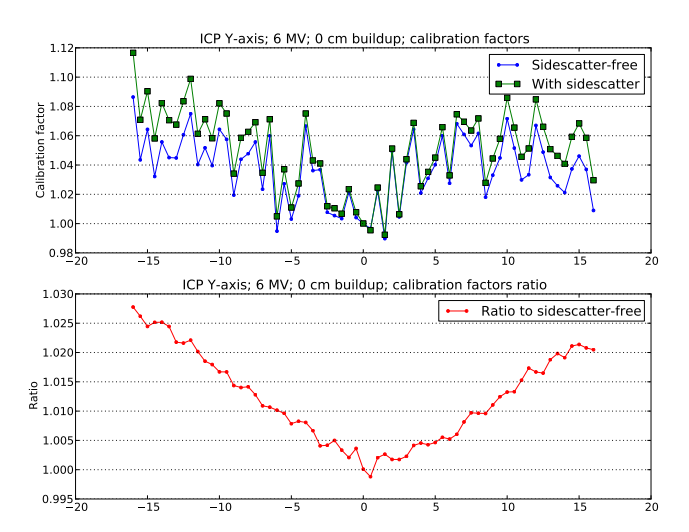


Figure 4–5: (**Top** 6 MV Y-axis calibration factors measured with no additional buildup on the ICP with and without 3 cm tall sidescatter at the array ends. (**Bottom**) Ratio of calibration factors with sidescatter to those without it.

that very probably, the differences in the two curves are due to variations in beam symmetry, as the shape of the ratio curve on figure 4–5 is very similar to what was presented earlier. At the time of the measurements, since it appeared that using sidescatter brought no new benefits, it was decided to use a sidescatter-free calibration for the 6 MV beam.

The results regarding the 18 MV beam are displayed on figure 4–6. This time, the ratio between the two curves is much closer to one. Differences between the two calibrations are of less than 0.5~% for all detectors.

These tests comparing calibrations with sidescatter to calibrations without sidescatter were made before concerns over calibration reproducibility due to beam symmetry variations were raised. It would have been better to do ten separate calibrations with sidescatter an take the mean calibration. This would have made comparisons between sidescatter calibration and sidescatter-free calibration much more significant.

At the time of the tests, unaware of the calibration reproducibility problem, it was seen that sidescatter calibration for the 6 MV beam clearly worsened agreement between two half-profiles,

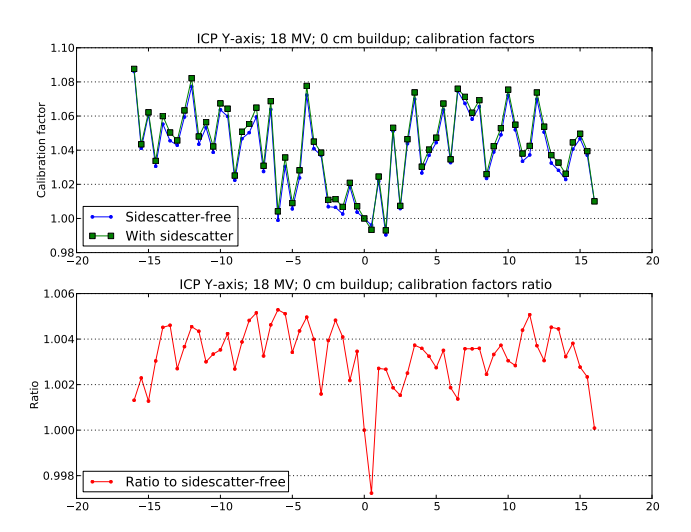


Figure 4–6: (**Top**) 18 MV Y-axis calibration factors measured with no additional buildup on the ICP with and without 3 cm tall sidescatter at the array ends. (**Bottom**) Ratio of calibration factors with sidescatter to those without it.

introducing more noise near the beam central axis in the combined profiles. That prompted the use of sidescatter-free calibration factors for the 6 MV beam. The shape of the curve on the bottom graph of figure 4–5 clearly shows how the noise problem presented earlier in figure 4–2 is amplified when the measured sidescatter calibration factors are used.

In the case of the 18 MV beam, the difference between sidescatter calibration factors and sidescatter-free calibration factors was not so important as in the 6 MV case. Using them did not clearly worsen the combined profiles, as it did for the 6 MV beam. Because of this, and because use of sidescatter during calibration theoretically brings the calibration measurement setup closer to the measurement setup used in this project (which also uses sidescatter near the +Y end of the ICP's Y-axis), it was decided at the time to use the sidescatter calibration factors for the 18 MV beam.

It would have been more rigorous to use calibration factors measured with the same method for both energies. However, as shown in figure 4–6, the difference between the two calibrations is

minimal and should not have affected much either the agreement of ICP measurements with the SWT measurements nor the final beam model parameters in Pinnacle.

The reason behind the large differences between the two ratio curves presented in figures 4–5 and 4–6 was only understood at a late point in the project, after all beam modeling was done. It is at present apparent that at least the 6 MV sidescatter calibration measurement suffered from a beam symmetry variation of some importance.

4.2.2 Combination of Measurements

The combination of two ICP measurements to give full profiles can sometimes lead to a noisy profile shape. Figure 4–7 shows two examples of ICP measurements that are combined.

In the left portion of this figure, the two measurements differ at the beam center by less than half a percent. The resulting profile should be fairly normal. In the right portion, however, the two measurements differ by almost a percent near the beam center. There is a visible difference in height between the two. The combined profile will present some high-frequency noise as a result since in the central field region, consecutive points alternate from one measurement to the other.

There are many sources of error in the total corrected counts recorded for each detector of each half-profile:

Field transitions Wrongly determined field transitions in the cumulative corrected counts time series of a .prm file introduce total corrected counts errors in two neighboring fields. See figure 3–5 for an example of determined transitions for an ICP file.

Variations in temperature and pressure Over the course of the measurements, with the whole process lasting for several hours, air temperature and pressure inside the ICP's cavities can vary. There is some conflicting information available regarding this issue and its correction with the ICP. In their article, Simon et al. indicate that a pressure-temperature correction factor is applied as part of the corrected counts calculation [15]. However, the ICP software's online help explicitly mentions that no air density correction is made in the calculation of corrected counts [14]. Thus, we may assume that no temperature-pressure correction is actually made and that this may cause variations in measured total corrected counts for the

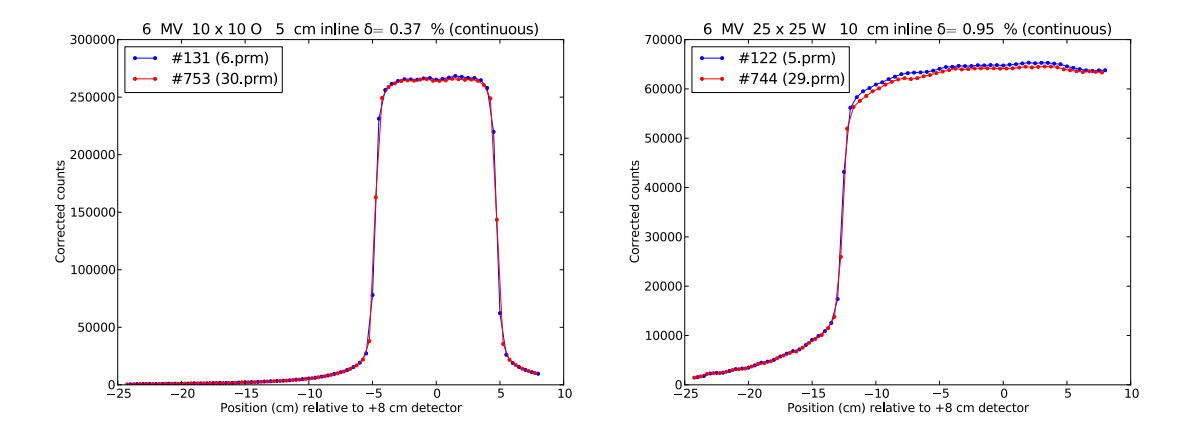


Figure 4–7: Shown here are two examples of pairs of half-profiles which will be combined together. The graph title shows the beam energy, field size, whether the field is wedged or open, the depth, the profile direction, the percentage difference between the total counts of the two measured half-profiles accumulated in the +8 cm detector of the ICP and the ICP acquisition mode. The difference should ideally and theoretically be zero. The legend lists measurement number followed by the file name where the ICP measurement was taken from in parentheses.

same beam configurations measured some time apart. This was confirmed by applying a temperature-pressure correction factor on all recorded corrected counts by using the recorded signals from the ICP's thermistor and pressure transducer. After correction, the agreement between matching half-profiles improved approximately by 0.4 % on average. An example of the improved agreement following the application of a pressure and temperature correction factor is shown in figure 4–8.

Different centering Two separate manually-defined positions of the ICP are used for half-profiles, with opposite orientations. Undesired inplane and/or crossplane shifts can occur with one orientation relative to the other. Only the shift along the detector array axis can be detected and compensated for, as explained earlier.

ICP and linac reproducibility Some variation is expected from one irradiation to the next in total measured corrected counts. As shown earlier in table 4–1, the continuous acquisition mode of the ICP under our linac presents a reproducibility of approximately 0.2 %, standard deviation from the mean for the 6 MV beam.

Linac output drift It is possible the linac output drifts over the time needed to acquire the measurements. Because no reference chamber is used and the total absolute corrected counts for each irradiation is used, this would not be compensated for by the current method. An improvement could be to perform output spot-checks at a fixed interval, say 1 hour, during the beam acquisition. These would allow verification that the output is not changing significantly or, in the case that it is, to compensate for the drift.

Different SSD Even if the SSD is always constant at 90 cm, this is still adjusted manually inbetween irradiations, whenever depth in water-equivalent material is changed. It may happen that SSD was not exactly the same for the two half-profiles, although one tries to keep this parameter as constant as possible. A Vernier caliper with precision to one one-hundredth of a millimeter affixed to the linac head was use to adjust SSD for each measurement. It is estimated that the SSD was always within ± 0.5 mm of the desired value, which by the inverse square law should introduce variations in measured ionization of the order of ± 0.1 %.

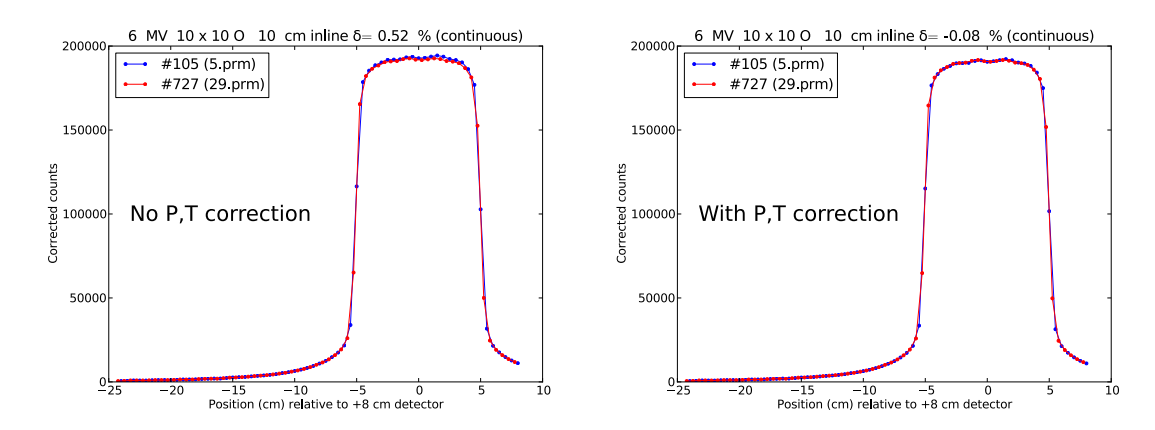


Figure 4–8: Example of the effect of applying a pressure and temperature correction factor to half-profile measurements. The percentage difference of the beam central axis detector is given by the symbol δ on the graph titles.

4.2.3 Smoothing of Profiles

As mentioned in chapter 3, smoothing was applied to counteract the noise introduced by variations in measured total counts. Additionally, this helped counter-act the effect of the application

of calibration factors measured in a standard ICP setup. Figure 4–9 demonstrates the effect of the smoothing procedure.

The smoothing procedure greatly attenuates the noise introduced by differences in measured total corrected counts and calibration factor variation towards array ends. The profile shape is not overly changed since smoothing only occurs over the central field region, and not in the penumbrae or umbra.

4.2.4 Percent Depth Dose Curve Fitting

Validation of the fitting procedure with SWT data showed that the fitting function was able to fit PDDs with success at all field sizes and energies, regardless if the field was open or wedged, except for a single case. Figures 4–10 and 4–11 show the fitting results for extreme and middle-of-the-run field sizes, for a 6 MV photon beam. The SWT data shown in these figures was acquired with a CC13 ionization chamber. The tolerance level of the gamma function [36] used for the comparison of the fit to the measurements is 1 %, 1 mm and is shown in a red dot-dash line on the graphs. No lower spatial tolerance could be set as the reference measurement points are already spaced 1.0 mm apart. 1.0 % of the maximum PDD (i.e. 1.0 % of 100 = 1) was chosen as percent depth dose tolerance.

What can be gathered from these figures is that the fitting function rarely is able to reproduce the measurements near the surface. However, within 1 cm of the surface in 100 % of the cases and within 1 mm of the surface for over 90 % of the cases, the problem has already subsided to a point where the fit represents the measurements adequately, within the specified tolerance of 1 %, 1 mm gamma. The reader is reminded that the fit passing through measured PDD(z = 0 cm) was one of the constraints imposed during the optimization procedure that minimizes the sum of squared differences between fit and measurement. This helps greatly towards agreement between fit and measurement in the buildup region.

For the particular case of the 3×3 cm² wedged field, in figure 4–11, the fitting curve cannot represent the measurements correctly near the dose maximum and near 10 cm. This is an extreme case and this behavior is not seen for other fields. The increased presence of noise in the CC13

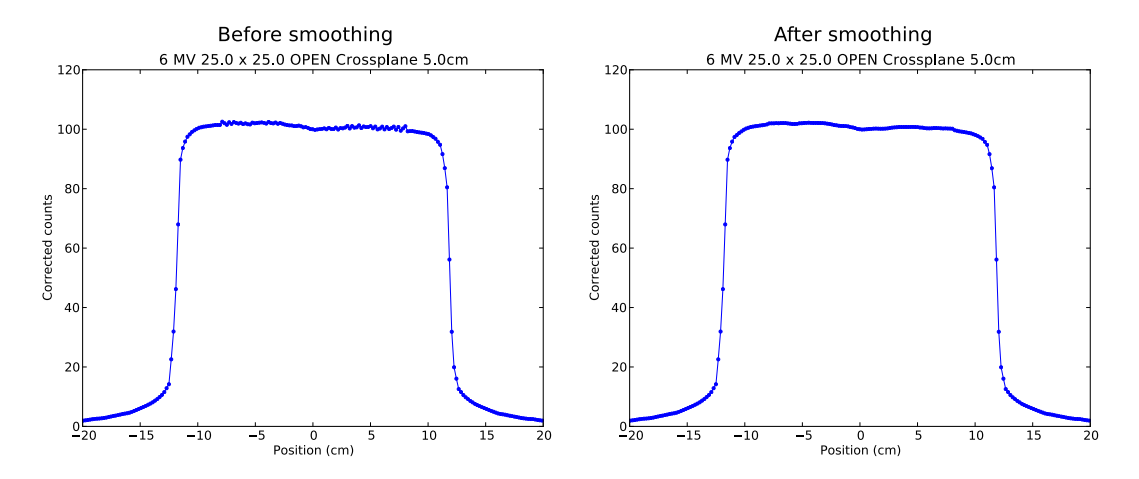


Figure 4–9: 6 MV, 25×25 cm² wedged profiles at 10 cm depth before and after smoothing.

measurements of small wedged fields can contribute to this. For all field sizes, open or wedged, except the 3×3 cm² wedged field case mentioned above, $\gamma < 1$ was satisfied for all depths greater than 1 cm (1 mm in most cases).

It was thus deemed that the chosen fitting procedure was appropriate to recover full PDD curves from a limited set of available measured depths. The possibility of doing this was hinted at in previous publications [31, 32]. The fitting procedure seems to have the additional benefit of denoising the noisier PDD curves (such as for the wedged fields, particularly at greater depths and small field sizes). Note that a 6 MV beam was chosen for this fitting procedure validation as the deeper z_{max} of a 18 MV beam actually makes the fitting procedure easier, given the set of available measured depths. With an 18 MV beam, more points fall in the buildup region and the fitting procedure is facilitated. For completeness, it was verified that the fitting procedure did work for all 18 MV fields, but the results are not presented here.

4.3 Relative Dose Factors

Relative dose factors (also known as output factors, OF) were available to be calculated from the measured profiles at 10 cm depth using the total corrected counts recorded by the detector

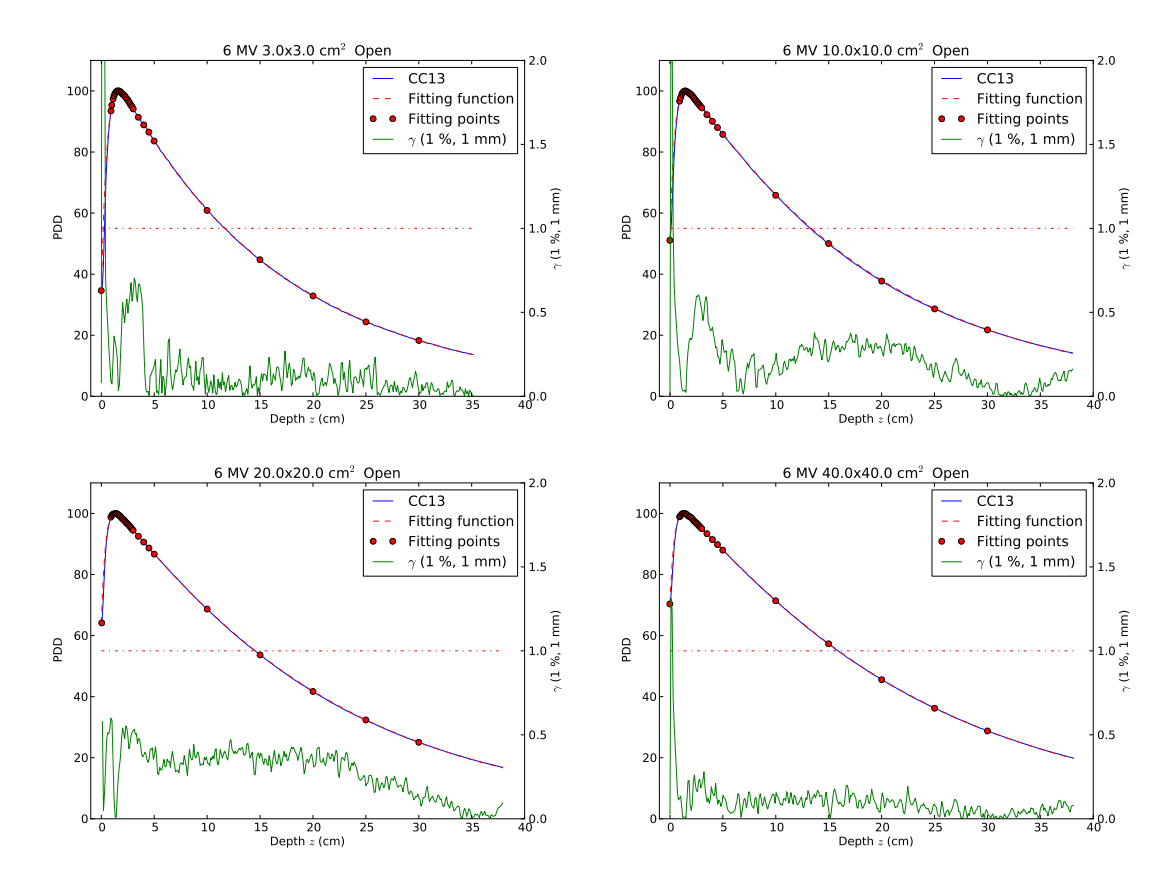


Figure 4–10: Results of the PDD fitting procedure on SWT data for open fields.

placed on the beam central axis. The results of OF measurements are presented in figures 4–12 and 4–13 for the 6 MV beam and the 18 MV beam respectively.

As can be seen from these figures, OF are underestimated for the smallest field sizes. This can be explained by the relatively large size of the ICP's cavities and by the difficulty in centering the ICP with a detector exactly under the beam central axis, where the profile is maximum for small fields.

On the other hand, OF are overestimated for large field sizes. This is particularly true for the 6 MV beam compared to the 18 MV beam. The higher cross-section for Compton scattering at 6 MV than at 18 MV indicates that a greater proportion of photons are scattered in-plane in the detector array (in fact, about twice as many). It may be that these extra photons traveling inside

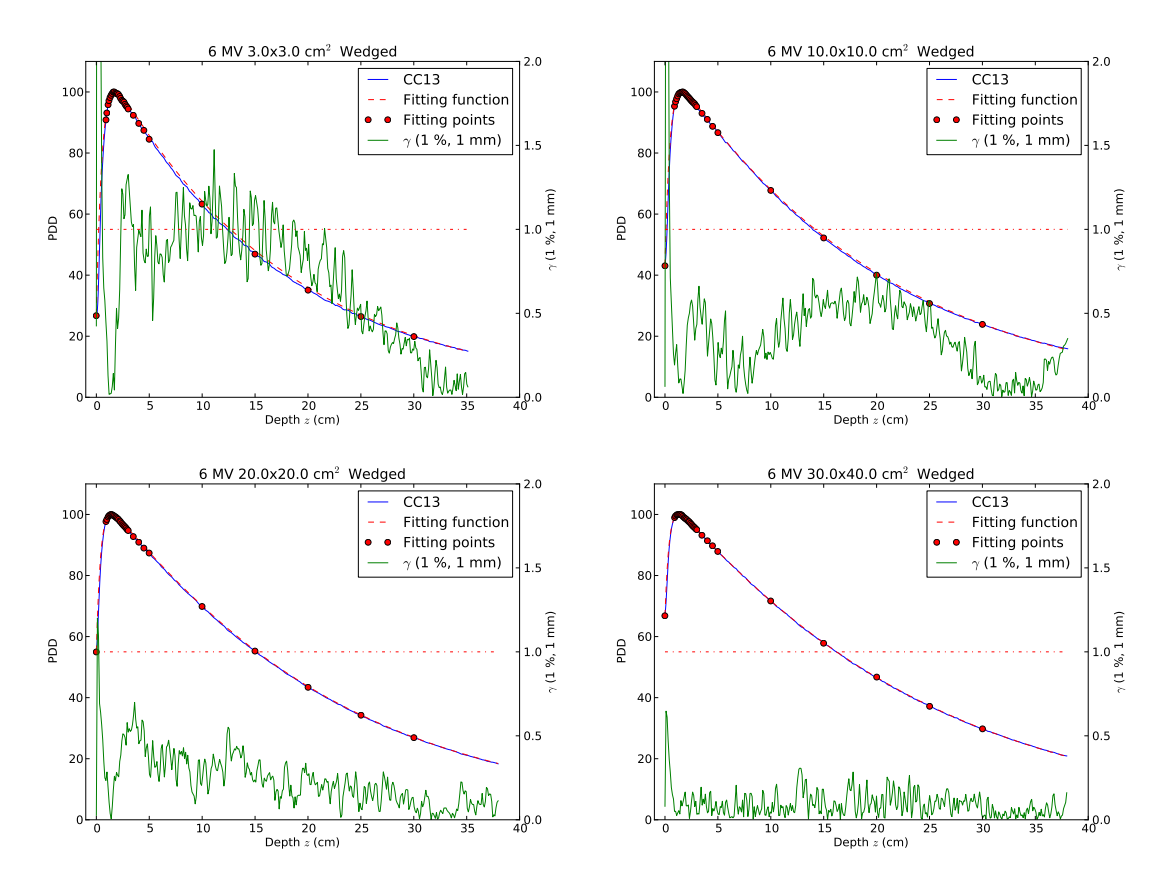


Figure 4–11: Results of the PDD fitting procedure on SWT data for wedged fields.

the array lead to higher measured output factors. Depending on the trajectory of the in-plane scattered photon, it may encounter a series of air-filled cavities interspaced by walls of aluminum; or it may interact with the ICP's printed circuit board, or simply travel through polycarbonate, which is nearly water-equivalent.

In summary, the scattering conditions around the detector placed on the beam central axis are very different from those of a single detector submerged in water, as is the case in a SWT system. This highlights the fact that the ICP is not an ideal instrument for making point measurements. These differences in scattering conditions can cancel themselves out when making relative measurements using the array of detectors. The ICP's construction even includes extra "dummy" detector

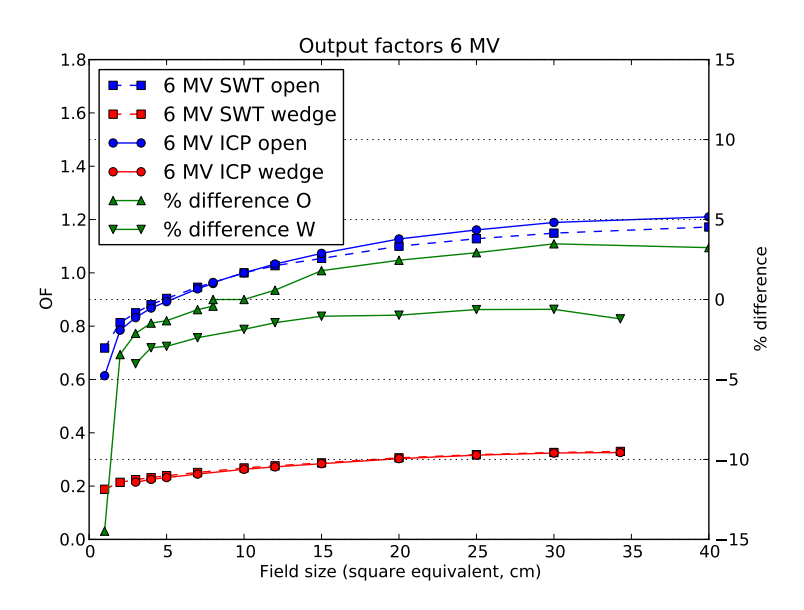


Figure 4–12: ICP-measured 6 MV output factors vs SWT-measured output factors.

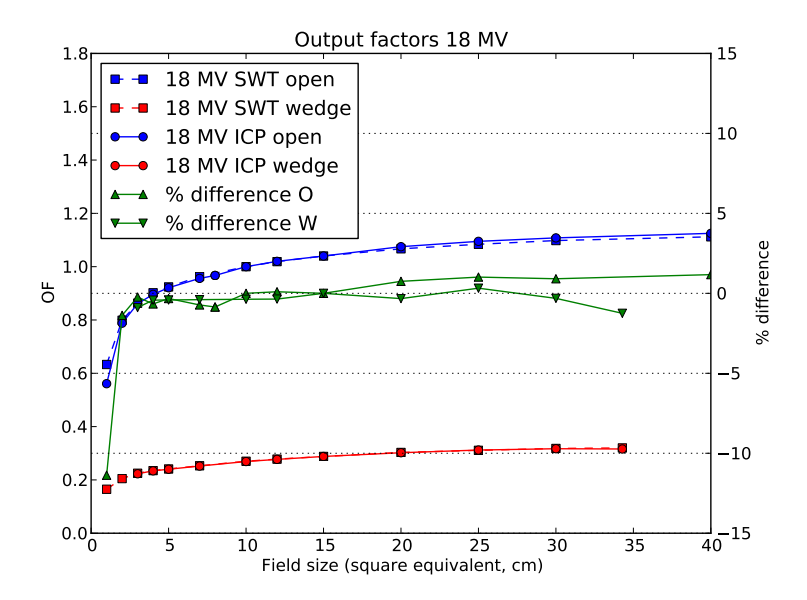


Figure 4–13: ICP-measured 18 MV output factors vs SWT-measured output factors.

cavities near the ends of each of its axes to provide similar scattering conditions for all its active detectors [12].

Simon et al., as shown in chapter 2, notice the same trends during their characterization of the ICP: underestimation at small field sizes, overestimations at large field sizes. The discrepancies they observe, however, are smaller in amplitude than the ones observed here. It remains unclear why this is so.

4.4 Comparisons with Water Tank Measurements

Tables 4–2 and 4–3 compare SWT-acquired data to ICP-acquired data for the 6 MV beam and the 18 MV beam respectively. The metrics used for comparison are those described previously in table 3–2. The mean Gamma and mean percent differences are calculated over all depths and all positions for the profiles; then over all depths for the PDDs. MLC fields denote fields where collimator jaws define a 20 × 20 cm² field at the isocenter, but are further collimated by the MLC leaves to a smaller area. More detailed results can be found in the Appendices, where graphs are shown. These are not presented here due to concerns about the space required for showing these comparison reports. In these graphs, the machine "Salle_9_clinique" represents the clinical beam model/SWT measurements, while the machine "IC_FINAL2" represents the ICP beam model/ICP measurements.

The comparisons show that in general there is agreement between SWT data and ICP data. Some problematic areas are:

- PDD buildup region Due to the measured surface PDD value imposed during the PDD fitting procedure, the error in the buildup region is relatively minor. However, it does happen, particularly for small field sizes, that the fit is not able to reproduce SWT measurements as we approach the dose maximum.
- **PDD near z**_{max} This is an area of large discrepancies between ICP data and SWT data. The reader is reminded that the normalization depth used in this project is 10 cm; hence important differences can appear near the depth of dose maximum. The ICP underresponds in comparison with the CC13 in a SWT. It is especially evident in the PDDs of large ($\geq 15 \times 15 \text{ cm}^2$)

Table 4–2: Summary of acquisition data comparison between SWT and ICP for the 6 MV beam. For more detailed results, consult Appendix A.

Field			OA	ARs			PI	DDs	
		$\overline{\gamma}$	γ_{rate}	$\overline{\%}$	$\%_{\mathrm{rate}}$	$\overline{\gamma}$	γ_{rate}	$\overline{\%}$	$\%_{\mathrm{rate}}$
$3 \times 3 \text{ cm}^2$	О	0.16	99.8	1.26	83.6	0.17	96.6	0.89	96.0
$10 \times 10 \; \mathrm{cm}^2$	O	0.24	99.4	1.00	90.6	0.21	99.7	0.59	97.4
$20 \times 20 \ \mathrm{cm}^2$	O	0.26	99.1	1.07	89.7	0.40	90.3	0.90	88.3
$40 \times 40 \; \mathrm{cm}^2$	O	0.46	90.5	1.36	86.6	0.47	87.7	1.06	85.1
$3 \times 3 \text{ cm}^2$	W	0.15	99.3	1.27	84.7	0.19	96.6	0.99	96.0
$10 \times 10 \text{ cm}^2$	W	0.19	99.6	0.91	90.7	0.16	99.7	0.54	96.9
$20 \times 20 \text{ cm}^2$	W	0.22	99.0	0.97	90.4	0.35	99.7	0.78	97.7
$30 \times 40 \ \mathrm{cm}^2$	W	0.49	85.7	1.51	79.0	0.36	93.7	0.78	92.6
$3 \times 3 \text{ cm}^2$	MLC	0.19	99.8	0.77	92.6	0.16	96.2	0.65	93.6
$10 \times 10 \; \mathrm{cm}^2$	MLC	0.19	99.1	0.78	92.0	0.17	98.6	0.60	96.5
Overall		0.23	97.7	1.11	87.5	0.26	96.3	0.76	94.2

Table 4–3: Summary of acquisition data comparison between SWT and ICP for the 18 MV beam. For more detailed results, consult Appendix B.

Field			OA	Rs			PΙ	DDs	
		$\overline{\gamma}$	γ_{rate}	$\overline{\%}$	$\%_{\rm rate}$	$\overline{\gamma}$	γ_{rate}	$\overline{\%}$	$\%_{\rm rate}$
$3 \times 3 \text{ cm}^2$	О	0.11	100.0	0.97	86.9	0.30	96.0	1.04	94.0
$10 \times 10 \; \mathrm{cm}^2$	O	0.14	100.0	0.64	93.1	0.17	97.1	0.63	94.3
$20 \times 20 \text{ cm}^2$	O	0.19	99.8	0.83	92.1	0.17	99.4	0.50	94.0
$40 \times 40 \ \mathrm{cm}^2$	O	0.25	97.1	0.95	93.8	0.28	92.6	0.60	92.0
$3 \times 3 \text{ cm}^2$	W	0.12	100.0	0.92	87.8	0.42	95.1	1.44	94.0
$10 \times 10 \text{ cm}^2$	W	0.15	100.0	0.68	93.6	0.21	97.7	0.70	93.1
$20 \times 20 \text{ cm}^2$	W	0.25	99.3	0.95	92.1	0.19	99.7	0.57	94.9
$30 \times 40 \text{ cm}^2$	\mathbf{W}	0.52	86.3	1.57	82.1	0.40	99.7	0.89	97.1
$3 \times 3 \text{ cm}^2$	MLC	0.20	99.2	0.74	93.2	0.23	93.6	0.88	91.6
$10 \times 10 \text{ cm}^2$	MLC	0.16	99.8	0.61	94.6	0.33	95.4	1.04	93.9
Overall		0.18	99.0	0.89	90.4	0.29	95.7	0.89	92.6

open fields at 6 MV. This is of concern as good agreement near z_{max} is critical. The same phenomenon was observed by Simon *et al.* [15], in that the largest observed differences between ICP and CC13 in water were for a large field size at 6 MV. The difference in measured PDD near z_{max} is not a result of the PDD fitting procedure. Rather, it is a direct consequence of the measured PDD points obtained with the ICP (the fit passes quite closely to the measured points, but the points themselves lead to this discrepancy). Open field PDDs are in general different between ICP and SWT, while wedged fields are in good agreement. For 18 MV, agreement is highest for open field PDDs, but even wedged field PDDs agree reasonably well.

- OAR penumbrae In all penumbrae we observe a sharp rise in the gamma metric and the percent difference metric. Gamma is preferable to use under the circumstances of the penumbrae (where a high dose gradient exists). However, it is quite common for even the 2.0 %, 2 mm gamma metric to go beyond the tolerance in these regions. The reasons for this are many. Differences in profile centering will cause this, but these are minimized if profiles are centered numerically before importation into the TPS. The ICP response function is assuredly different from that of an ionization chamber or a diode used in a SWT; the blurring of the true profile will be different, producing differences in high dose gradient regions. Finally, it is possible field sizes were slightly different at the time of ICP measurement than they were at the time of the SWT measurements (which were made at the time of the initial beam commissioning of the linac in 2009).
- OAR central region near \pm 8 cm Differences in the two measurements combined to make the profile sometime caused bumps in the profile shape which disagree with SWT measurements. As shown earlier, this is a direct consequence of (and is mostly due to) the calibration factors used.
- 6 MV crossplane OAR central region There was a known symmetry problem with the 6 MV beam in the crossplane direction at the time of ICP acquisition which was not present at the time SWT measurements were made (1.9 % area symmetry for the ICP measurement). As a result, there is some disagreement in some of the large crossplane profiles at 6 MV. This symmetry problem is discernible on the previously shown figure 4–9.

4.5 Comparisons with Clinical Model

We now compare the beam model used clinically to ICP measurements and the ICP beam model to the ICP measurements to ensure that the constructed ICP beam model corresponds better to its data than the clinical model does. The results are presented in table 4–4 for the 6 MV beam and in table 4–5 for the 18 MV beam.

The results show that the model constructed with the ICP data fits better the ICP measurements than the clinical model which was constructed with SWT data, both for the 6 MV and the 18 MV beams. This is true for the overall comparison, where comparison metrics are averaged over all fields, and true for all fields individually as well, except a few exceptions (for instance the $40 \times 40 \text{ cm}^2$ open field at 18 MV).

4.6 Validation of Beam Models

The results of the validation of the beam models (6 and 18 MV) are separated into two types: scans and point measurements. The reader is referred to section 3.2.4 for a more detailed description of the method used for model validation. The results are presented, for brevity, in tables as averages over the many fields of a certain type. However, detailed results (i.e. scan-specific or point-measurement specific results) were examined. Overall, the summarized results are consistent with, and representative of, the specific results obtained in each case.

4.6.1 6 MV Model Validation

Point measurement absolute dose differences between model and experimental validation are presented for the 6 MV beam in table 4–6. In the following tables one should look to compare the clinical SWT validation results with the validation results from the ICP beam model. The reference validation values used in these tables were measured with a SWT system at the time of the initial linac acquisition.

It is apparent from the point measurement results that the ICP beam model does not agree as well with experimental measurement as the clinical SWT model does. This is especially true for wedged fields in general and irregular or asymmetrical open fields.

Table 4–4: Model-data comparisons for the $6~\mathrm{MV}$ beam. For more detailed results, consult Appendix C.

Field		SWT	Model	vs ICF	Data	ICP	Model	vs ICP	Data
		$\overline{\gamma}$	γ_{rate}	$\overline{\%}$	$\%_{\rm rate}$	$\overline{\gamma}$	γ_{rate}	$\overline{\%}$	$\%_{\rm rate}$
$3 \times 3 \text{ cm}^2$	О	0.21	98.4	1.32	87.7	0.20	99.9	0.99	91.3
$10 \times 10 \; \mathrm{cm}^2$	O	0.24	98.6	1.03	89.7	0.20	99.9	0.75	93.8
$20 \times 20 \text{ cm}^2$	O	0.40	92.7	1.40	78.3	0.31	95.4	1.08	85.7
$40 \times 40 \ \mathrm{cm}^2$	O	0.58	79.9	1.60	74.9	0.51	85.3	1.27	86.8
$3 \times 3 \text{ cm}^2$	W	0.18	98.9	1.29	87.3	0.21	99.0	1.10	90.7
$10 \times 10 \text{ cm}^2$	W	0.30	94.9	1.13	88.1	0.28	96.2	0.92	91.6
$20 \times 20 \text{ cm}^2$	W	0.46	90.4	1.40	81.2	0.41	91.0	1.25	82.8
$30 \times 40 \text{ cm}^2$	W	0.76	79.6	1.98	74.4	0.64	83.2	1.63	77.2
$3 \times 3 \text{ cm}^2$	MLC	0.36	95.2	1.38	83.9	0.23	99.3	0.92	91.6
$10 \times 10 \text{ cm}^2$	MLC	0.26	99.2	0.99	91.3	0.23	99.9	0.78	93.6
Overall		0.34	94.7	1.32	84.3	0.30	96.2	1.08	88.3

Table 4–5: Model-data comparisons for the 18 MV beam. For more detailed results, consult Appendix D.

Field		SWT	Model	vs ICF	P Data	ICP	Model	vs ICP	Data
		$\overline{\gamma}$	γ_{rate}	$\overline{\%}$	$\%_{\rm rate}$	$ \overline{\gamma}$	$\gamma_{\rm rate}$	$\overline{\%}$	$\%_{\mathrm{rate}}$
$3 \times 3 \text{ cm}^2$	О	0.19	99.7	1.14	88.0	0.19	100.0	0.96	89.5
$10 \times 10 \; \mathrm{cm}^2$	O	0.20	98.7	0.81	92.3	0.18	99.2	0.64	94.8
$20 \times 20 \ \mathrm{cm}^2$	O	0.28	96.5	0.96	91.3	0.23	98.7	0.80	93.9
$40 \times 40 \ \mathrm{cm}^2$	O	0.44	91.5	1.25	88.5	0.45	90.0	1.27	87.1
$3 \times 3 \text{ cm}^2$	W	0.25	99.1	1.41	86.3	0.17	100.0	0.90	90.3
$10 \times 10 \text{ cm}^2$	W	0.39	91.6	1.35	80.8	0.30	94.1	0.97	86.2
$20 \times 20 \ \mathrm{cm}^2$	W	0.58	86.6	1.74	78.4	0.49	88.8	1.46	79.5
$30 \times 40 \ \mathrm{cm}^2$	W	0.90	75.6	2.38	71.0	0.82	75.9	2.08	71.1
$3 \times 3 \text{ cm}^2$	MLC	0.41	89.9	1.35	81.5	0.21	98.1	0.72	94.7
$10\times10~\mathrm{cm^2}$	MLC	0.24	98.6	0.86	92.6	0.27	98.7	0.86	94.5
Overall		0.34	94.7	1.25	86.3	0.29	95.9	1.04	88.9

Table 4–6: Validation results for point measurements made in 6 MV beam using the clinical SWT model and the ICP model. The average absolute difference in percentage over all fields of a certain type between the TPS-calculated dose and the dose measured for the model validation field is shown.

Field Type	6 MV SW	Γ Model vs Validation Set	6 MV ICP Model vs Validation Set				
	Open	Wedged	Open	Wedged			
Square	0.30	0.30	0.52	0.65			
Rectangular	0.81	1.13	0.63	0.90			
Irregular	0.88	1.08	1.24	1.50			
Asymmetrical	1.00	2.46	2.33	2.34			
$SSD \neq 90 \text{ cm}$	0.37	0.63	0.27	1.53			

Table 4–7: Validation results for scans made in the 6 MV beam using the clinical SWT model and the ICP model.

Scan Type	6 MV	SWT	Model v	vs Validation Set	6 MV	ICP :	Model vs	Validation Set
	$\overline{\gamma}$	γ_{rate}	$\overline{\%}$	$\%_{\mathrm{rate}}$	$\overline{\gamma}$	$\gamma_{\rm rate}$	$\overline{\%}$	$\%_{\mathrm{rate}}$
PDD	0.23	97.2	0.66				1.24	88.3
OAR	0.74	80.3	6.54	61.6	0.80	78.2	6.67	60.3
Overall	0.67	82.5	5.67	66.2	0.75	80.1	5.87	64.1

The scan results presented in table 4–7 indicate as well that the 6 MV ICP beam model is overall significantly worse at predicting measured dose distributions than the 6 MV SWT model.

However, in all cases except asymmetric fields, the average percent difference is less than 2 % between the ICP beam model and the SWT validation measurements. In some cases, e.g. the rectangular fields, the ICP beam model validation results are even better than the clinical beam model's.

Even if the ICP's 6 MV beam model did not validate as well as the SWT model, the model was kept in order to investigate further and move on within the project. If a choice had to be made, however, on which model (SWT or ICP) to use clinically, it is clear from these results that the SWT model should be chosen. At this point, it cannot be concluded on exactly what improvements need to be made to the 6 MV ICP beam model for it to validate as well as the clinical model. It seems the inferior validation results are simply a result of the measured data obtained from the ICP. It was already demonstrated that the ICP beam model fits the ICP beam data better than the clinical beam model does. This means that characteristics of the measured data were carried over into the beam model. The combined effect of the particularities of the ICP beam acquisition dataset lead to a model validation results that are sub-par to those obtained with the clinical model.

4.6.2 18 MV Model Validation

Similarly, point measurements absolute dose differences between model and experimental validation are presented for the 18 MV beam in table 4–8. Contrary to the case of the 6 MV beam model, the 18 MV ICP beam model agreement with experimental data is generally on par with the 18 MV SWT beam model (and in the case of square fields, in better agreement with SWT measurements).

The validation scan results themselves, presented in table 4–9, are comparable between the ICP model and the SWT model. The PDD results do show a little less agreement in the case of the ICP beam model. All in all, it seems the 18 MV ICP beam model can be considered almost as good as the SWT beam model for predicting the measured dose distributions of the validation fields, except in the case of PDDs, where slight differences exist. This is consistent with the acquisition

Table 4–8: Validation results for point measurements made in 18 MV beam using the clinical SWT model and the ICP model. The average absolute difference in percentage over all fields of a certain type between the TPS-calculated dose and the dose measured for the model validation field is shown.

Field Type		T Model vs Validation Set		
	Open	Wedged	Open	Wedged
Square	0.42	0.82	0.17	0.52
Rectangular	0.46	0.86	0.49	0.87
Irregular	1.17	1.07	1.20	1.39
Asymmetrical	0.92	2.28	0.86	2.30
$SSD \neq 90 \text{ cm}$	0.13	0.57	0.33	0.97

Table 4–9: Validation results for scans made in the $18~\mathrm{MV}$ beam using the clinical SWT model and the ICP model.

Scan Type	18 M	V SWT	Model	vs Validation Set	18 M	V ICP	Model vs	Validation Set
	$\overline{\gamma}$	γ_{rate}	$\overline{\%}$	$\%_{\mathrm{rate}}$	$\overline{\gamma}$	$\gamma_{\rm rate}$	$\overline{\%}$	$\%_{\mathrm{rate}}$
PDD	0.23	97.3	0.75	93.0	0.32	95.6	0.98	89.7
OAR	0.68	79.6	6.95	55.2	0.68	79.2	6.89	53.9
Overall	0.62	81.8	6.05	60.4	0.63	81.2	6.04	58.8

data comparisons presented earlier for the 18 MV beam. Based only on these validation results, the 18 MV ICP beam model could be used clinically as well as the SWT model.

4.7 Calculated Dose Distribution Comparisons

4.7.1 Calculated Dose Distributions in Water Phantoms

In this section, we make comparisons between calculated dose distributions using the ICP beam model and the clinical SWT model. We start off by calculating dose distributions for some simple fields in water phantoms and subsequently calculating per-voxel dose differences. These comparisons simply highlight visually any differences between the beam models. The studied fields, both for the 6 MV beam and the 18 MV beam, are the following:

- $40 \times 40 \text{ cm}^2$ open field;
- $10 \times 10 \text{ cm}^2$ open and wedged fields;
- $8 \times 8 \text{ cm}^2$ MLC-defined field. The collimator jaws are placed so they define a $20 \times 20 \text{ cm}^2$ field size at isocenter and the beam is further collimated down to an $8 \times 8 \text{ cm}^2$ area using the MLC leaves.

More fields were studied but are not presented here due to length of text concerns.

For these comparisons, the 3DVH® software is employed with the "dose difference/distance-to-agreement" comparison method. The dose and distance-to-agreement criteria were both set to zero, making the comparison straight-up per-voxel dose difference. Red voxels indicate higher dose in the ICP beam model than in the clinical SWT model. Blue voxels indicate the contrary.

6 MV Water Phantom Dose Difference Results

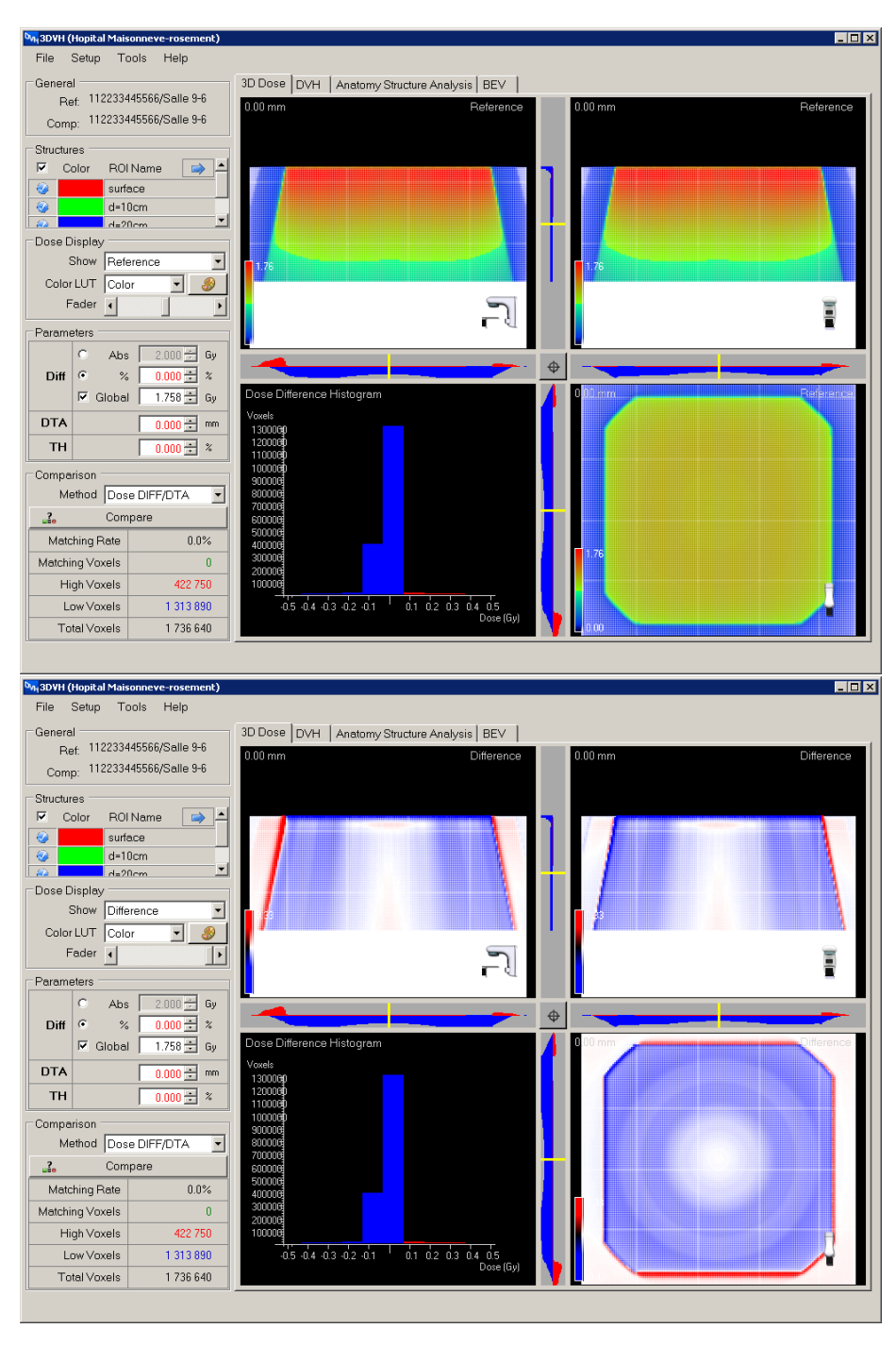


Figure 4–14: 6 MV $40 \times 40 \text{ cm}^2$ open water phantom calculation. (**Top**) Reference distribution (SWT model). (**Bottom**) Dose difference.

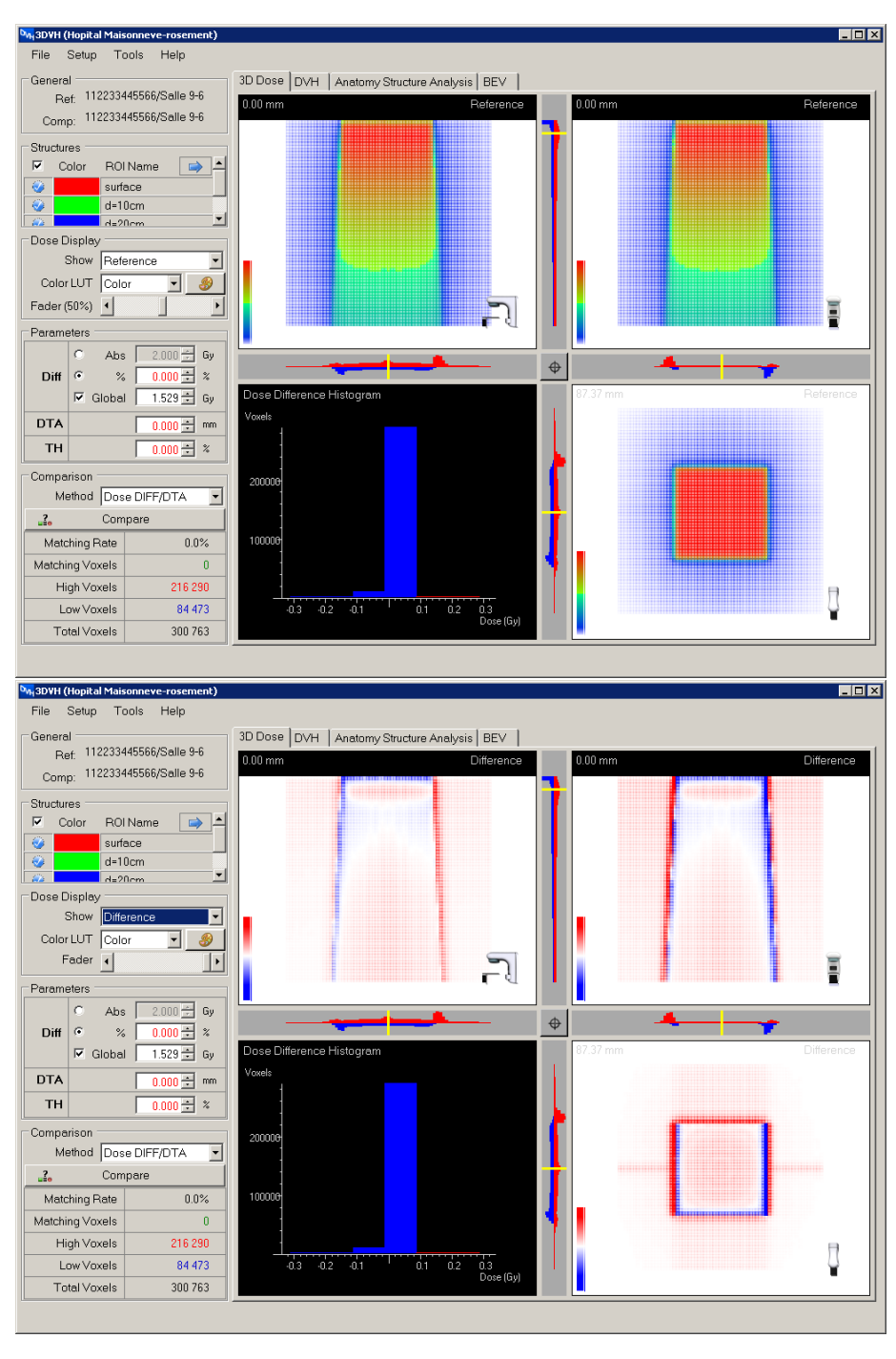


Figure 4–15: 6 MV $10 \times 10 \text{ cm}^2$ open water phantom calculation. (**Top**) Reference distribution (SWT model). (**Bottom**) Dose difference.

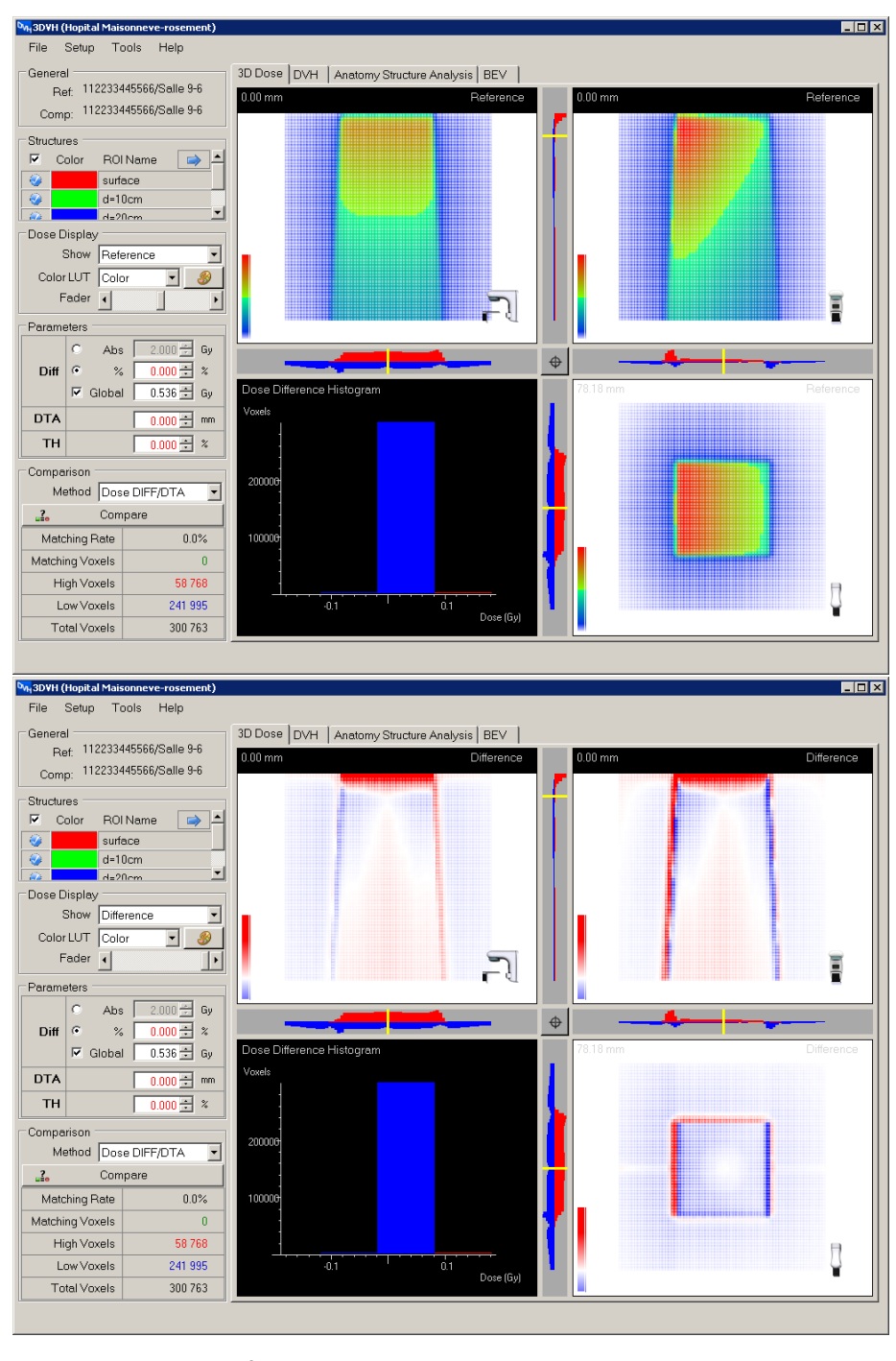


Figure 4–16: 6 MV 10×10 cm² wedged water phantom calculation. (**Top**) Reference distribution (SWT model). (**Bottom**) Dose difference.

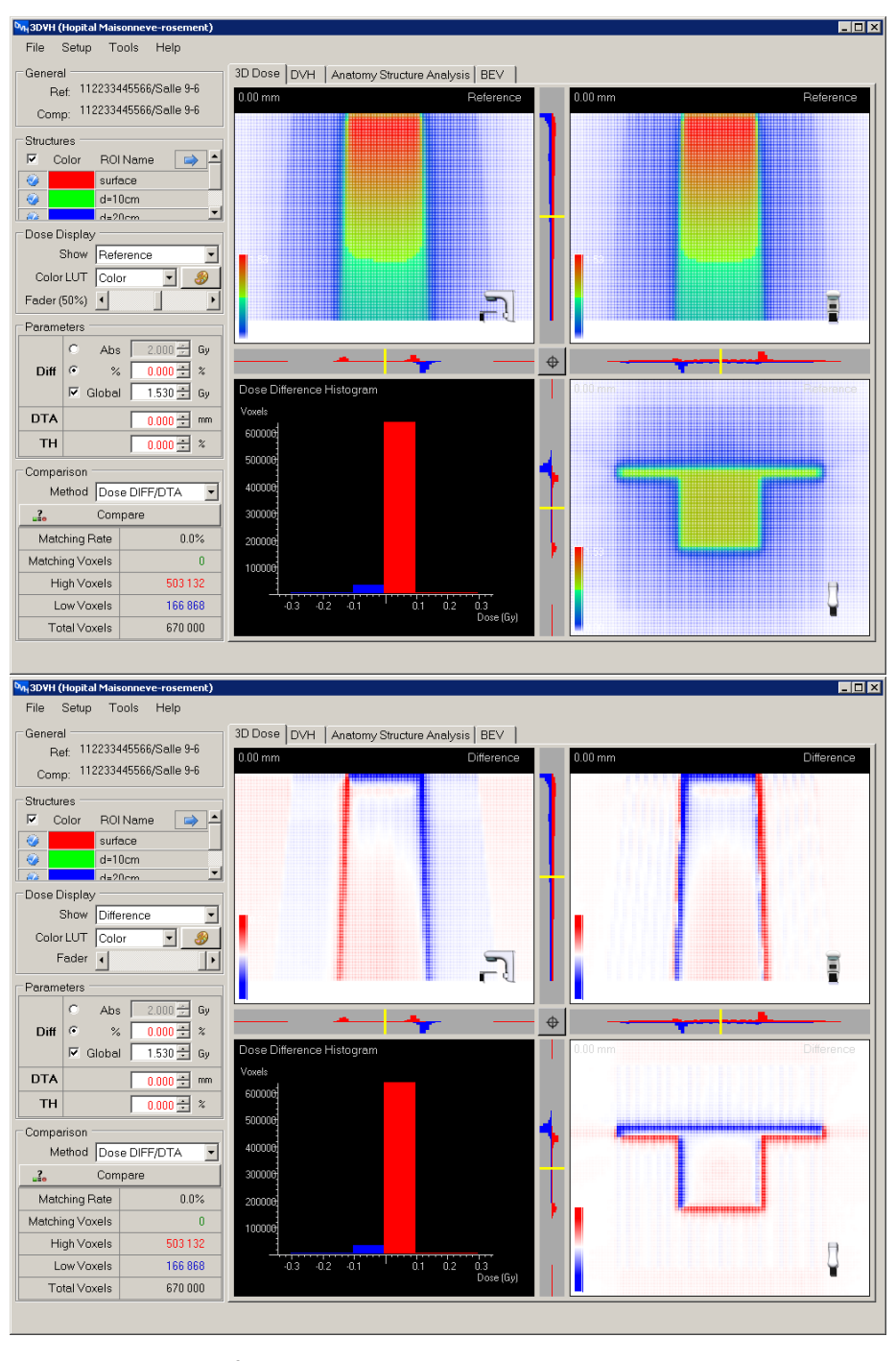


Figure 4–17: 6 MV $8 \times 8 \text{ cm}^2$ MLC water phantom calculation. Collimation is provided up to $20 \times 20 \text{ cm}^2$ by the collimator jaws, with the MLC leaves further collimating the beam to a $8 \times 8 \text{ cm}^2$ square field. (**Top**) Reference distribution (SWT model). (**Bottom**) Dose difference.

After consideration of the figures presented in the preceding pages, these observations can be made for the 6 MV beam model:

- In all cases, beam penumbrae represent regions of disagreement between the two models. This is due to differences in modeled source size and flattening filter scatter component. The ICP beam model presents a slightly larger field size in the inplane direction. The crossplane profile is slightly off-center with respect to the clincal beam model. This is most likely due to an issue where beam profiles are sometimes calculated to be off-center by Pinnacle³ version 9.0 [47].
- Differences in the way the flattening filter is modeled (specifically, in the fluence profile and in the off-axis softening model parameters) are evident upon examination of figure 4–14. Concentric rings of differing agreement between the two models are visible.
- Differences of a magnitude as large as in the case of beam penumbrae or larger are visible at the surface, corresponding to the buildup region of the PDD, as evident from figures 4–15 and 4–16.
- X and Y jaw transmissions are higher in the ICP open beam model than the clinical open beam model and the reverse is true for the wedged beam models. This is demonstrated by figures 4–15, 4–16 and 4–17.
- Finally, it seems from figure 4–17 that inter-leaf transmission is slightly lower in the ICP beam model than it is in the clinical model, although they both have the same value for the "additional interleaf leakage transmission" parameter of the beam model: 0.03. It is therefore probable that the combination of differences in other beam model parameters yields this difference.

18 MV Water Phantom Dose Difference Results

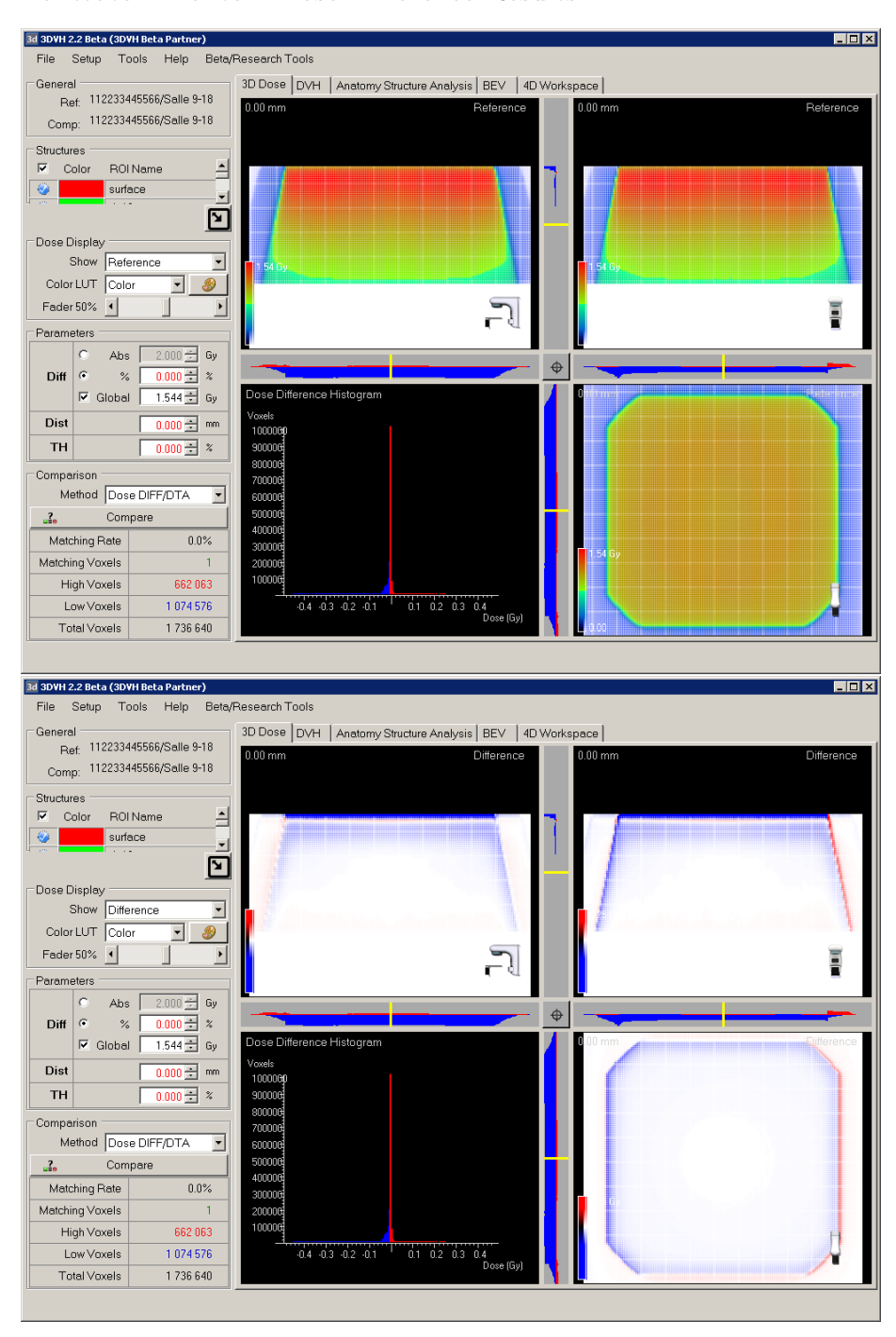


Figure 4–18: 18 MV $40 \times 40 \text{ cm}^2$ open water phantom calculation. (**Top**) Reference distribution (SWT model). (**Bottom**) Dose difference.

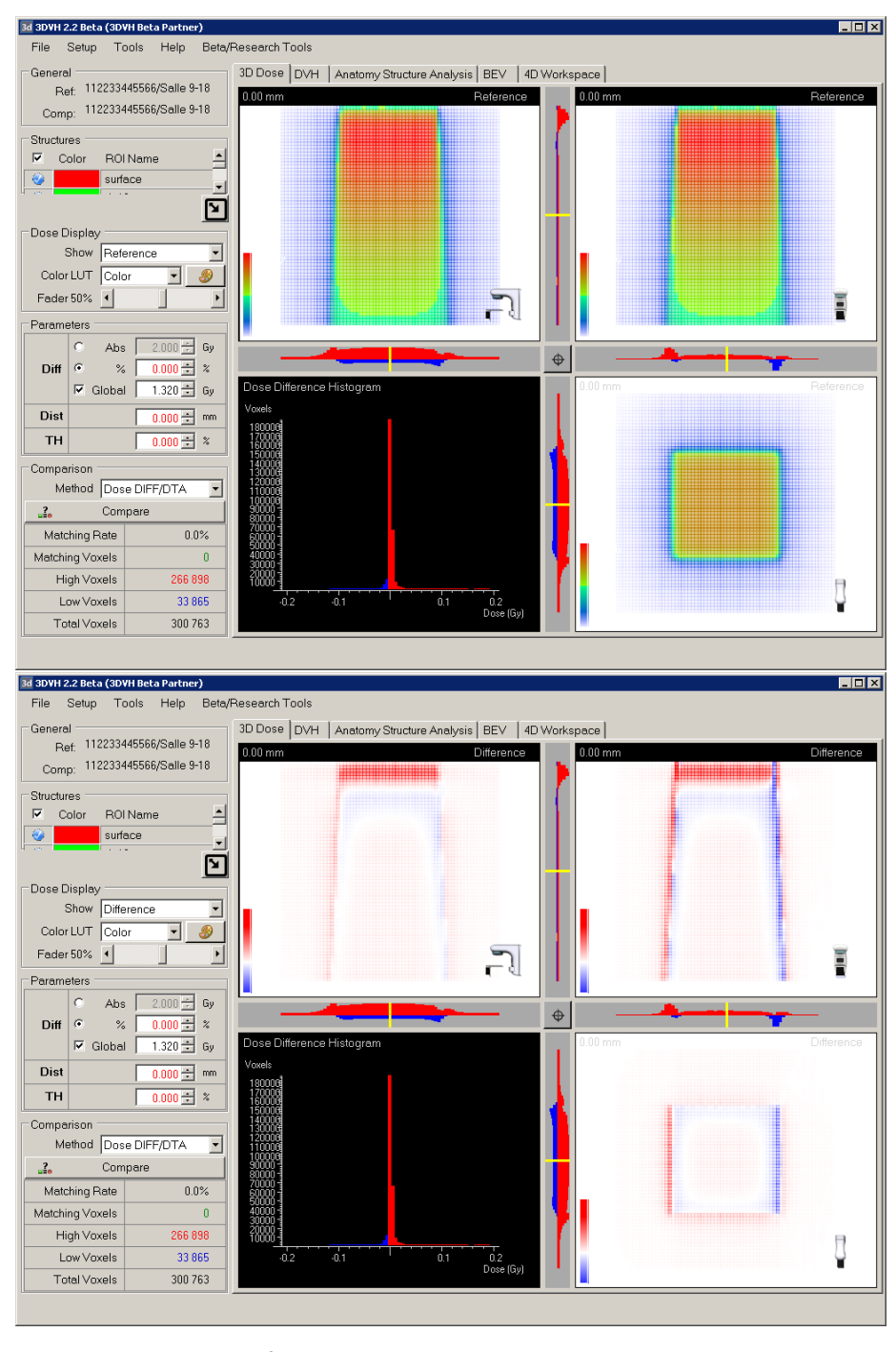


Figure 4–19: 18 MV $10 \times 10 \text{ cm}^2$ open water phantom calculation. (**Top**) Reference distribution (SWT model). (**Bottom**) Dose difference.

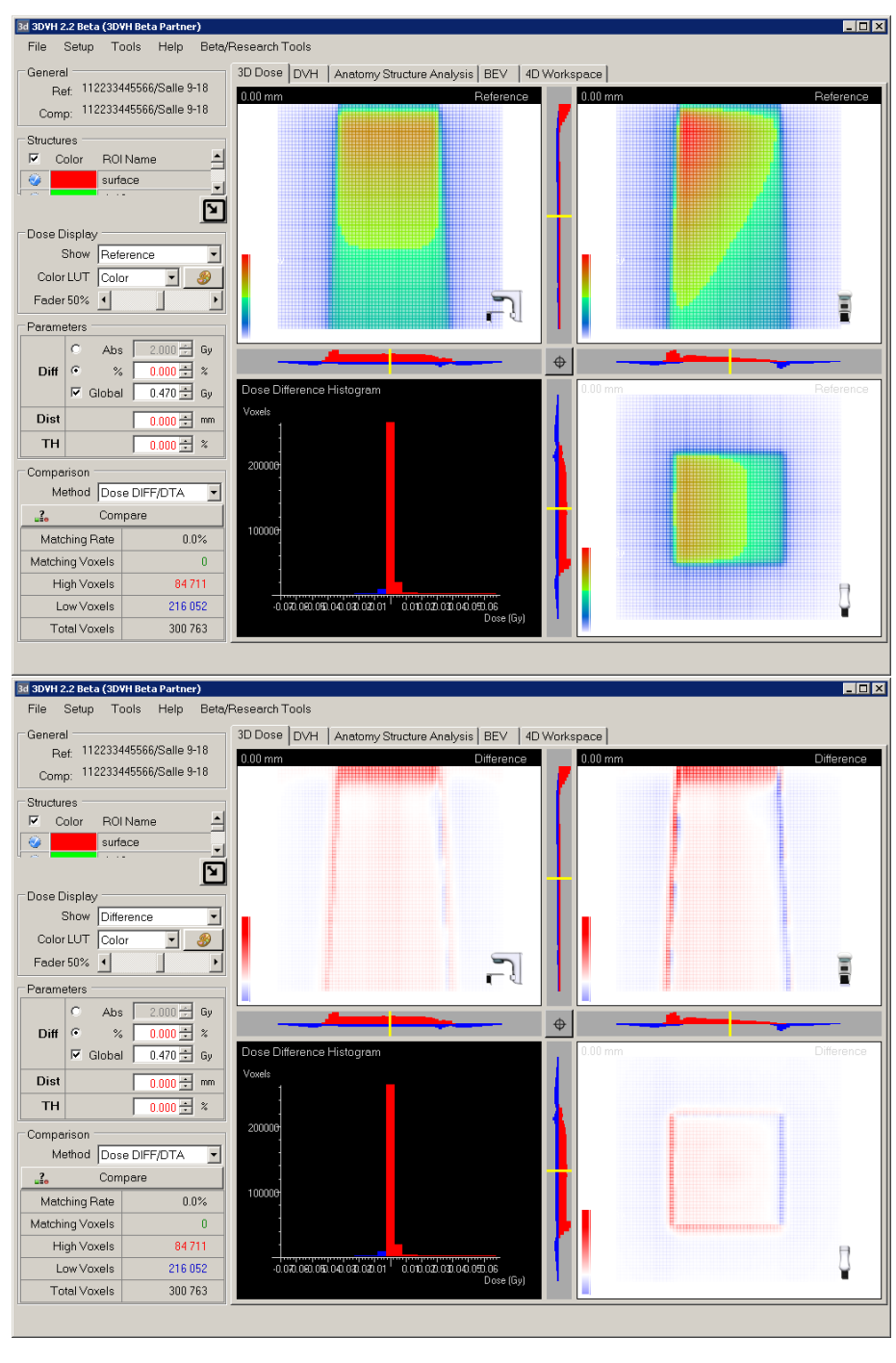


Figure 4–20: 18 MV 10×10 cm² wedged water phantom calculation. (**Top**) Reference distribution (SWT model). (**Bottom**) Dose difference.

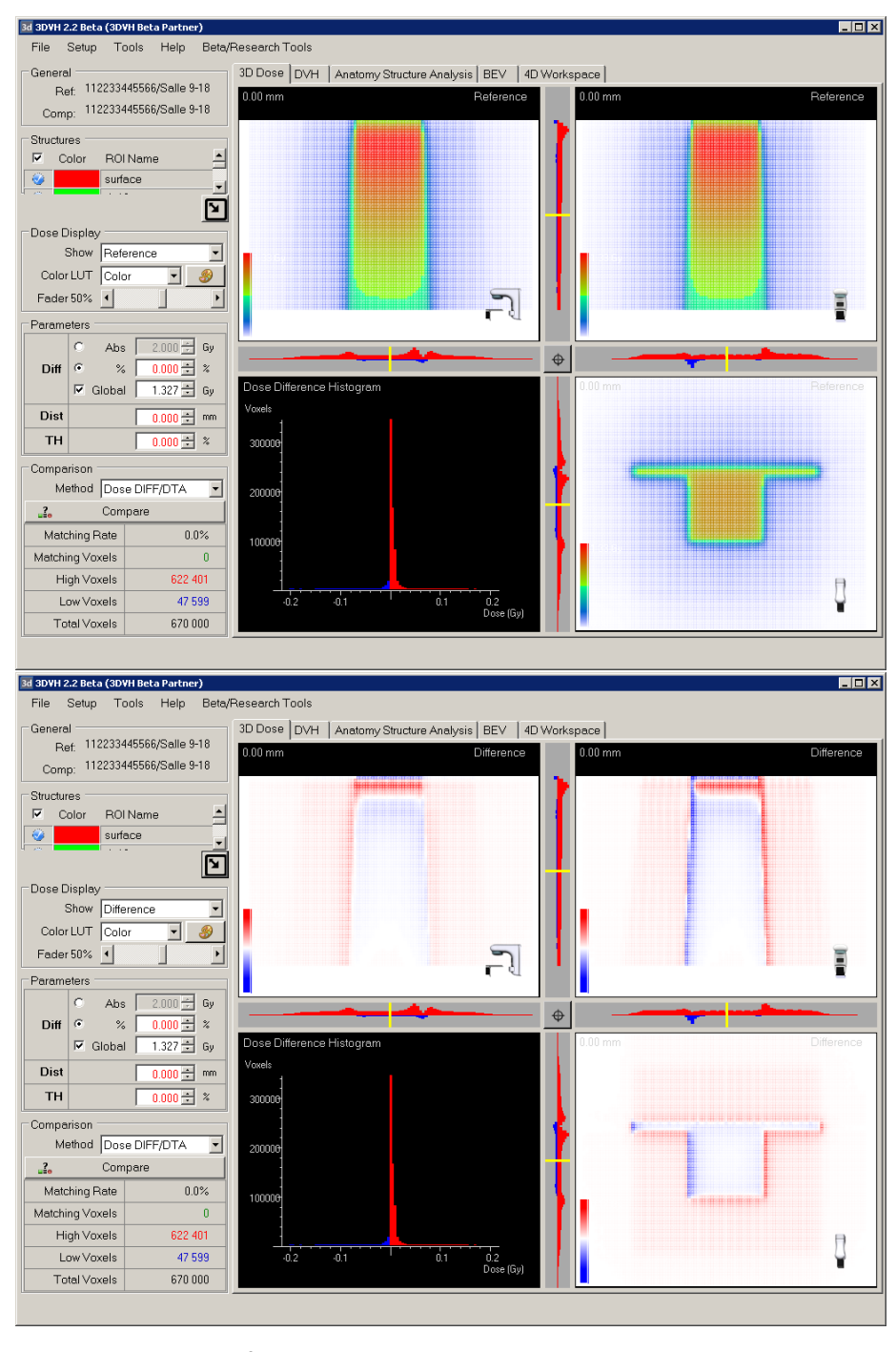


Figure 4–21: 18 MV $8 \times 8 \text{ cm}^2$ MLC water phantom calculation. Collimation is provided up to $20 \times 20 \text{ cm}^2$ by the collimator jaws, with the MLC leaves further collimating the beam to a $8 \times 8 \text{ cm}^2$ square field. (**Top**) Reference distribution (SWT model). (**Bottom**) Dose difference.

The dose differences computed for the 18 MV beam models lead to the following observations:

- There are important differences in the buildup region of the PDD and near the dose maximum. For large fields, the ICP beam model underestimated doses in the buildup region, while there usually is an over estimation for a short distance after the dose maximum (as visible in figure 4–18, very near the surface of the water phantom). The differences are minor at greater depths.
- Penumbrae continue to represent an area of disagreement, although the discrepancies are less pronounced than for the 6 MV models.
- Open beam jaw transmission is almost identical between the two models, as can be seen from figure 4–19. Wedge beam jaw transmission is slightly lower for the ICP model, as evident from 4–20.
- MLC transmission is obviously higher in the ICP beam model than in the clinical model, as seen from figure 4–21.
- Overall, it is visibly apparent that the 18 MV ICP beam model is in better agreement with
 the 18 MV clinical model than is the case for the 6 MV ICP model with the 6 MV clinical
 model. One area where the 6 MV models agree better than the 18 MV models is the buildup
 region of the PDD.

Finally, please note that these interpretations of dose differences can be the result of the combined effect of differences in many beam model parameters. For instance, dose differences that are seemingly due to differences in jaw transmission can result from differences in the jaw transmission parameter itself, but also from differences in modeled beam spectrums, which affect the spectrum of the transmitted beam.

4.7.2 Calculated Dose Distributions of Treatment Plans

In this section, comparisons of treatment plan dose distributions are made, one distribution being calculated with the ICP beam model and the other with the clinical beam model. As discussed in chapter 3, the gamma dose distribution comparison tool is used to find voxels where the distributions are in disagreement or in agreement, within the chosen tolerances of 2 %, 3 mm. 2 %, 0 mm was used in cases where 2 %, 3 mm did not provide useful information on the differences between the beam models.

The studied treatment plans were chosen at random as long as they were originally planned for the same linac as used in this project and that they included 6 MV and/or 18 MV beams. The plans are:

Breast Case This treatment plan is not the most common when it comes to breast treatments, as is includes two tangent 18 MV beams as boost to the 6 MV beams first used. However, it has the advantage of using both the 6 MV and the 18 MV beam models. 82.6 % of the delivered MUs were at 6 MV with the rest being delivered at 18 MV. The prescription was of 45 Gy in 20 fractions at the 100 % isodose line and the global maximum inside the PTV was at 48.4 Gy.

Prostate Case This plan uses 18 MV beams only, with a first prescription consisting of a simple 4-field box 2 Gy per fraction for 26 fractions, then followed by another 6-field prescription at 2 Gy per fraction for 12 fractions, for a total of 76 Gy at the 100 % isodose line. The global maximum inside the PTV was of 76.3 Gy.

Head & Neck Case This plan is for an IMRT step-and-shoot treatment of a neck tumor. A total of 7 beams are used with approximately 6 step-and-shoot segments for each field. The prescription was 70 Gy in 33 fractions to the 100 % isodose line and the global maximum inside the PTV was of 75.4 Gy.

Breast Case: 6 MV and 18 MV

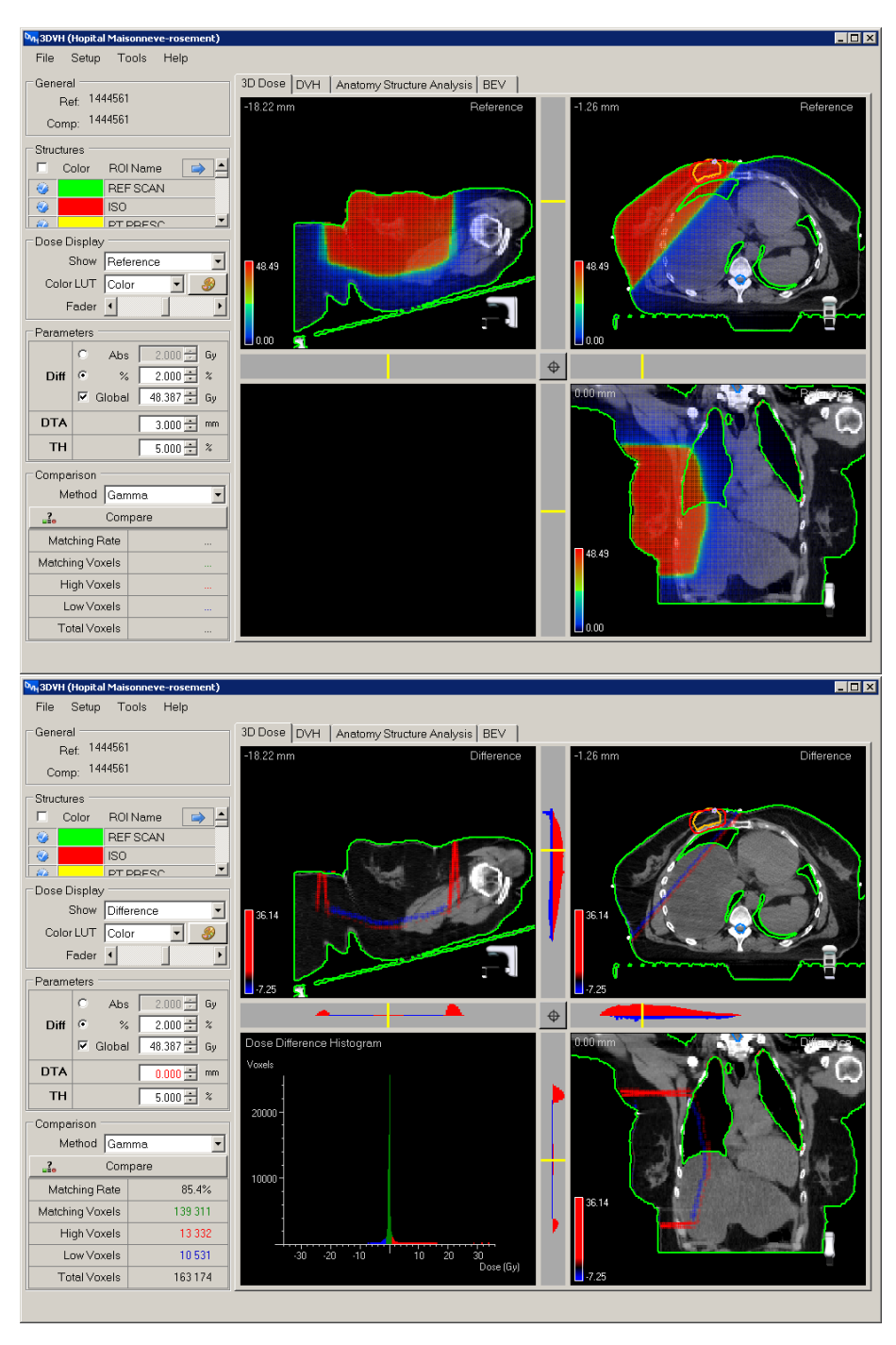


Figure 4–22: 6 MV and 18 MV forward IMRT breast treatment plan dose comparison. (**Top**) Reference distribution (SWT model). (**Bottom**) 2 %, 0 mm γ comparison.

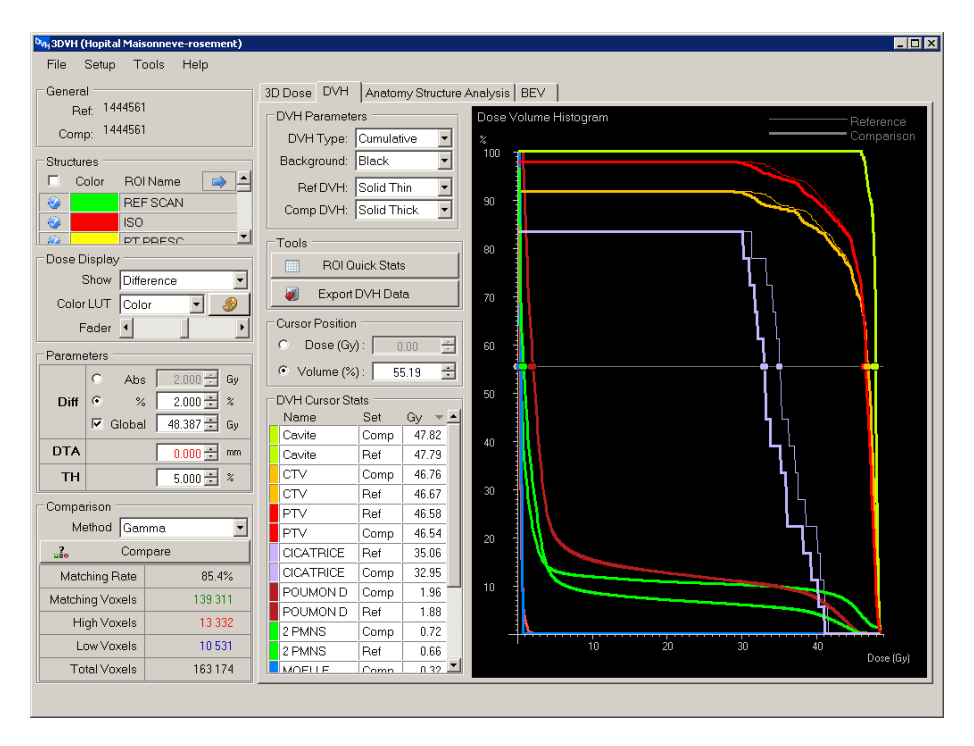


Figure 4–23: DVH comparison for the 6 MV and 18 MV breast treatment plan.

In the case of this mixed 6 MV and 18 MV breast treatment plan, presented in figure 4–22, dose differences for the 2 %, 3 mm were minimal, so the original tolerances had to be tightened to 2 %, 0 mm, effectively turning off the distance-to-agreement component of the gamma comparison. The result is that clearly the penumbrae are the main area of disagreement between the two models. Upon activating the 3 mm distance-to-agreement criterion, the voxels are in agreement. This is not surprising considering that: 1. for a given field size setting at the isocenter, the field size of the modeled beam profile are less than 3 mm apart between the two models; 2. the same measured output factors were used in the two models. The comparison of DVHs presented in figure 4–23 shows no clinically significant differences except in one volume: the scar tissue from a previous operation the patient had. This contour being quite small in volume and being located on the surface makes it very susceptible to differences in the two models, especially in the buildup region of the PDD. The maximum dose to the PTV was 48.5 Gy for the ICP beam model and 48.4 Gy for the clinical model, an insignificant difference.

Prostate Case: 18 MV 4 fields + 6 fields

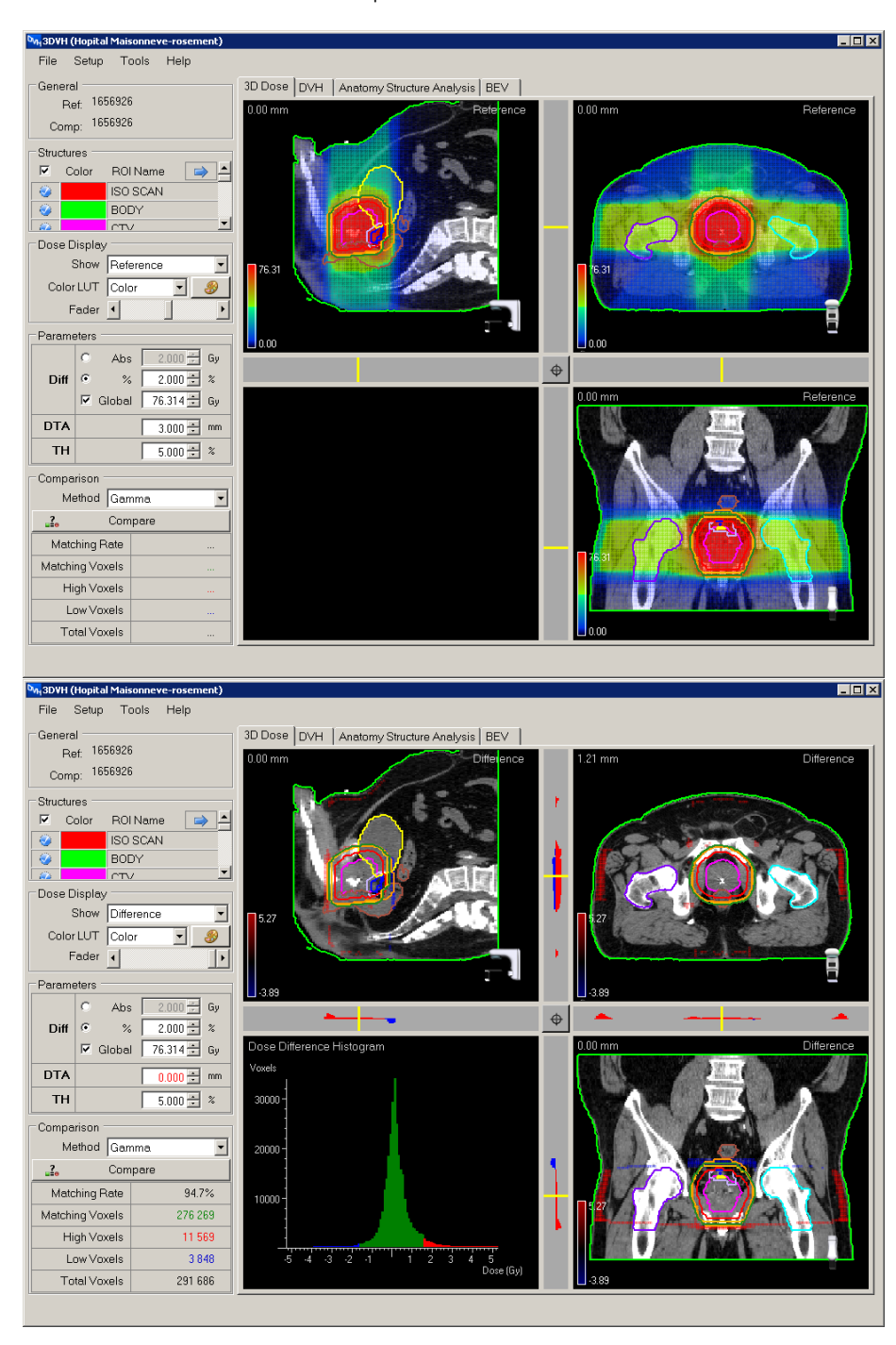


Figure 4–24: 18 MV, 4 fields then 6 fields prostate treatment plan dose comparison. (**Top**) Reference distribution (SWT model). (**Bottom**) 2 %, 0 mm γ comparison.

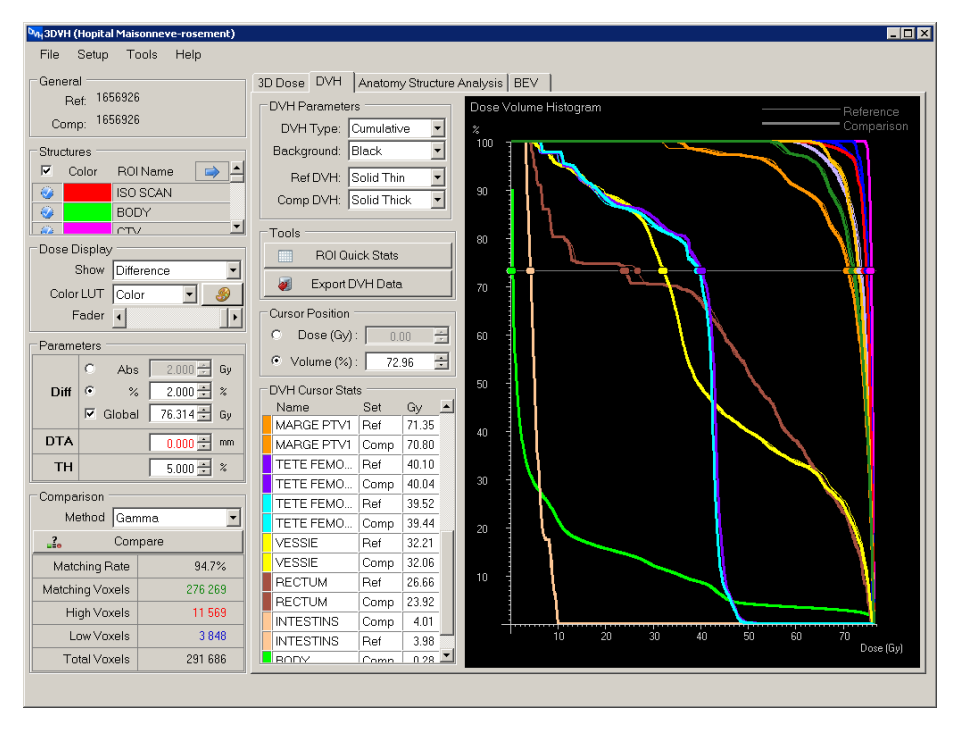


Figure 4–25: DVH comparison for the 18 MV prostate treatment plan.

The same can be said of the 18 MV prostate treatment plan dose comparison presented in figure 4–24 than in the breast case just presented, only now many buildup region voxels are in disagreement between the two models. In the breast case, most planned MUs were from the 6 MV beam, for which, as shown earlier, the beam model better reproduces SWT measurements for PDDs than the 18 MV model does, in the buildup region. The fact that the prostate case is treated with only 18 MV beams means that errors in the buildup region from every beam in the plan can accumulate, producing significant differences at beam entries.

The maximum dose to the PTV was 76.3 Gy in both beam models. Other than in the beam entry areas and the beam penumbrae, the most significant difference exists for the $\approx 70 \%$ to $\approx 73 \%$ volume range of the DVH for the rectum. A difference of ≈ 2.7 Gy exists between the two models for that volume proportion near the 25 Gy level. Depending on the criterion used for this OAR, it could be clinically significant. In our clinic, however, the criterion are specified for the 60 Gy

(<50~%), 65 Gy (<35~%), 70 Gy (<20~%) and 75 Gy (<15~%) levels. Thus, as it stands, from the DVH point-of-view, the two plans would be clinically equivalent.

Head & Neck IMRT Case: 6 MV

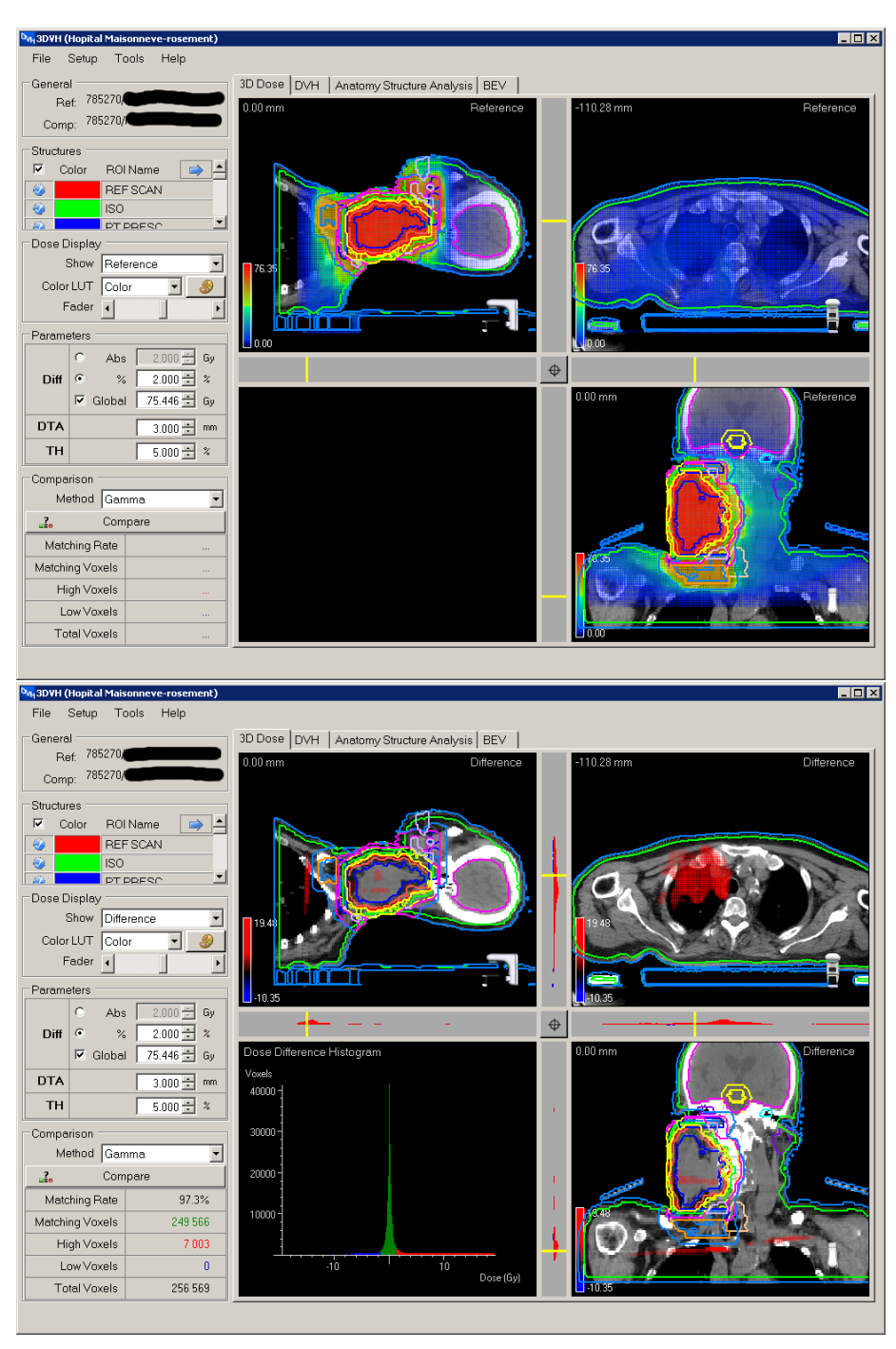


Figure 4–26: 6 MV head & neck IMRT treatment plan dose comparison. (**Top**) Reference distribution (SWT model). (**Bottom**) 2 %, 3 mm γ comparison.

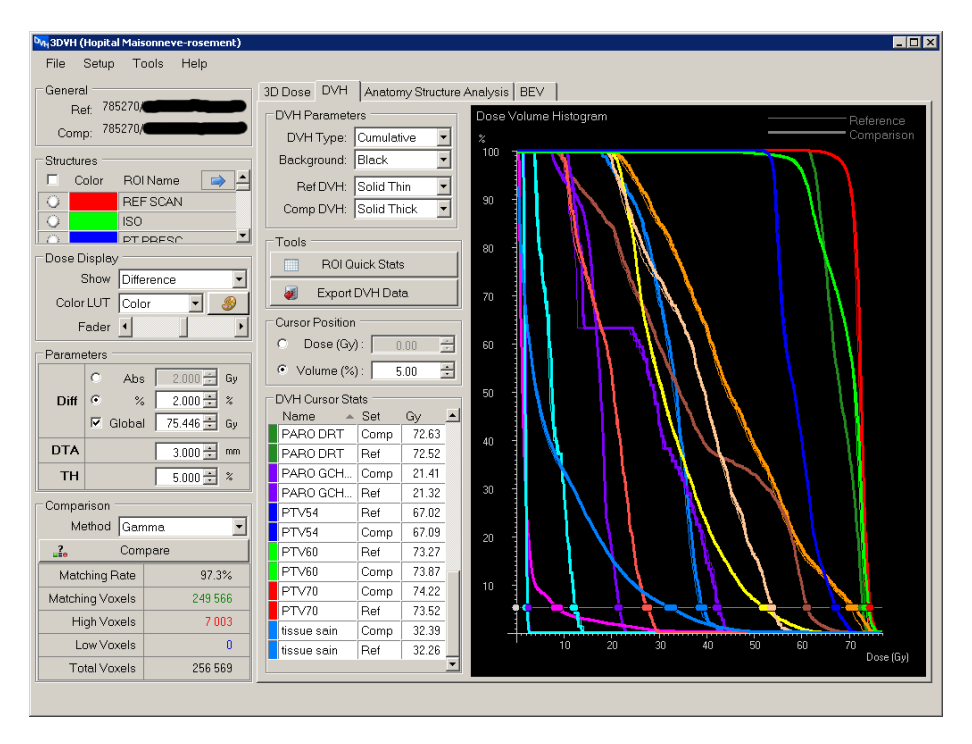


Figure 4–27: DVH comparison for the 6 MV head & neck treatment plan.

This head & neck case, shown in figure 4–26, demonstrates that important dose differences can occur when comparing the two models in an IMRT plan using 6 MV. This plan used a total of 7 beams with approximately 6 step-and-shoot segments each. With so many separate irradiations, small discrepancies in the two models can amount to large differences in the final calculated dose distributions.

In this case, significant differences, of the order of up to 20 Gy (about 27 % of the global maximum dose), are visible in the inferior side of the patient, where a low dose, low dose-gradient region exists. The apparently higher MLC and jaw transmission found in the ICP model may be responsible for this, since fields used in this plan are fairly small (highly collimated) and the number of MUs is superior to a typical 3DCRT plan.

Additionally, there are voxels located in the PTV that fail the gamma comparison. These voxels have a dose difference of up to +2 Gy (≈ 3 % of the global maximum). Thus, figure 4–27 shows that the maximum dose predicted by both models is different in the PTV (the actual difference is

of 1 Gy: 76.4 Gy for the ICP model and 75.4 Gy for the SWT model). This could potentially lead to different decisions being made by the treatment planner with regards to the maximum dose in the PTV and its deviation from the prescription dose.

Even if a larger data set of comparisons should be compiled to conclude definitely on IMRT plans in general, the differences observed for this plan are sufficient to state that dose differences between the two models could change the plan optimization in a clinically significant manner.

4.8 Acquisition Speed

A single photon beam energy beam data set, omitting MLC fields, was acquired in 6 hours. This was using 40 MUs for every irradiation and yielded 26 RDFs, 26 PDDs and 256 profiles (although the RDFs disagreed very much with accepted values). In terms of IC PROFILERTM measurements only, 1056 were made in those 6 hours for an average of 2.93 measurements per minute. The time includes time alloted for setting up and putting away equipment and time used to enter the linac room to change the thickness of the solid phantom and re-adjust SSD.

Comparing to a SWT system, it would mean averaging one complete scan every 77 seconds, including the tank set-up time and time alloted to put away equipment. If we include point measurements (RDFs) as well as scan measurements (PDDs and OARs), it would mean a rate of one measurement per 72 seconds must be achieved with the SWT, which corresponds to making 50 measurements per hour. This indicates that the developed acquisition method allows the acquisition of the necessary measurements dramatically faster than with a SWT.

If both beam energies are measured using the same step-and-shoot sequence, the number of entries into the linac room to change depth remains the same and this really represents the most time-consuming part of the ICP beam acquisition process. It is estimated that doing so would allow both beam energies to be measured in 10 hours. A further 3.5 hours are needed to acquire MLC field data (for both energies at once), making a total of 13.5 hours. (The reason MLC fields must be measured separately from standard fields is that the ICP needs to be centered off the beam central axis by 0.5 cm on the Elekta Synergy® linac for the detectors not to fall under an inter-leaf area.)

This is for a total of 632 measurements (i.e. scans with a SWT). Again, with this estimate, we are averaging a rate of 77 seconds per scan.

It seems that, in order to increase acquisition speed, one has to further decrease the number of MUs delivered for each field. This presents diminishing returns, however, because the limiting factor is the number of times one must enter the linac room to change buildup thickness over the ICP and adjust SSD. This amount of entries into the treatment room remains constant and cannot be decreased unless the user chooses to measure PDD at fewer depths (yielding fewer points for the PDD fitting function), which would further degrade the quality of measured PDDs.

It is obvious that, if only measuring profiles (and not depth dose curves), the IC PROFILERTM data acquisition method presented in this work is *much* faster than using a scanning water tank system. As evident from the results presented in this chapter, this gain in acquisition speed comes at a cost in precision and accuracy, when comparing to SWT measurements.

Chapter 5 Conclusion

5.1 Method

This thesis examined the feasibility of performing a linar beam acquisition using the IC PROFILERTM (Sun Nuclear corporation, Melbourne, FL, USA), an ion chamber array designed for fast beam symmetry and flatness evaluation. It was surmised in at least one publication that the ICP showed potential for this task [15], but results of a beam commissioning with the device were inexistent or unpublished at the time of this writing.

The feasibility was examined by conceiving of a method that allowed the necessary measurements for beam modeling in the Pinnacle³ treatment planning system to be made in an amount of time that compared advantageously to the use of a scanning water tank system. The method was used to acquire beam data and comparisons were made to the best data available: that which was acquired with a SWT and used in the original commissioning of the linac.

Much time and effort was devoted to optimizing this method of beam acquisition, making it faster and closer to reference SWT data as the project advanced. The aspects of measurement setup, necessary software, measurement workflow, array calibration, array acquisition mode (pulsed or continuous), measurement reproducibility and data processing had to be investigated.

Eventually, when the acquisition method was deemed to be optimal, the ICP-acquired data was used as input for the beam modeling process in Pinnacle. When the ICP-acquired data had important differences from SWT data, as in the case of the measured relative dose factors, reference SWT data were used in order to complete the beam model. Evaluation of acquired data with the ICP by direct comparison to SWT data helped identify situations where the ICP underperforms compared to a standard SWT system.

The beam model constructed with the ICP data was shown to fit ICP measurements better than the clinical beam model used for the linac did. This meant that the beam model incorporated the characteristics and particularities of the ICP measurements in a significant manner. Furthermore, it meant that the comparison of this ICP beam model with the clinical SWT-based beam model would lead to a meaningful comparison of the end-result of the two beam data acquisitions.

Comparisons of the two beam models was achieved first by independently comparing them to a set of model validation measurements. Then, calculated 3D dose distributions were compared for some of these validation fields, using per-voxel dose differences. Finally, the calculated dose distributions of three treatment plans were compared using gamma analysis.

5.2 Agreement of ICP Measurements with SWT

The degree of agreement of ICP-acquired data to SWT-acquired data varies greatly depending on the situation. Most beam profiles agree quite well between the two measurement modalities – that is – within acceptable error given our chosen comparison criteria of 2 %, 2 mm gamma.

The PDDs resulting from the ICP acquisition sometimes presented some important differences with SWT data in the buildup region at depths just beyond the depth of maximum dose. Agreement beyond this was generally very good, as the normalization depth for all fractional depth doses (loosely called PDDs here) was 10 cm.

The measurement of relative dose factors with the ICP did not yield satisfactory results, as RDFs for small fields were underestimated compared to SWT measurements. The opposite is true for the largest fields used, where the ICP measurements lead to overestimated RDFs compared to the SWT.

For this reason alone, it is difficult to recommend the ICP as the sole device used for beam acquisition. Combined with another device to better measure PDDs, small field profiles and especially RDFs, it could be used safely, based on direct comparison of the acquired measurements.

5.3 Differences Between the Two Beam Models

Even if relative dose factors used for the ICP beam models were actually the very same factors used as input for the clinical SWT-based beam model, there remained differences between the two beam models. These differences are of course due to the different beam model parameters used in

the two cases, which are a consequence of differences in the measured OARs and PDDs between the two systems.

It is of interest to note that there is a degree of variability associated with the beam modeling process, and that two independent beam modeling tasks performed with the same set of measurements would in all probability not yield the exact same model. Still, the fact that the ICP beam model fits the ICP measurements better than the clinical model does points out that the beam modeling process was successful in incorporating many characteristics of the ICP measurements in the final model.

We may use the calculated dose distribution comparisons presented earlier to evaluate the ICP's ability to acquire data in preparation to beam modeling. For simple plans some significant differences (≈ 4 % global maximum dose in the studied prostate case) can turn up in organs at risk. For IMRT plans it is possible to get even larger differences (≈ 27 % global maximum dose in the studied head & neck case) in low dose, low dose gradient regions. Some differences (≈ 3 % global maximum dose in the studied case) can also occur for the maximum dose in the PTV. Given these facts, it is reasonable to conclude that there exist differences present after beam modeling that could lead to different clinical decisions, as to whether or not a certain plan is usable for treatment.

5.4 Feasibility of Beam Data Acquisition with the IC PROFILERTM

The difficulty in measuring relative dose for small fields because of the fixed, relatively large size of the ionization chambers on the ICP, and the poor results obtained for large fields disqualify this device as a tool to perform a full beam data acquisition. Because of the 0.9 cm inherent buildup to the array, PDD measurements are also difficult, and do not always yield results that compare suitably to reference SWT data.

Measured profiles agree very well with SWT data, but subtle differences in the penumbra and umbra regions might lead to significant differences in source size and collimator/MLC transmission beam model parameters. Some of the differences in the model parameter values are no doubt due only to the variability of the beam modeling process, and the ICP-acquired data should not be

blamed for this. The fact also that field size was slightly adjusted since the original commissioning data was acquired can introduce differences.

All in all, we must come to the conclusion that the IC PROFILERTM is not suitable for performing beam data acquisition that would lead to data importation in a treatment planning system. This is true under the method described in this thesis, a method which includes using a very specific experimental setup and various data processing steps.

Still, it is the author's belief that this work has underlined some important limitations of the ICP in the context of beam commissioning, namely:

- Inability to measure RDFs accurately for the smallest and largest fields.
- Difficulty of acquiring PDD data in the buildup region. This is mainly due to the 0.9 cm inherent buildup used in the ICP's construction.
- Inability to remotely scan the detectors. Scanning laterally the array could mean acquiring data with much higher spatial sampling than the nominal detector spacing of the array. Array centering would also become less of a concern. This could be achieved by coupling the array to a remotely operable linear translation stage, or with timed precise patient couch movements (if the weight of the experimental setup is supported safely by the couch).
- Fairly large ionization chambers are used (≈ 3 × 7 mm²). While the 3 mm dimension of the chamber is placed along the axis of highest expected dose gradient, it remains that this detector size is inappropriate for making measurements in small fields (3 × 3 cm² or lower). Furthermore, a smaller detector volume could potentially allow for a denser packing of the detectors, yielding a smaller detector spacing.
- Limited array length to 32 cm. This imposes an important restriction on the measured field size at the SSD specified by the TPS manufacturer for beam data acquisition, leading to the need for the combination of several measurements to obtain full profiles of large fields.
- A software user interface designed primarily for real-time adjustment of beam flatness and symmetry. The software is currently the only way to operate the IC PROFILERTM, and is geared towards making a few singular measurements, rather than a long series of measurements, as is needed in the case of beam commissioning.

5.5 Outlook

While the IC PROFILERTM did not prove itself to be an appropriate device for beam data acquisition under the chosen method, the results of the method itself did show that acquiring many measurements can be done in a reasonable amount of time. In fact, the acquisition speed approaches 200 ICP measurements per hour, which is easily more than twice what is achievable using the ICP software in its current state (for the number of MUs used and the information recorded for each measurement).

The combination of a pre-determined sequence of measurements, a linac with step-and-shoot capability and the method developed during this project could prove an interesting tool were it used as a quality assurance procedure. A reduced SSD (for instance 75 cm) could be used for all measurements, making even the largest field fit over the surface of the ICP and eliminating the need for profile combination. Fewer points could be acquired for the PDD measurements and the optimal values of the fit parameters could be used to characterize beam quality.

Thus, with a much-reduced total number of measurements, the total time required to acquire a full set of measurements for a single energy could be much shorter (always depending of what the user actually chooses to acquire). This pseudo-acquisition set could be used as a baseline for the beam characteristics, to be taken right after reference SWT data is acquired. Another possible application would be beam matching, where one wants to determine if one machine's beam characteristics match that of another machine.

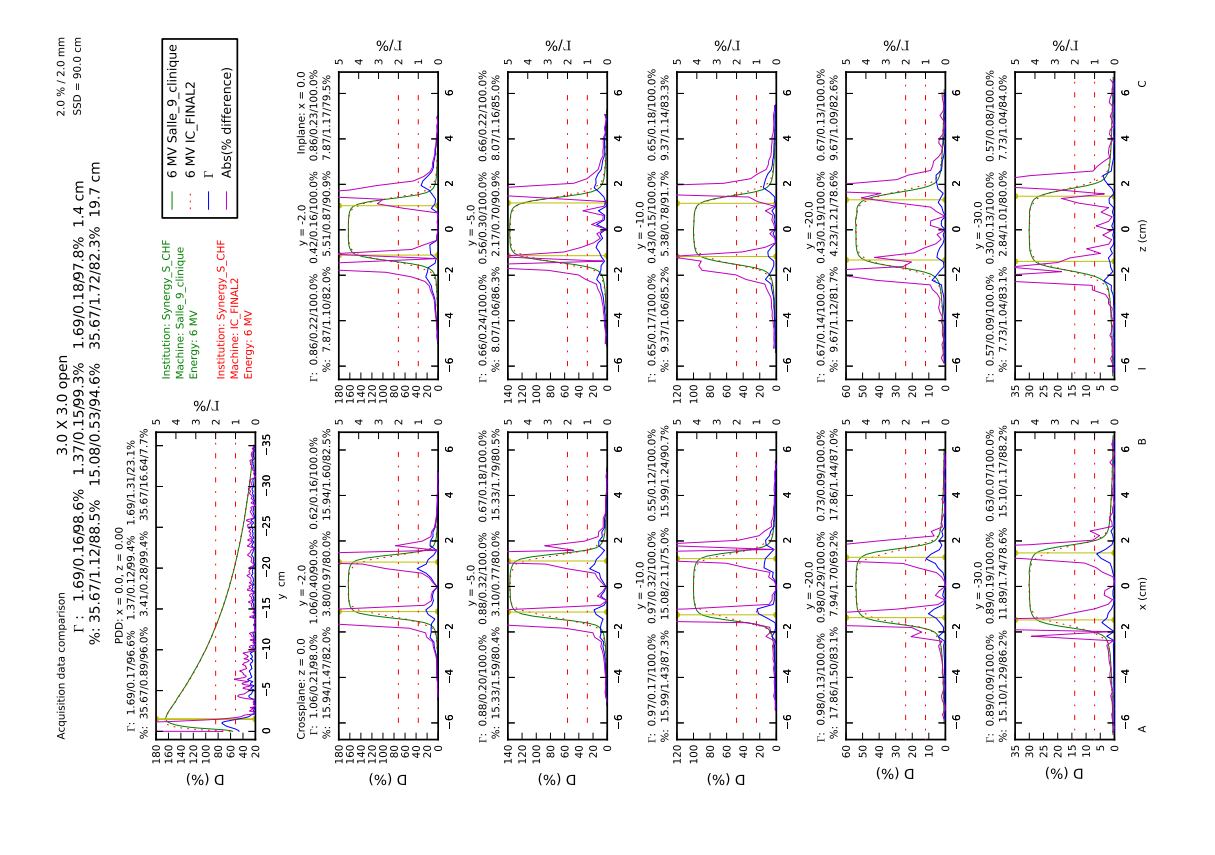
During this project, some effort was devoted to eliminating the blurring effect of the ICP's relatively large chambers on radiation profiles by the way of deconvolution. It was attempted to calculate the ICP's pulse response function with a Monte Carlo simulation and then to use that response to recover "true profiles". It was also attempted to determine why the ICP's measured output factors at 6 MV were so different from the SWT's measurements for large fields by way of Monte Carlo calculations. A fairly complete and accurate model of the panel was thus created using egs++ Monte Carlo package [48] and is available. These aspects of the work were not finished due to time constraints. However, should anyone want to pursue the project further, there is basis for continuation.

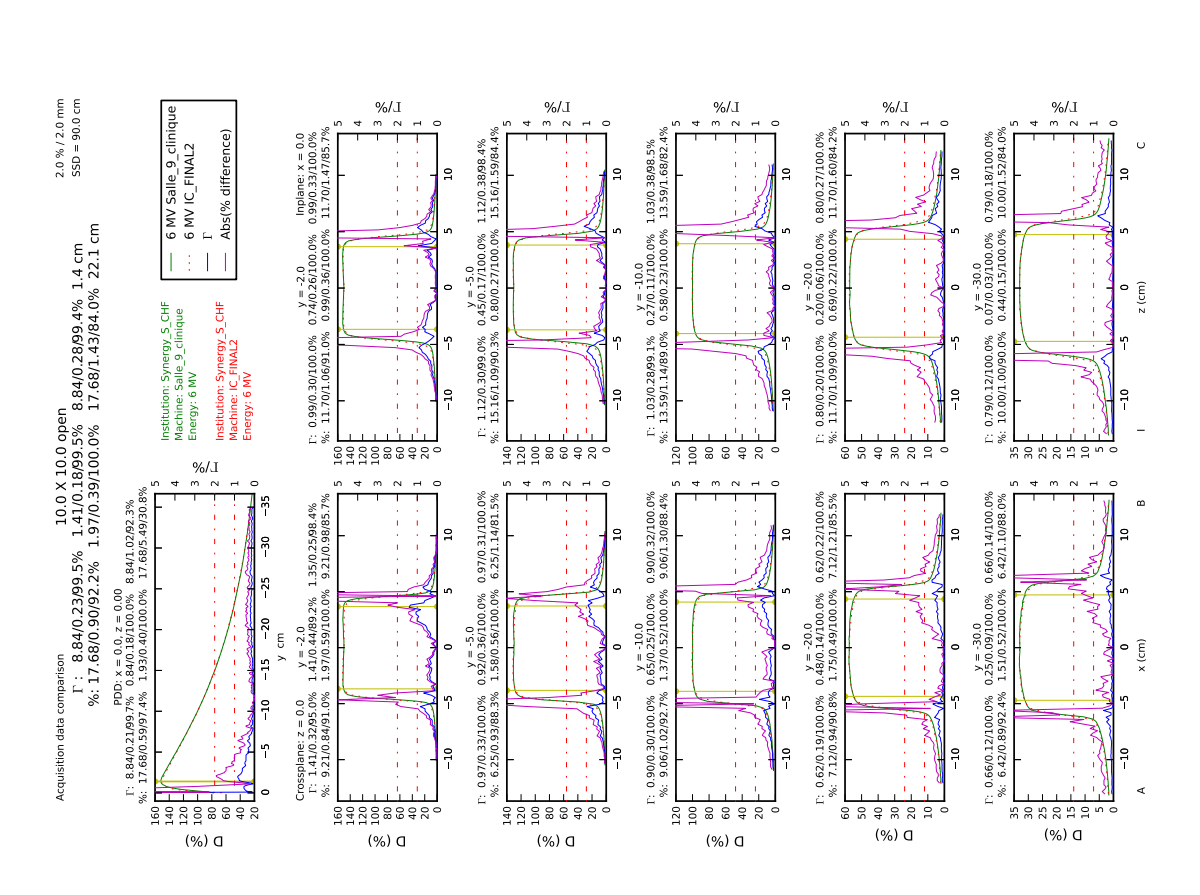
Finally, it should be mentioned that in general, there is an important lack of published studies regarding the use of detector arrays for the purpose of beam commissioning. For example, there exists a commercial product from IBA Dosimetry, the linear diode array LDA-99 (IBA Dosimetry GmbH, Schwarzenbruck, Germany), which can interface with IBA's Blue Phantom scanning water tank system. The array is interesting because it can be submerged in water and scanned in all necessary axes. Yet, there are, at the time of this writing, no published articles evaluating it.

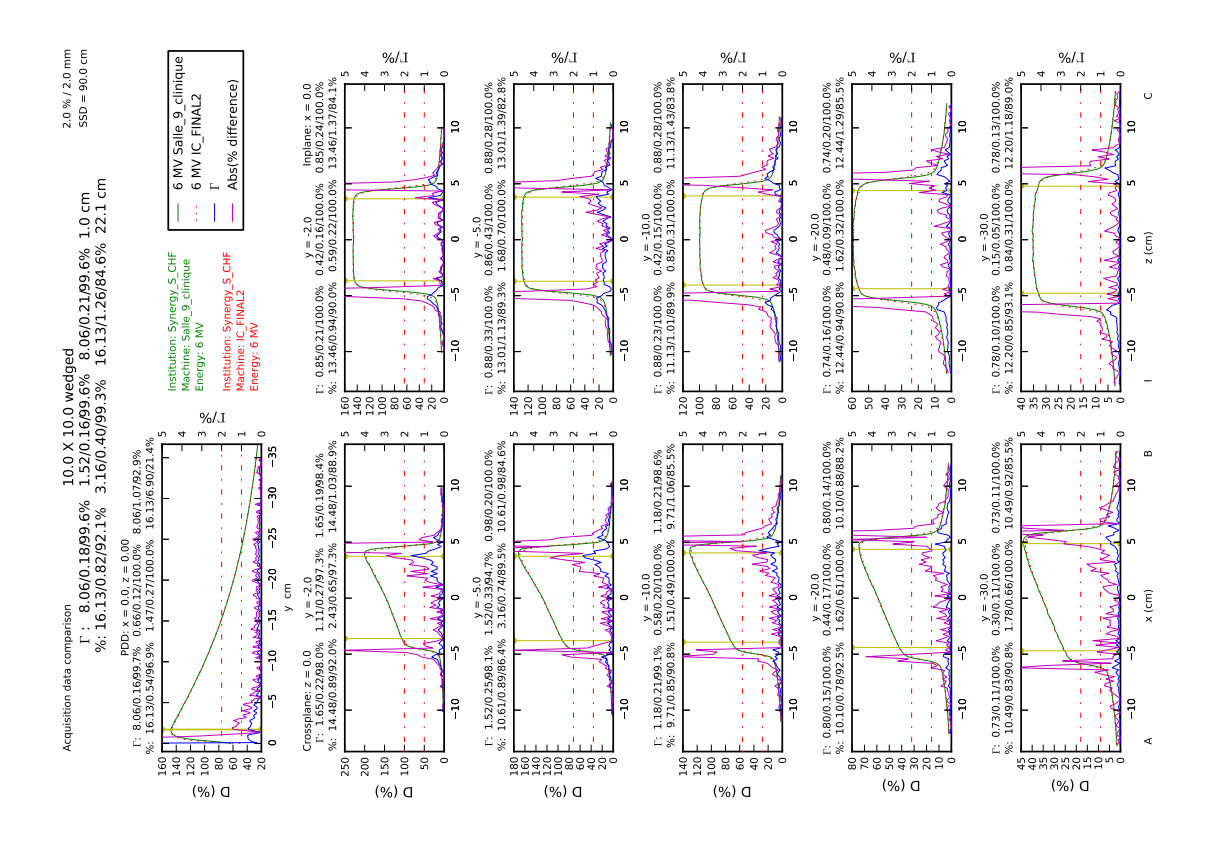
Arrays or matrices of water-equivalent detectors, such as scintillating fibers, could also be of great interest in the context of beam commissioning. Yet, publications regarding this technology focus mostly on other applications, such as quality assurance or portal imaging. It is therefore desirable that more studies regarding the use of arrays in beam data acquisition be performed, not only because using an array may save a great deal of time to physicists performing a beam commissioning task, but also to realize its other advantages, its limitations and what measurements it can safely acquire.

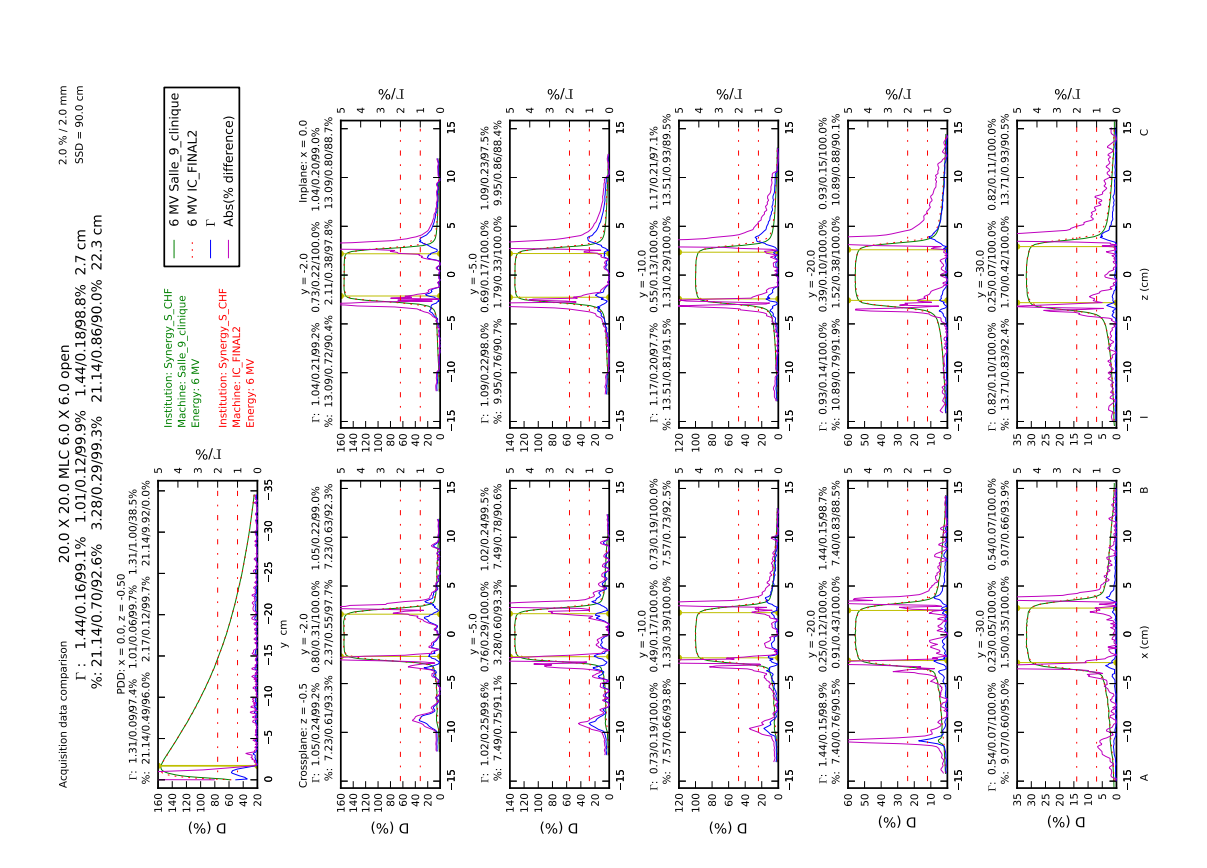
Appendix A

$6~\mathrm{MV}~\mathrm{SWT}$ vs ICP Acquisitions Comparison



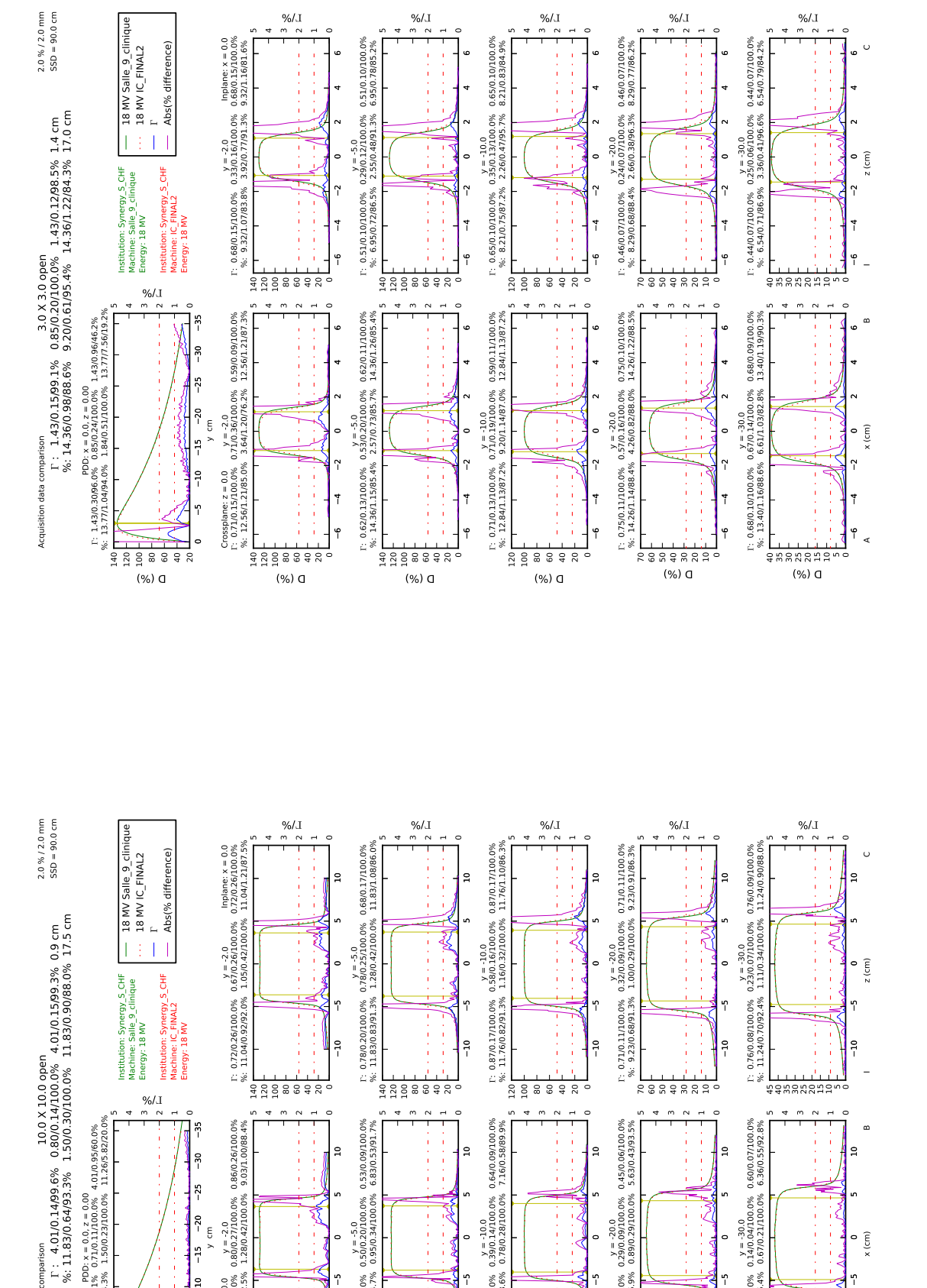






Appendix B

$18~\mathrm{MV}~\mathrm{SWT}$ vs ICP Acquisitions Comparison



2

-10

140 1120 100 80 80 60 40

(%) ₫

Crossplane: z = 0.0 y = -2.0 T: 0.86/0.26/100.0% 0.86/0.27/100.0% 0.86/0.26/100.0% %: 9.03/0.79/92.5% 1.28/0.42/100.0% 9.03/1.00/88.4%

e e

, -20 y cm

-15

유

140 120 100 80 60 40

(%) ₫

120 100 80 80 60 60 20

(%) a

2

-10

140 1120 1100 80 60 60 40

(%) ₫

y = -20.0: 0.45/0.07/100.0% 0.29/0.09/100.0% 0.45/0.06/100.0% %: 5.63/0.38/95.9% 0.89/0.29/100.0% 5.63/0.43/93.5%

9

45 30 30 10 10

(%) ₫

9

0 × (cm)

9

9

(%) ☐

L/%

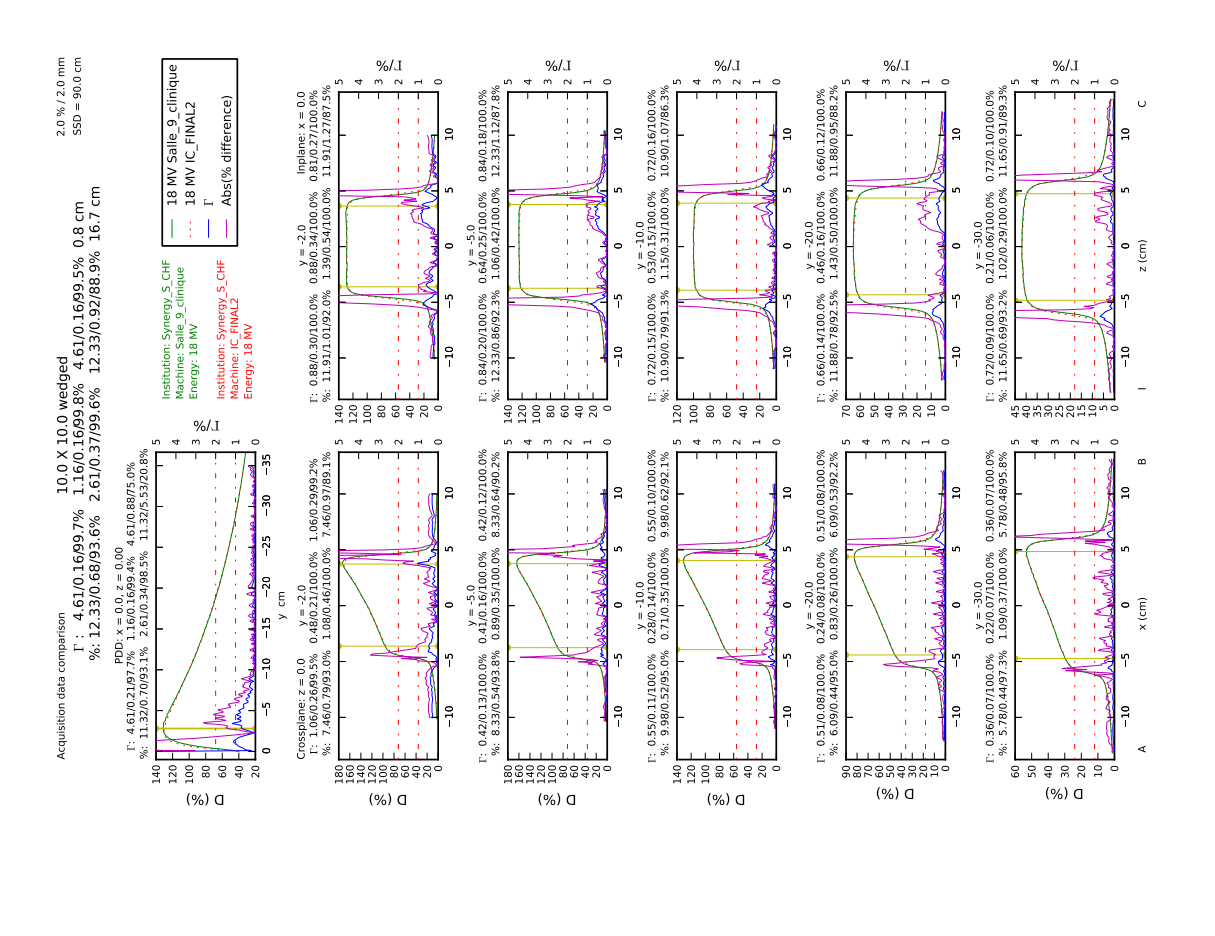
L\%

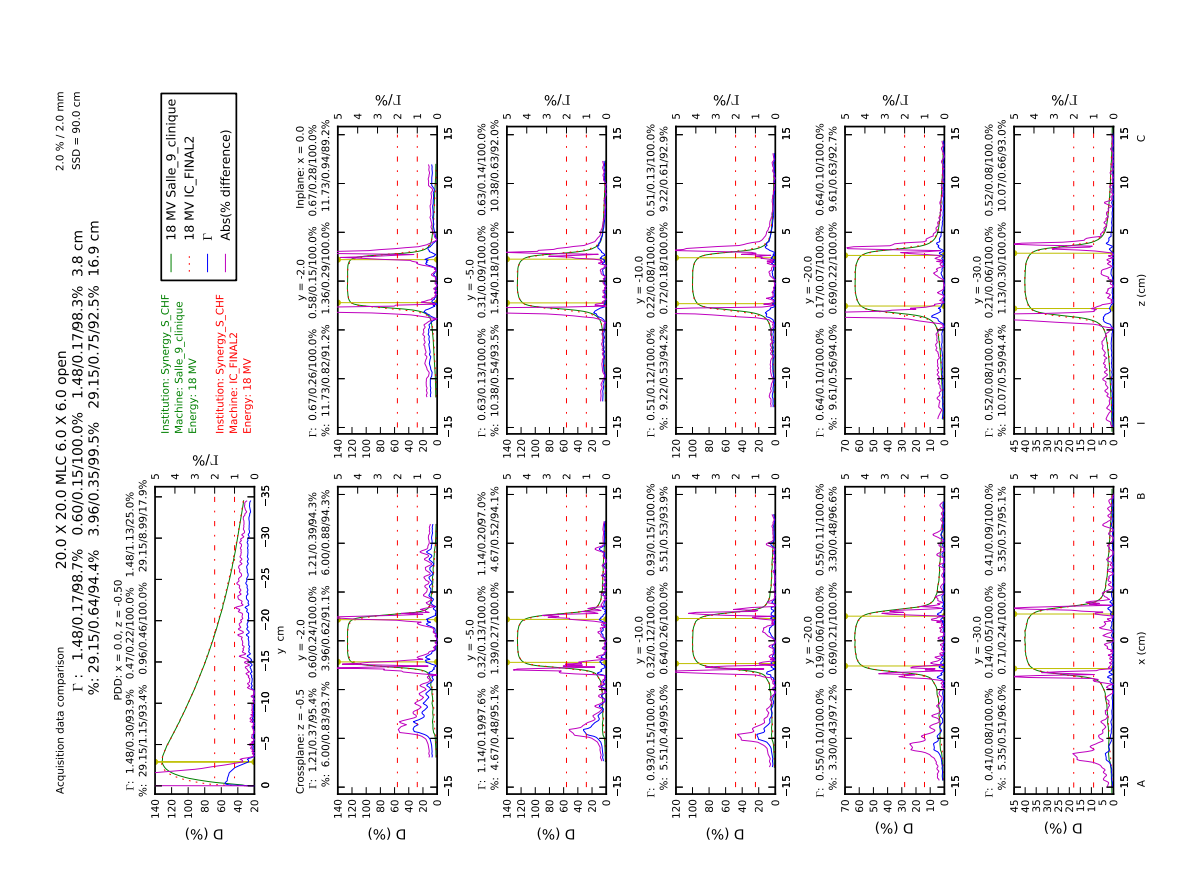
L/%

L/%

PDD: x = 0.0, z = 0.00 I: 4.01/0.17/97.1% 0.71/0.11/100.0% 4.01/0.95/60.0% %: 11.26/0.63/94.3% 1.50/0.23/100.0% 11.26/5.82/20.0%

Acquisition data comparison

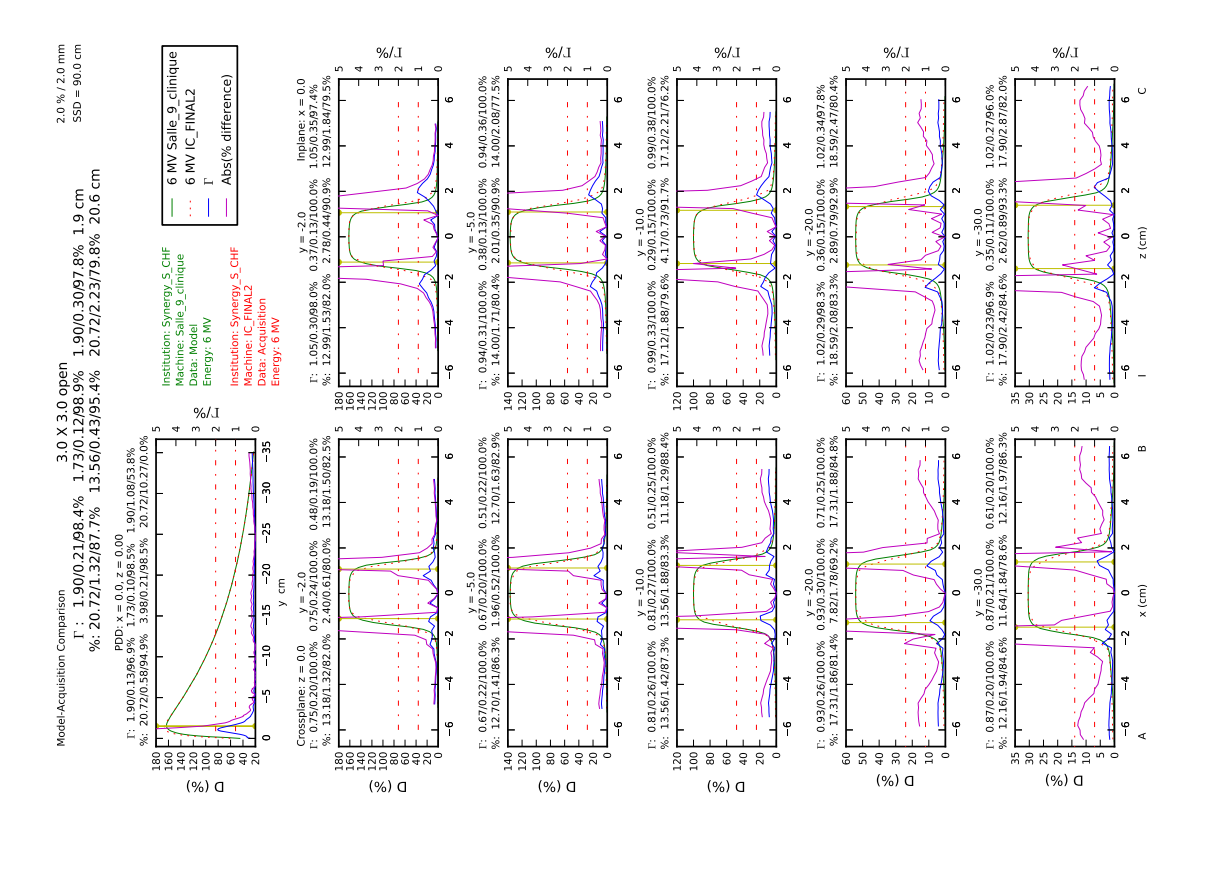


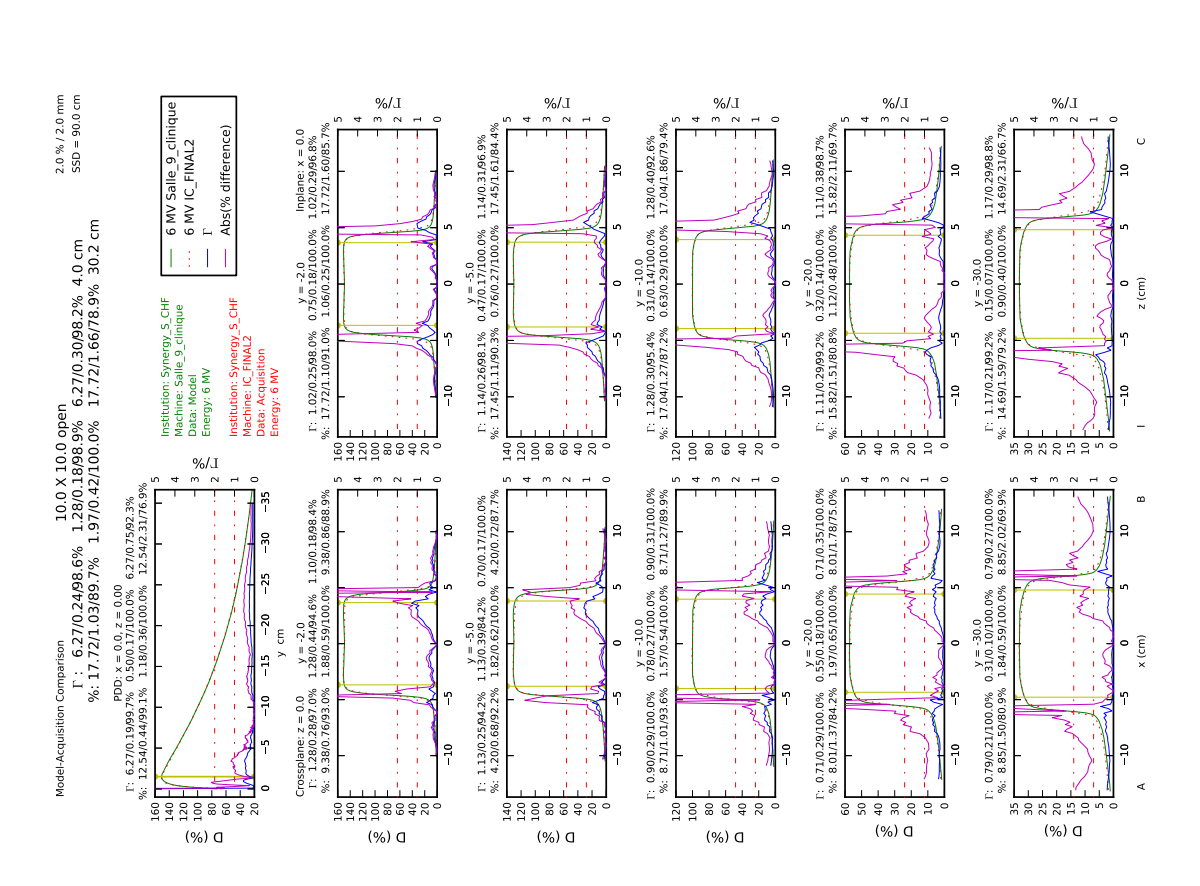


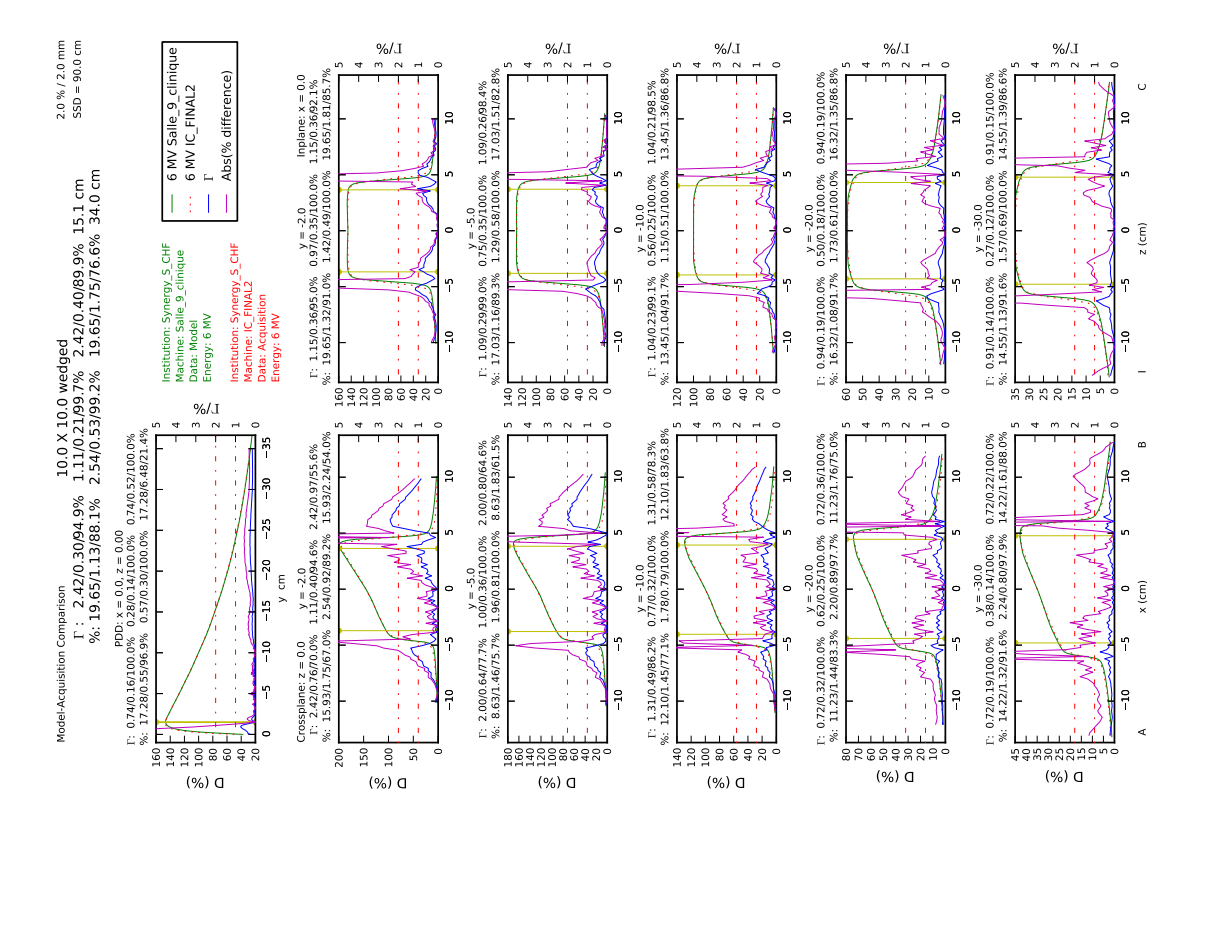
Appendix C

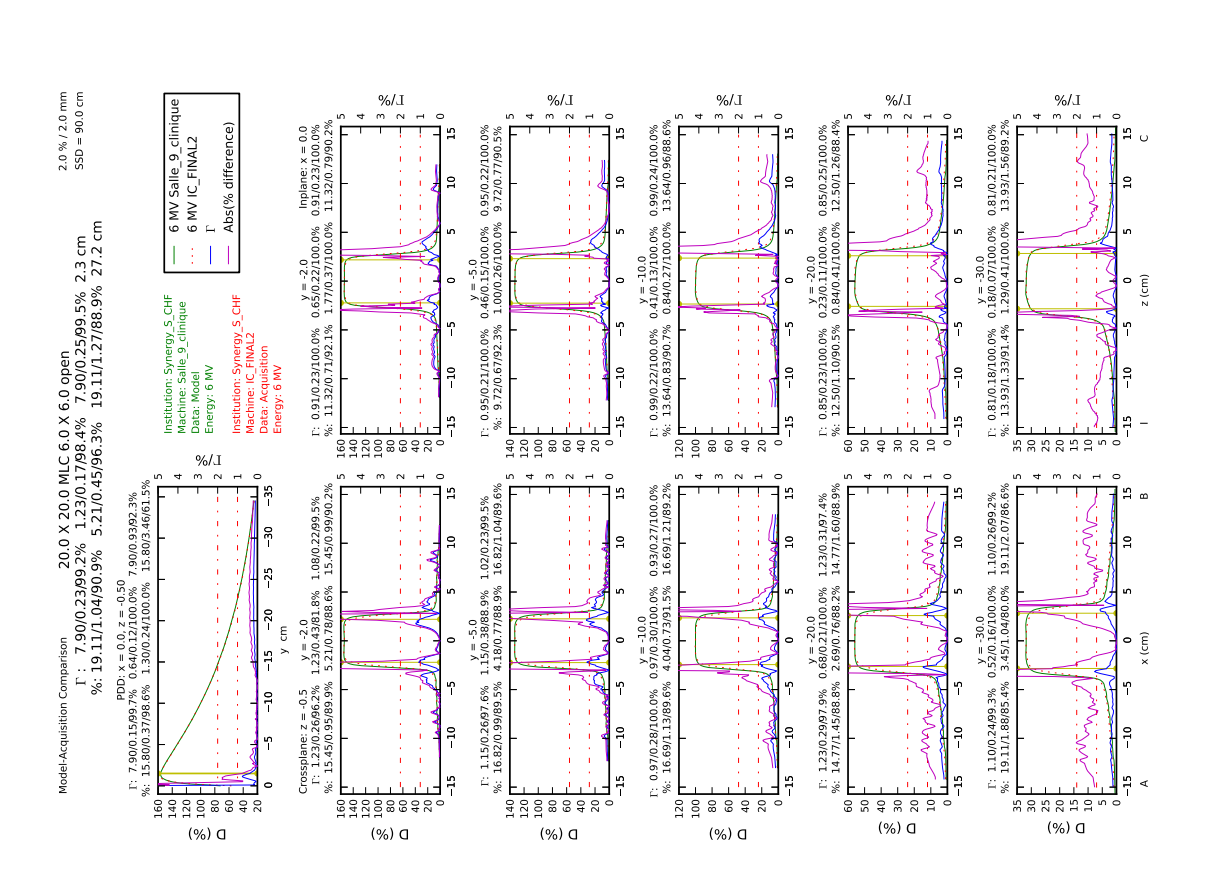
$6~\mathrm{MV}$ Model-Acquisition Comparisons

Clinical Model vs ICP Acquisition

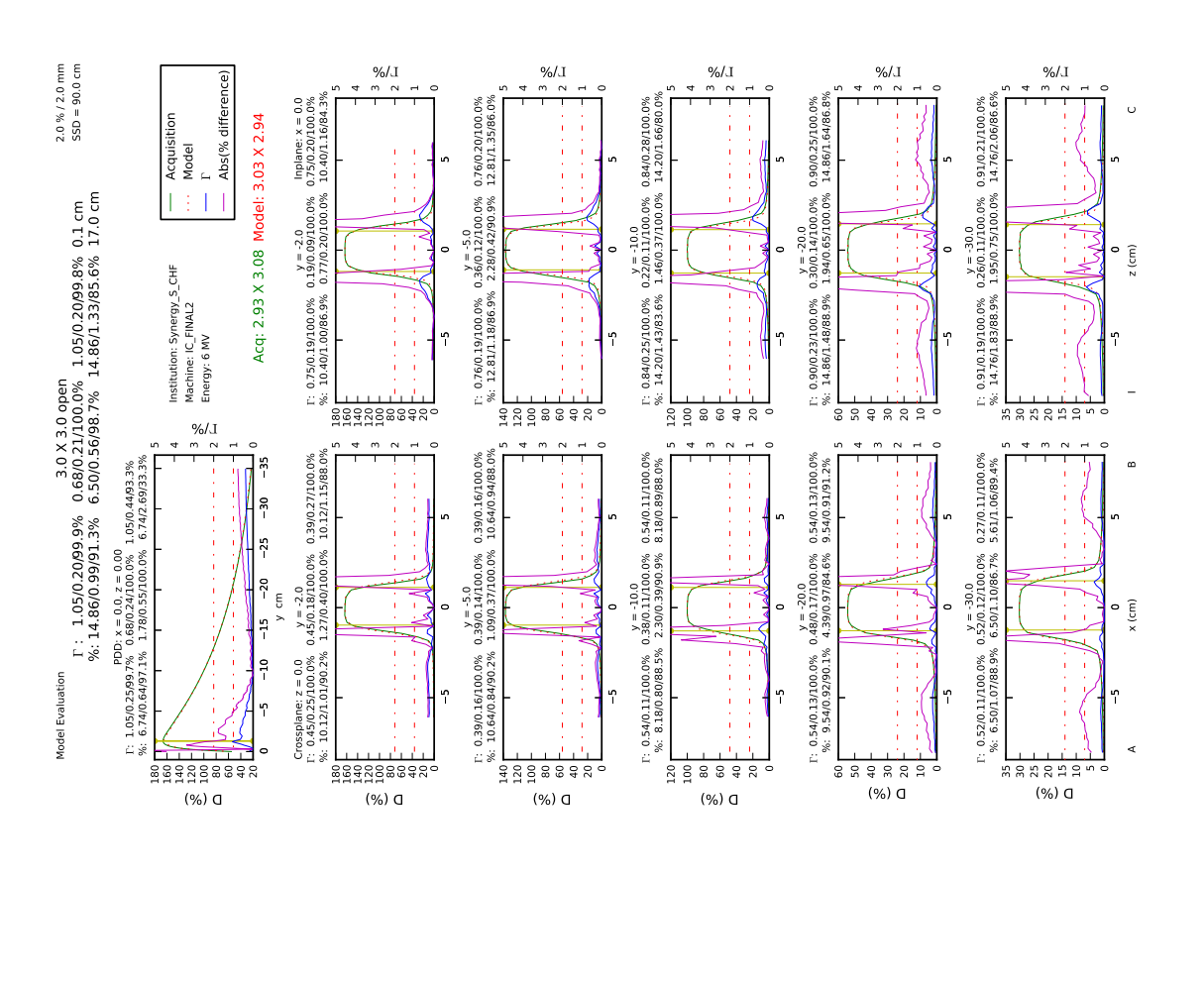


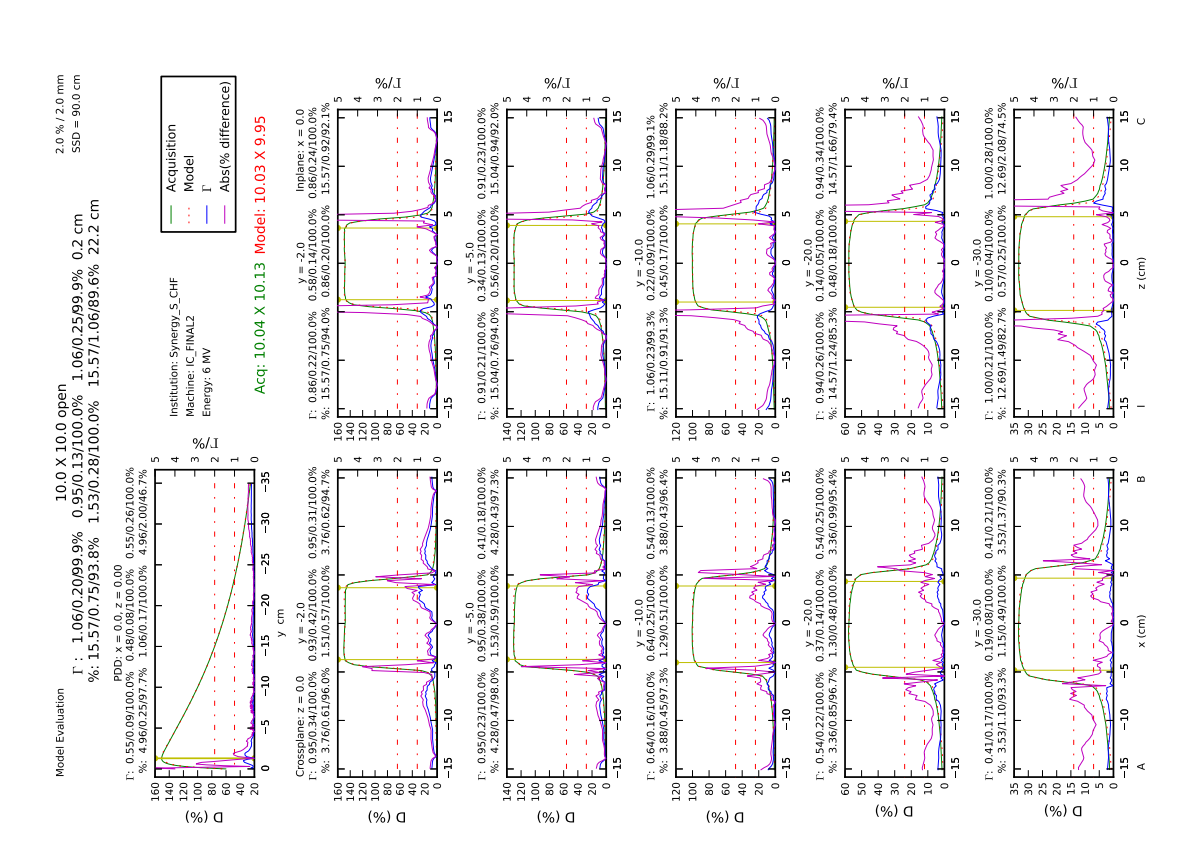


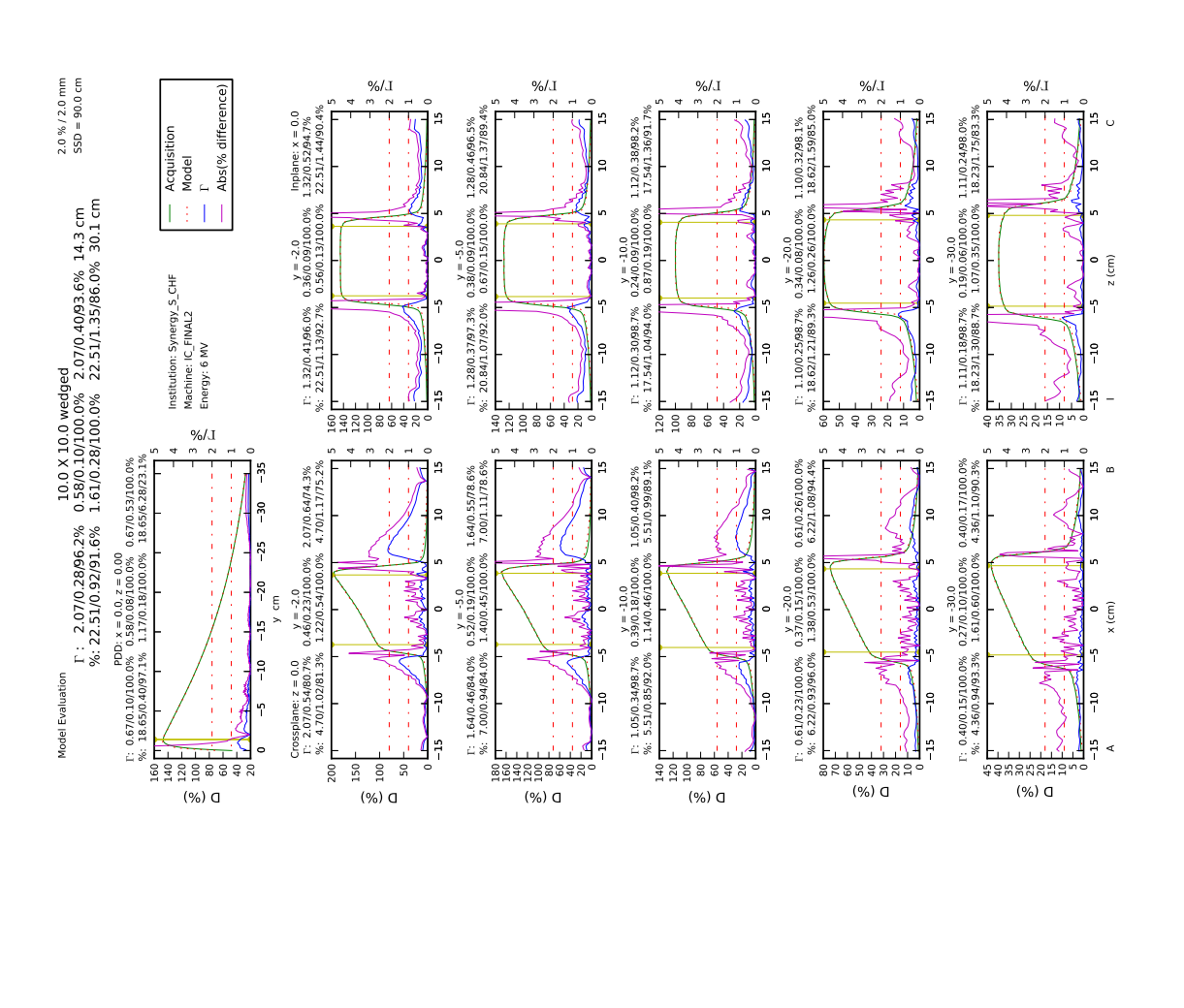


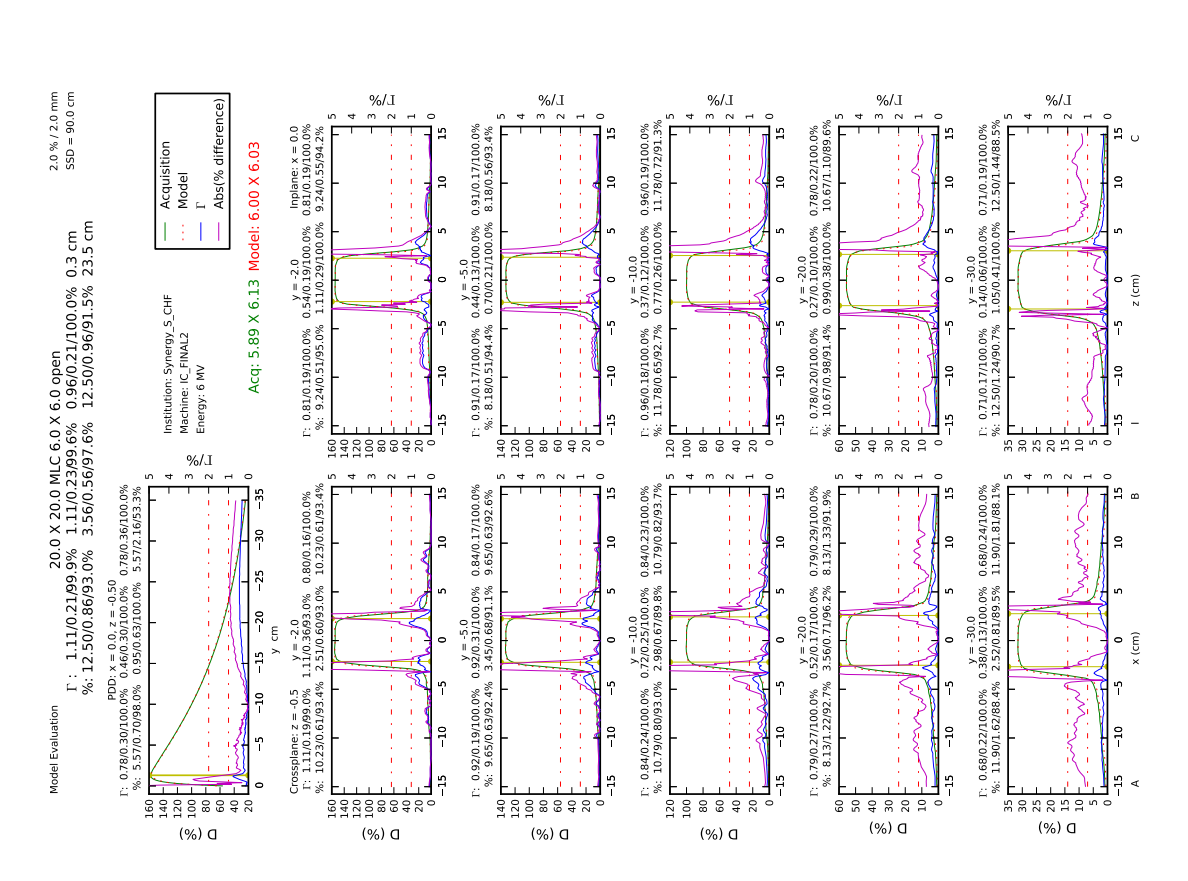


ICP Model vs ICP Acquisition





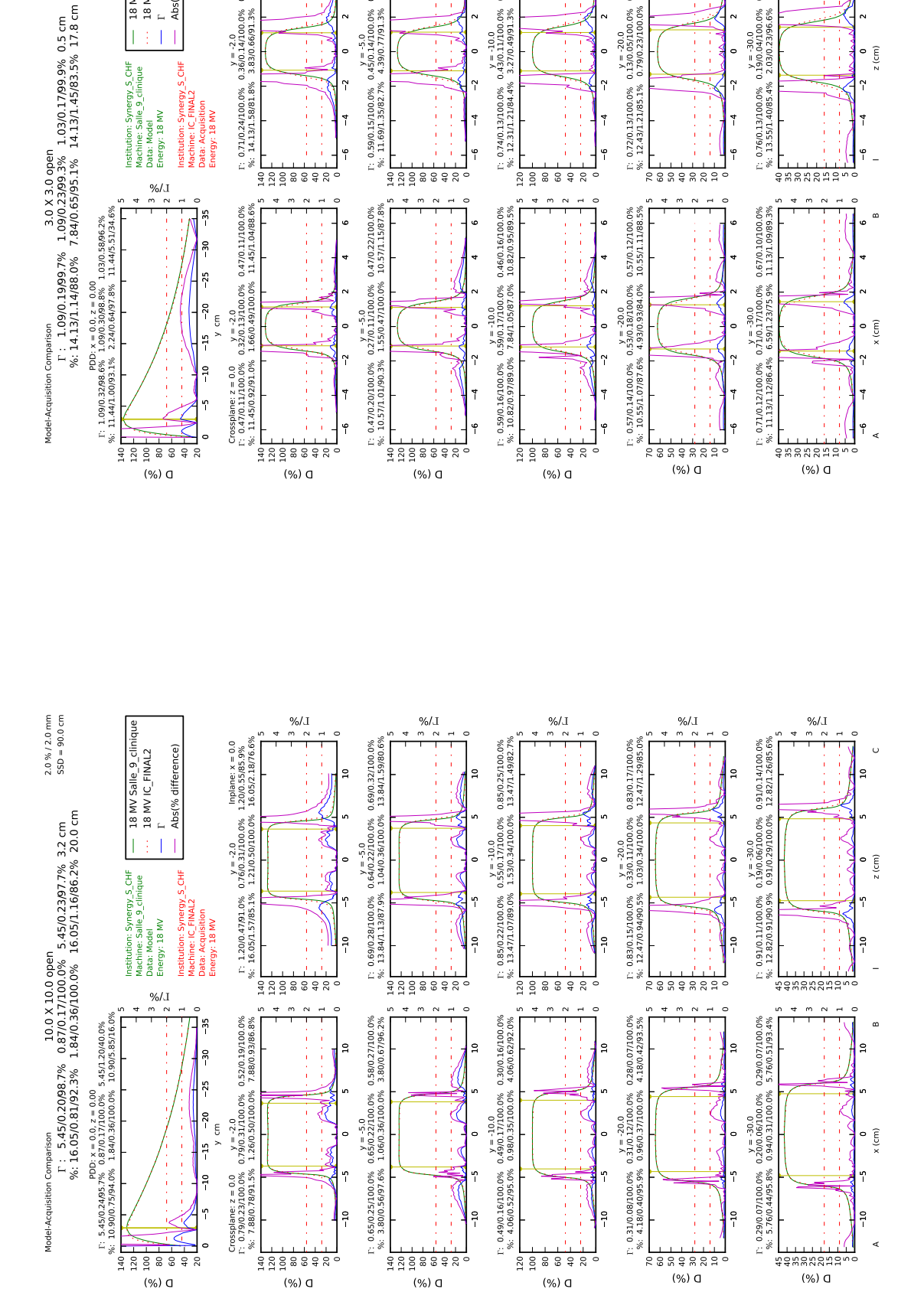




Appendix D

18 MV Model-Acquisition Comparisons

Clinical Model vs ICP Acquisition



2.0 % / 2.0 mm SSD = 90.0 cm

— 18 MV Salle_9_clinique
— 18 MV IC_FINAL2
— I

Institution: Synergy_S_CHF Machine: Salle_9_clinique Data: Model Energy: 18 MV

L\% ~ ~

Abs(% difference)

Institution: Synergy_S_C Machine: IC_FINAL2 Data: Acquisition Energy: 18 MV

-25

L/%

140 100 100 80 60 40 40

Y = -5.0
F: 0.59/0.15/100.0% 0.45/0.14/100.0% 0.59/0.16/100.0%
%: 11.69/1.35/82.7% 4.39/0.77/91.3% 11.69/1.52/80.2%

L/%

120 100 80 80 60 40 20

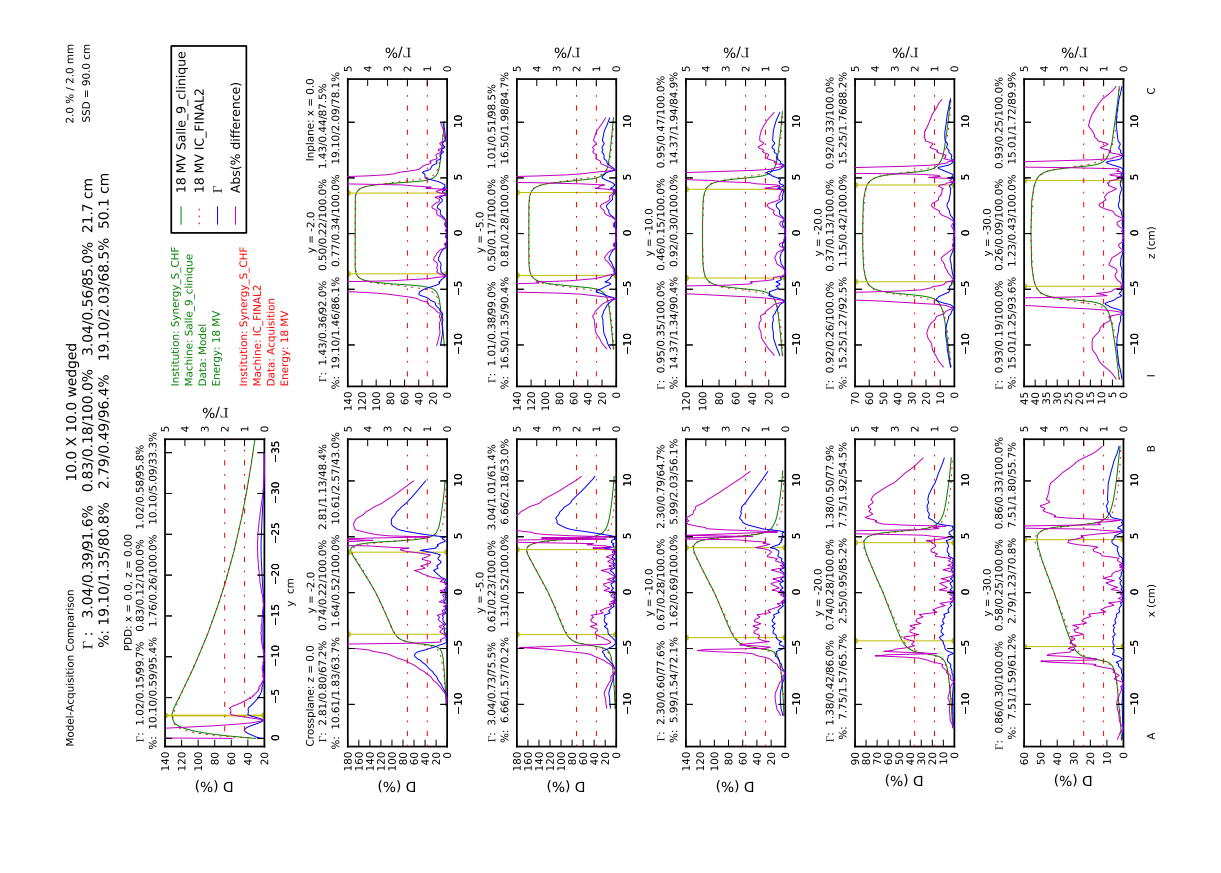
y = -20.0 0.72/0.13/100.0% 0.13/0.05/100.0% 0.72/0.15/100.0% 12.43/1.21/85.1% 0.79/0.23/100.0% 12.43/1.49/80.9%

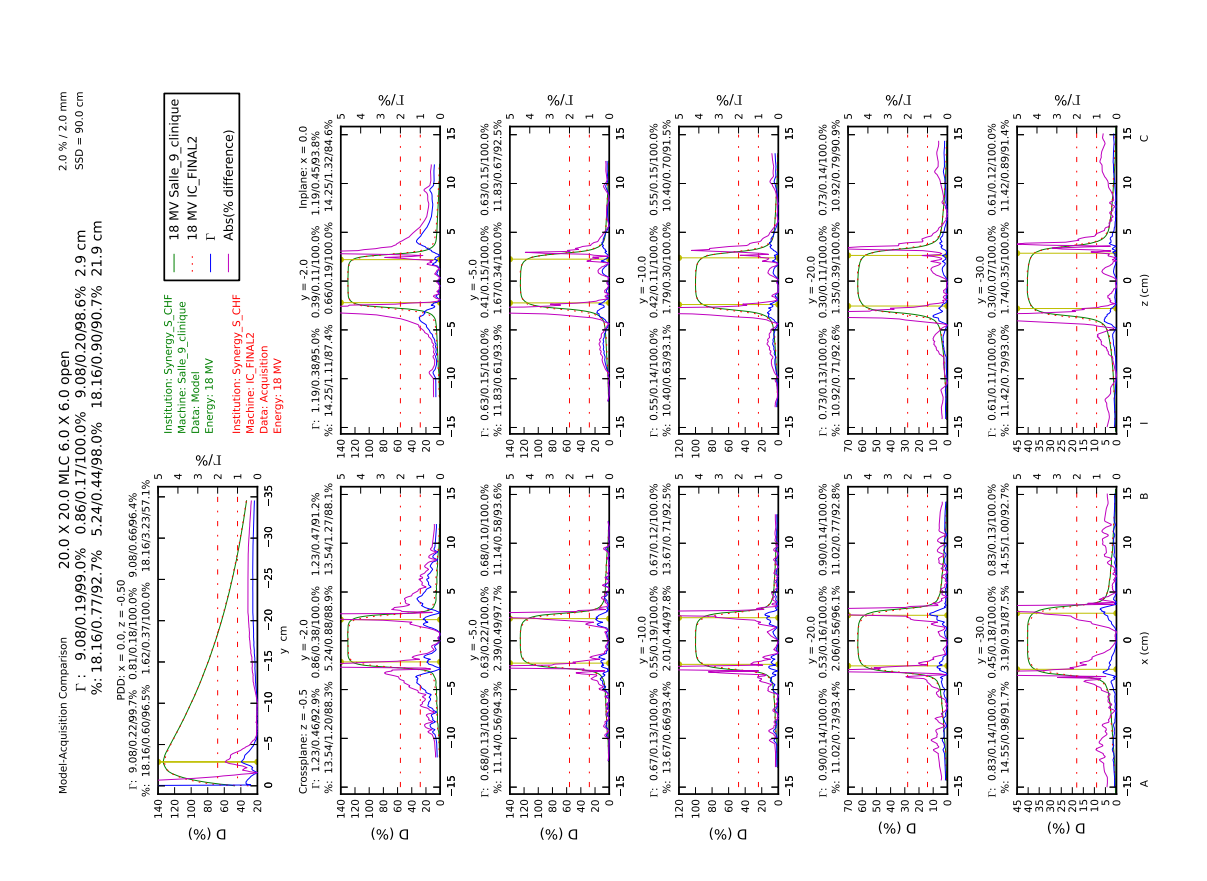
20248220

L/%

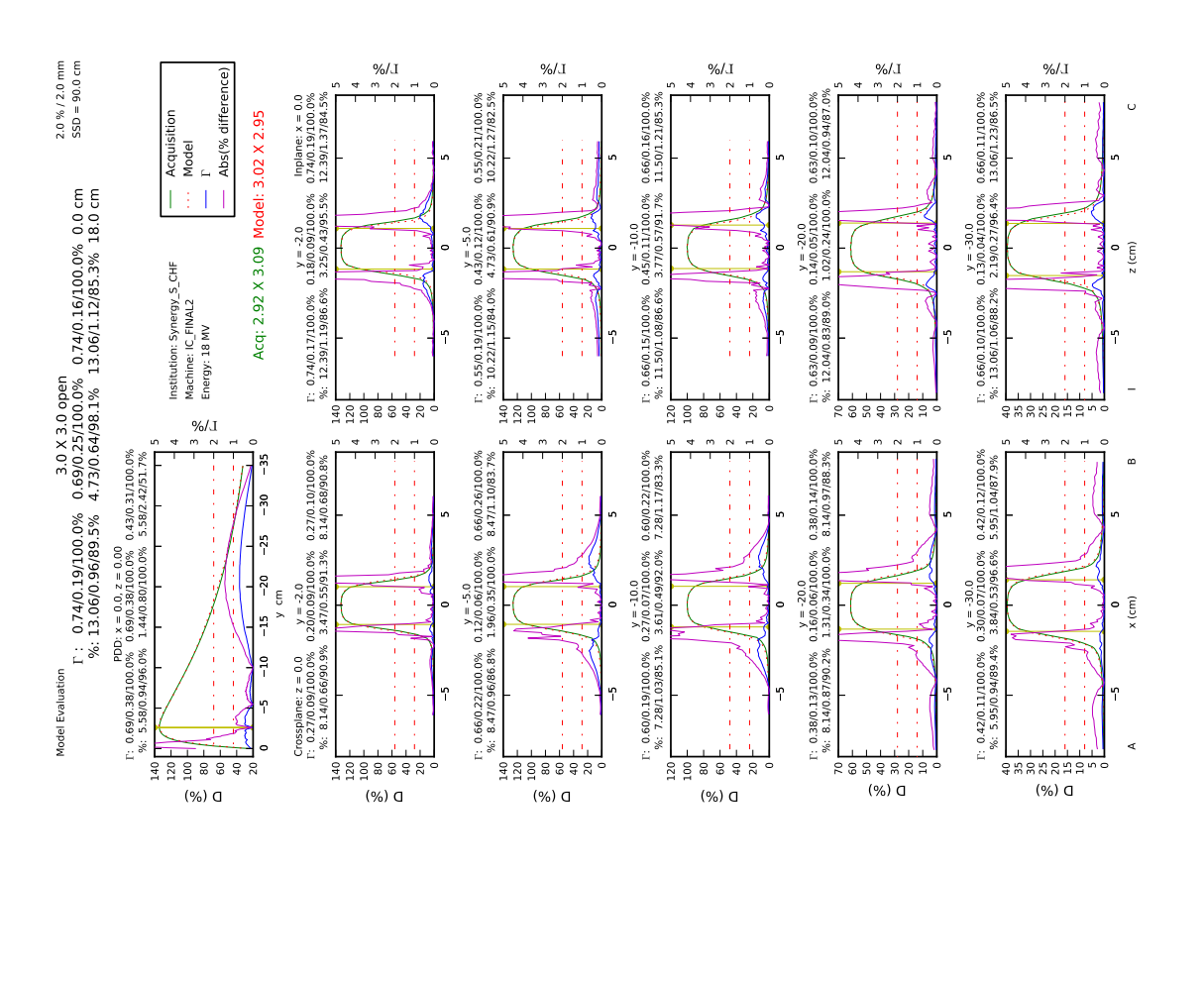
40 33 30 20 20 10 10 5

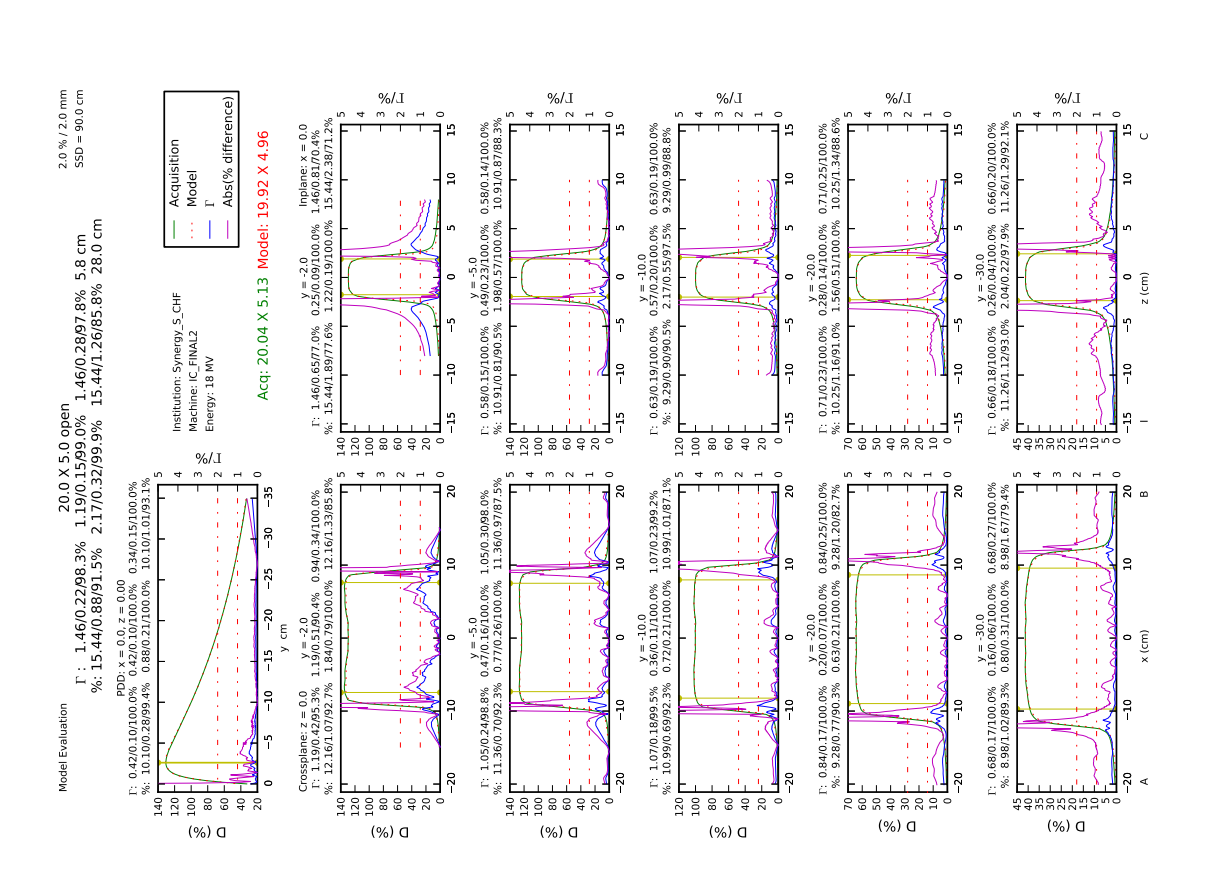
y = -30.0 Γ: 0.76/0.13/100.0% 0.19/0.04/100.0% 0.76/0.16/100.0% %: 13.55/1.40/85.4% 2.03/0.23/96.6% 13.55/1.73/82.2%

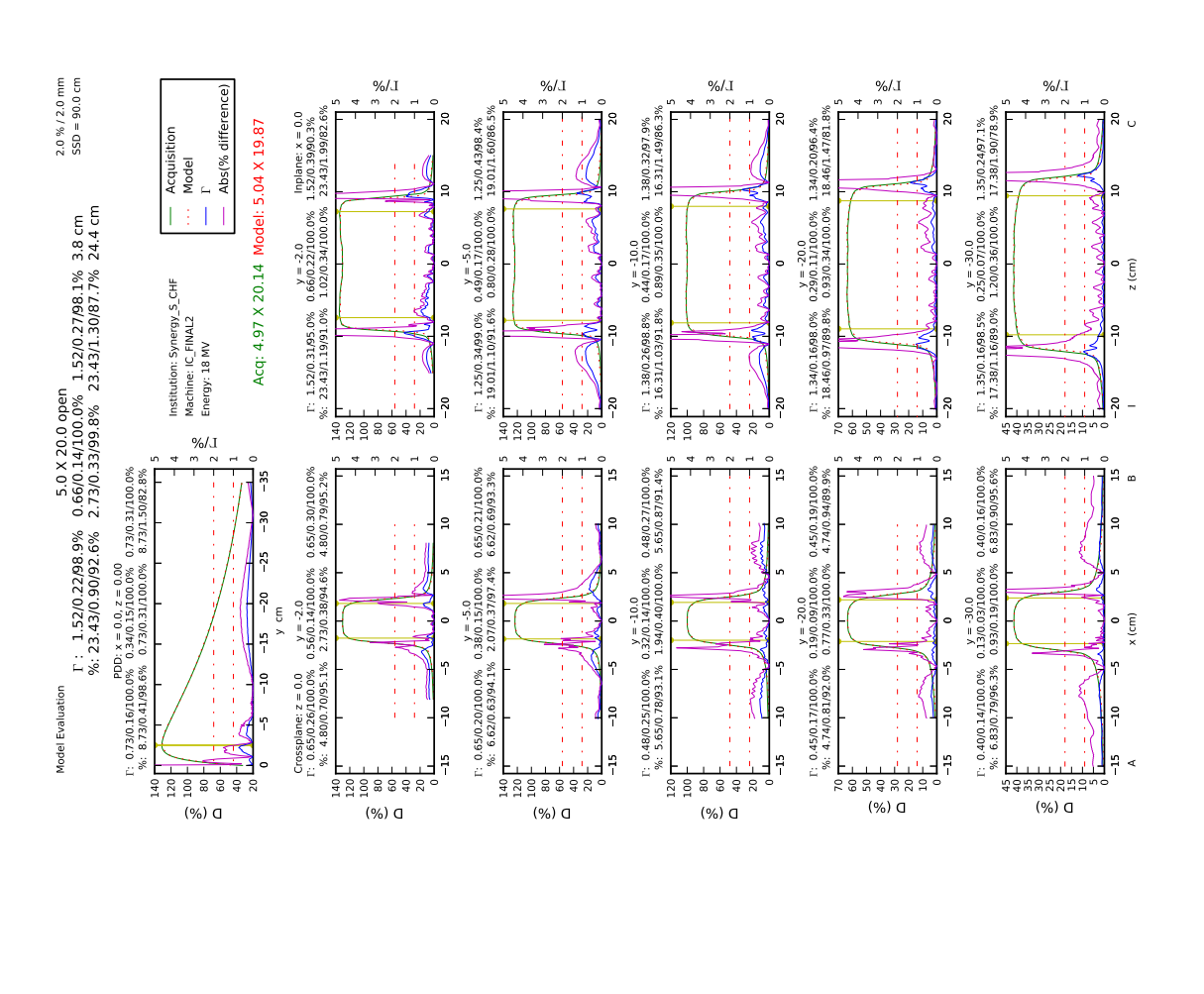


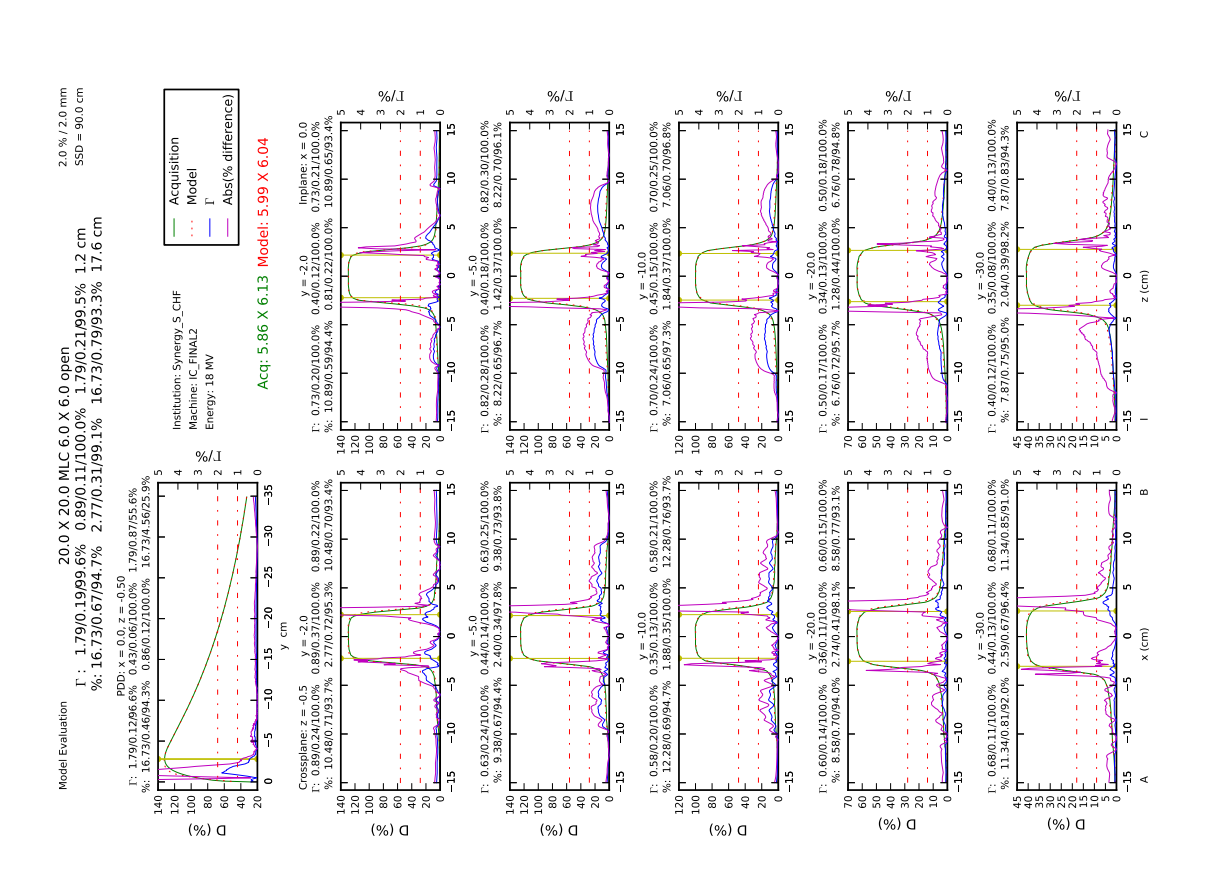


ICP Model vs ICP Acquisition







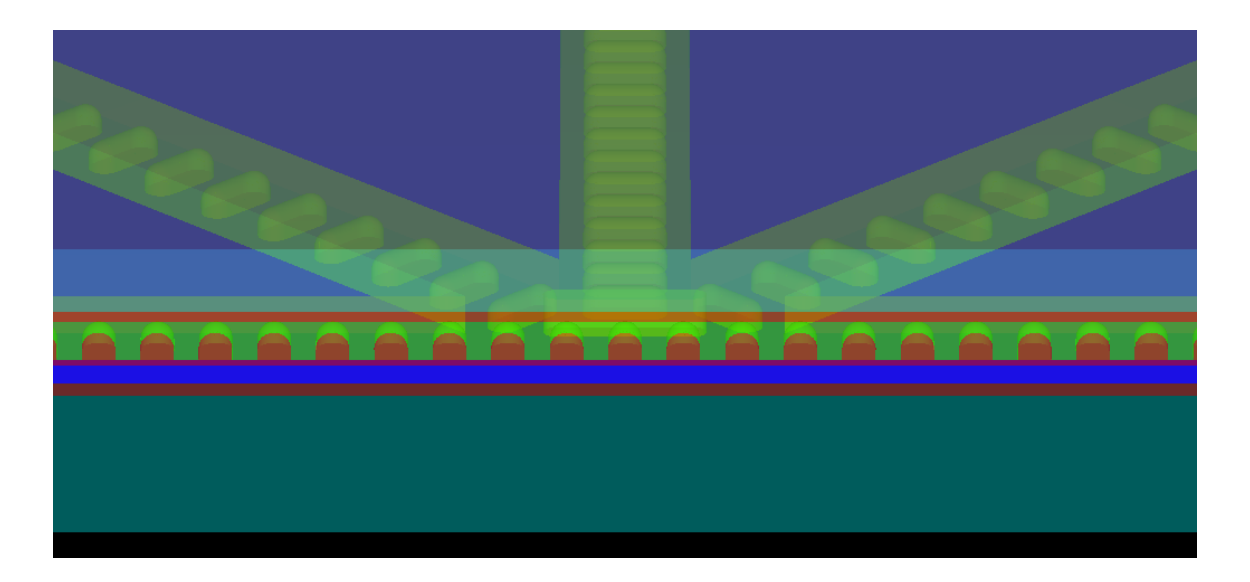


Appendix E

Geometrical model of the IC Profiler for the $\operatorname{egs}++$ Monte Carlo package

A geometrical model of the IC Profiler was made using the egs++ Monte Carlo package. It models the full array without the electronics box. The model was derived from technical schematics obtained from the manufacturer. All four detector axes are included, but the approximation is made that the diagonal axes' chambers are of the same shape as the X and Y axes, whereas in reality the diagonal axes chambers are curve-shaped to follow isodose lines at the corners of square fields.

The model is quite heavy; over 10000 regions are defined. The geometric definition makes much use of egs++'s input loops feature, without which this model would be much harder to create. Six materials are used in the model: air (for some of the internal structure of the array, plus the chamber cavities), aluminum (the material the chambers are constructed with), copper (for the chamber collectors printed on the circuit board), FR4 (the substrate for the printed circuit board), polycarbonate (the inherent buildup and backscatter) and water (to simulate added buildup on top of the array). A computer rendering of the model (cross-sectional view) is shown below, with some materials made transparent to improve visibility of structures.



References

- [1] World Health Organization. Cancer. Fact sheet No297. [Online]. Available: http://www.who.int/mediacentre/factsheets/fs297/en/, February 2011.
- [2] American Cancer Society. Learn About Cancer. Cancer Basics. What is Cancer? [Online]. Available: http://www.cancer.org/Cancer/CancerBasics/what-is-cancer, July 2011.
- [3] World Health Organization. Are the number of cancer cases increasing or decreasing in the world? [Online]. Available: http://www.who.int/features/qa/15/en/index.html, April 2008.
- [4] Canadian Cancer Society. General cancer statistics at a glance. [Online]. Available: http://www.cancer.ca/Canada-wide/About%20cancer/Cancer%20statistics/Stats%20at%20at%20glance/General%20cancer%20stats.aspx?sc_lang=en, October 2011.
- [5] World Health Organization. Global action against cancer now! [Online]. Available: http://www.who.int/entity/cancer/media/GlobalActionCancerEnglfull.pdf, 2005.
- [6] Elekta AB, Stockholm, Sweden. Website. [Online]. Available: http://www.elekta.com/, 2011.
- [7] Ervin B. Podgoršak, editor. Radiation Oncology Physics: A Handbook for Teachers and Students. International Atomic Energy Agency, Sales and Promotion Unit, Publishing Section, Wagramer Strasse 5, P.O. Box 100, A-1400 Vienna, Austria, July 2005.
- [8] R. M. Forbes, A. R. Cooper, and H. H. Mitchell. The composition of the adult human body as determined by chemical analysis. *Journal of Biological Chemistry*, 203, 1953.
- [9] PTW Freiburg GmbH Germany. Website. [Online]. Available: http://www.ptw.de/, 2011.
- [10] Indra J. Das, Chee-Wai Cheng, Ronald J. Watts, Anders Ahnesjö, John Gibbons, X. Allen Li, Jessica Lowenstein, Raj K. Mitra, William E. Simon, and Timothy C. Zhu. Accelerator beam data commissioning equipment and procedures: Report of the TG-106 of the Therapy Physics Committee of the AAPM. *Medical Physics*, 35(9):4186–4215, September 2008.
- [11] Sun Nuclear Corporation, 425A Pineda Court, Melbourne, Florida 32940. IC PROFILERTM User's Guide, Rev. A, September 2008.
- [12] Sun Nuclear Corporation. Personal communication, 2011.
- [13] Thomas A. Simon, William E. Simon, Darren Kahler, Jonathan Li, and Chihray Liu. Wide field array calibration dependence on the stability of measured dose distributions. *Medical Physics*, 37(7):3501–3509, July 2010.

- [14] Sun Nuclear Corporation, 425A Pineda Court, Melbourne, Florida 32940. IC PROFILERTM Software Online Help, Application Version 3.2.0.1, 2010.
- [15] Thomas A. Simon, Jakub Kozelka, William E. Simon, Darren Kahler, Jonathan Li, and Chihray Liu. Characterization of a multi-axis ion chamber array. *Medical Physics*, 37(11):6101–6111, November 2010.
- [16] W. E. Simon, J. Shi, and C. A. Iannello. U.S. Patent No. 6,125,335, 2000.
- [17] A. Alexander, F. DeBlois, G. Stroian, K. Al-Yahya, E. Heath, and J. Seuntjens. MMCTP: a radiotherapy research environment for Monte Carlo and patient-specific treatment planning. *Physics in Medicine and Biology*, 52:N297–N308, 2007.
- [18] F. Hasenbalg, H. Neuenschwander, R. Mini, and E. J. Born. Collapsed cone convolution and analytical anisotropic algorithm dose calculations compared to VMC++ Monte Carlo simulations in clinical cases. *Physics in Medicine and Biology*, 52:3679, 2007.
- [19] Dennis Grofsmid, Maarten Dirkx, Hans Marijnissen, Evert Woudstra, and Ben Heijmen. Dosimetric validation of a commercial Monte Carlo based IMRT planning system. *Medical Physics*, 37(2):540–550, January 2010.
- [20] Tao Han, Mohammad Salehpour, Justin K. Mikell, and Firas Mourtada. Dosimetric comparison of Acuros XB deterministic radiation transport method with Monte Carlo and model-based convolution methods in heterogeneous media. *Medical Physics*, 38(5):2651–2665, May 2011.
- [21] Todd McNutt. Dose Calculations Collapsed Cone Convolution Superposition and Delta Pixel Beam. White paper, Phillips Medical Systems, Global Information Center, I.B.R.S. / C.C.R.I., Numero 11088, 5600 VC Eindhoven, The Netherlands, 2002.
- [22] George Starkschall, Roy E. Steadham, Jr., Richard A. Popple, Salahuddin Ahmad, and Isaac I. Rosen. Beam-commissioning methodology for a three-dimensional convolution/superposition photon dose algorithm. *Journal of Applied Clinical Medical Physics*, 1(1):8, Winter 2000.
- [23] Anthony K. Ho and Bhudatt R. Paliwal. Stopping-power and mass energy-absorption coefficient ratios for Solid Water. *Medical Physics*, 13(3):403–404, May/June 1986.
- [24] V. M. Tello, R. C. Tailor, and W. F. Hanson. How water equivalent are water-equivalent solid materials for output calibration of photon and electron beams? *Medical Physics*, 22(7):1177– 1189, July 1995.
- [25] M. R. McEwen and D. Niven. Characterization of the phantom material Virtual WaterTM in high-energy photon and electron beams. *Medical Physics*, 33(4):876–887, April 2006.
- [26] Jan Seuntjens, Marina Olivares, Michael Evans, and Ervin Podgoršak. Absorbed dose to water reference dosimetry using solid phantoms in the context of absorbed-dose protocols. *Medical Physics*, 32(9):2945, September 2005.
- [27] Ramani Ramaseshan, Kirpal Kohli, Fred Cao, and Robert Heaton. Dosimetric evaluation of Plastic Water Diagnostic Therapy. *Journal of Applied Clinical Medical Physics*, 9(3):98–111, Spring 2008.

- [28] Faiz M. Khan. *The Physics of Radiation Therapy*. Lippincott Williams & Wilkins, 530 Walnut Street, Philadelphia, PA 19106 USA, third edition, 2003.
- [29] Karin Eklund and Anders Ahnesjö. Spectral perturbations from silicon diode detector encapsulation and shielding in photon fields. *Medical Physics*, 37(11):6055–6060, November 2010.
- [30] Davide Fontanarosa, Lucia Clara Orlandini, Italo Andriani, and Luca Bernadi. Commissioning Varian enhanced dynamic wedge in the PINNACLE treatment planning system using GafchromicTM EBT film. *Medical Physics*, 36(10):4504, October 2009.
- [31] Bruce J. Gerbi. A mathematical expression for %DD accurate from Co-60 to 24 MV. *Medical Physics*, 18(4):724–726, July/August 1991.
- [32] Wieslaw Wierzbicki, Katharina E. Sixel, and Ervin B. Podgoršak. An analytical representation of radiosurgical depth-dose data. *Physics in Medicine and Biology*, 38:1351–1358, 1993.
- [33] D. L. Fehl. A simple one-dimensional model for understanding planar dose-versus-depth profiles in mixed photon/electron fields. *Medical Physics*, 20(5):1361–1370, September/October 1993.
- [34] Bengt E. Bjärngard and Paul Vadash. Analysis of central-axis doses for high-energy x rays. Medical Physics, 22(7):1191–1195, July 1995.
- [35] Ken Kang-Hsin Wang and Timothy C. Zhu. Modeling scatter-to-primary dose ratio for mega-voltage photon beams. *Medical Physics*, 37(10):5270–5278, October 2010.
- [36] Daniel A. Low and James F. Depmsey. Evaluation of the gamma dose distribution comparison method. *Medical Physics*, 30(9):2455–2464, September 2003.
- [37] Tao Ju, Tim Simpson, Joseph O. Deasy, and Daniel A. Low. Geometric interpretation of the γ dose distribution technique: Interpolation-free calculation. *Medical Physics*, 35(3):879–887, March 2008.
- [38] Jiankui Yuan and Weimin Chen. A γ dose distribution evaluation technique using the k-d tree for nearest neighbor searching. *Medical Physics*, 37(9):4868–4873, September 2010.
- [39] Heng Li, Lei Dong, Lifei Zhang, James N. Yang, Michael T. Gillin, and X. Ronald Zhu. Toward a better understanding of the gamma index: Investigation of parameters with a surface-based distance method. *Medical Physics*, 38(12):6730–6741, December 2011.
- [40] Guido van Rossum et al. Python Programming Language. [Online]. Available: http://www.python.org/, 1990-.
- [41] Philips Medical Systems. *Pinnacle 3 Physics Reference Guide*. Philips Medical Systems Inc., 5520 Nobel Drive Suite 125, Fitchburg WI 53711, 2009.
- [42] Ervin B. Podgoršak. *Radiation Physics for Medical Physicists*. Springer-Verlag, Berlin Heidelberg, second, enlarged edition, 2010.
- [43] Eric Jones, Travis Oliphant, Pearu Peterson, et al. SciPy: Open source scientific tools for Python. [Online]. Available: http://www.scipy.org/, 2001-.

- [44] P. Andreo, D. T. Burns, K. Hohlfeld, M. S. Huq, T. Kanai, F. Laitano, V. Smyth, and S. Vynckier. IAEA TRS-398 Absorbed Dose Determination in External Beam Radiotherapy: An International Code of Practice for Dosimetry based on Standards of Absorbed Dose to Water. Technical Report V.10A, International Atomic Energy Agency, Dosimetry and Medical Radiation Physics Section, International Atomic Energy Agency, Wagramer Strasse 5, P.O. Box 100, A-1400, Vienna, Austria, May 2001.
- [45] Ben Nelms. DVH β TEAMHEADQUARTERS. [Online]. Available: http://www.canislupusllc.com/3DVH/3DVHBETA_index.htm, 2011.
- [46] Sun Nuclear Corporation. 3DVH. [Online]. Available: http://www.sunnuclear.com/medphys/patientqa/3dvh/3dvh.asp, 2011.
- [47] Philips Medical Systems. *Pinnacle 3 Release Notes Release 9.2.* Philips Medical Systems Inc., 5520 Nobel Drive Suite 125, Fitchburg WI 53711, 2011.
- [48] I. Kawrakow, E. Mainegra-Hing, F. Tesssier, and B. R. B. Walters. The EGSnrc C++ class library. Technical report, NRC Report PIRS-898 (rev A), Ottawa, Canada, 2009.